Politecnico di Torino

ScuDo
Scuola di Dottorato ~ Doctoral School
WHAT YOU ARE, TAKES YOU FAR

Doctoral Dissertation
Doctoral Program in Energy Engineering (35^{th}cycle)

Optimization of Launch Power in Optical Line Systems and Design of Optical Networks for Multi-band Transmission

By

Bruno Correia

******

Supervisor(s):
Professor Vittorio Curri, Supervisor
Dr. Nelson Costa, Industrial Mentor
Dr. Antonio Napoli, Industrial Mentor
Dr. João Pedro, Industrial Mentor

Doctoral Examination Committee:
Prof. Andrea Sgambelluri , Referee, Scuola Superiore Sant'Anna
Prof. Krzysztof Walkowiak, Referee, Wroclaw University of Science and Technology

Politecnico di Torino
2023

Declaration

I hereby declare that, the contents and organization of this dissertation constitute my own original work and does not compromise in any way the rights of third parties, including those relating to the security of personal data.

Bruno Correia
2023

* This dissertation is presented in partial fulfillment of the requirements for **Ph.D. degree** in the Graduate School of Politecnico di Torino (ScuDo).

I would like to dedicate this thesis to my loving family

Acknowledgements

First of all, I would like to thank my supervisor Prof. Vittorio Curri for the opportunity to perform this Ph.D. The combination of patience, attention and technical knowledge provided by him was crucial for the development of this work, and also personal. I am so grateful to the WON project, also for the Ph.D. opportunity, specially to my industrial advisor Antonio Napoli, which was always solicitous to give me advices when needed and being a example of hardworking and good humor. I would like to thanks for the technical support provided by the Infinera team, precisely by João Pedro and Nelson Costa. Their perspective shown during the numerous meeting that we had during this Ph.D. was crucial to expand my view and knowledge of the field, and sometimes also being able to speak my mother language. I want also to thank professor Nicola Sambo, from the Scuola Superiore Sant'Ana, for his guidance and contribution during our jointly work, as he was always very solicitous to solve my questions and doubts about the work. Finally I would like to thanks the help provided by the WON project manager Tatiana Kilina and by the WON project representative at Polito Maria Elisabetta Racca, which were always very kind to me.

Now, my gratitude goes to all my colleagues for their friendship and companionship during this Ph.D, for which I will always remember them. Starting by the PLANET team, the experience shared with Rasoul Sadeghi, Elliot London, Andrea D'Amico, Giacomo Borraccini, Emanuele Virgillito, Ihtesham Khan, Muhammad Umar Masood, Fehmida Usmani, Rocco D'Ingillo, Renato Ambrosone, Vittorio Gatto, and Alessio Ferrari will be forever remembered with kindness. I also would like to thanks to all WON students, specially the ones which I have the pleasure to work more closely, like Andre Souza, Matheus Senna, Thyago Monteiro, Rafael Kraemer, Caio Santos, Pratim Hazarika and Aleksandr Donodin.

Finally, I am so grateful for the constant support of my brother and my parents, that even physically distant from me during this time, were always present to encourage me during the difficult times.

Abstract

This thesis explores the topic of optical transmission and networks, addressing the challenges and trends in future optical communication systems. The development of solutions that can support the continuous growth demanded from optical networks are an extremely important issue, due to the increasing of digital services and applications, 5G deployment and many other factors, which are contributing to stress the actual infrastructure to its limit. The first chapter provides an overview of the advancements in optical transmission technology during the past 50 years, from the first systems providing capacity of dozens of Mbps to the most recent ones, with provide transmission capacity of several signals of hundreds Gbps each. Moreover, we identify the key challenges faced by optical networks and discusses the emerging trends that shape the future of optical transmission.

The second chapter focuses on the modeling of the physical layer in optical line systems (OLSs), which compose the optical networks. This chapter delves into the detailed information about the components that constitute the OLS, e.g. fibers, transceivers, and amplifiers. The optical network architecture is also explored, encompassing topics such as geographic optical network structure, software-defined networking (SDN), disaggregated networks, and finally the optical network transport model. This chapter also discusses the concept of multi-band transmission (MBT) systems, technology which focus on increase the fiber spectral bandwidth used for transmission, elucidating their benefits and challenges.

In the third chapter, we investigate the launch power in MBT systems topic. Firstly, we analyze the impact of launch power on the quality of transmission (QoT) for this scenario. Then, we explore the strategy of tilt/offset with a brute-force approach to optimize the launch power. Additionally, we propose the application of a genetic algorithm (GA) to refine this strategy, aiming to reduce the computational effort while improving the performance of the system. We shown that, besides the

fact that increasing the fiber spectral usage for increase the number of transmitted channels, the launch power optimization can mitigate the impairments raised by this scenario.

Moving forward, the fourth chapter focuses on the upgrade and design of multi-band optical networks. We start by evaluating the impact of incorporating different spectral bands, considering their effects on existent systems performance, as well as the capacity increasing provided by this upgrade. Furthermore, we propose a network design specifically for the C+L+S band system, with the objective of achieving comparable performance to the C-band system while minimizing the incremental costs.

Finally, in the fifth chapter, we present the conclusions drawn from our research. We summarize the findings from each chapter, highlighting the advancements made in MBT systems and their implications for future network design and optimization. We think that this thesis provides valuable insights into the evolution of optical transmission, modeling techniques, and optimization strategies, offering guidance for the development of efficient and cost-effective multi-band optical communication networks in the future.

Contents

List of Figures

List of Tables

List of Abbreviations

ADC analog-to-digital converter

AS amplification site

ASE amplified spontaneous emission

BDFA bismuth doped fiber amplifier

BDM band-division multiplexing

BF brute force

BP blocking-probability

BPD balanced photodetector

CAPEX capital expenditure

CD chromatic dispersion

CUT channel under test

DCF dispersion-compensating fiber

DEMUX demultiplexer

DFA doped fiber amplifier

DP dual-polarization

DP-16QAM dual polarization 16 quadrature amplitude modulation

DP-QPSK dual polarization quadrature phase shift keying

DSP digital signal processor

DWDM dense wavelength-division multiplexing

EDFA erbium doped fiber amplifier

FEC forward error correction

FF first-fit

FWM four-wave mixing

GA genetic algorithm

GB guard-band

GFF gain flattening filter

GGN generalized Gaussian-noise

GN Gaussian noise

GNPy Gaussian noise simulation in Python

GSNR signal-to-noise ratio

GVD group-velocity dispersion

ILA inline amplifier

IoT Internet of Things

JPDF joint probability density function

LOGO local-optimization global-optimization

LP lightpath

MBT multi-band transmission

MCVD modified chemical vapor deposition

MUX multiplexer

MZM Mach-Zehnder modulator

NDFA neodymium doped fiber amplifier

NE network element

NF noise-figure

NLI nonlinear interference

NLSE nonlinear Schrödinger equation

O-E-O optical-electrical-optical

OA optical amplifier

OLO optical local oscillator

OLS optical line system

OPEX operational expenditure

OSNR optical signal-to-noise ratio

PBS polarization beam splitter

PCU power control unit

PDL polarization dependent loss

PMD polarization-mode dispersion

PON passive optical network

PS probabilistic shaping

QAM quadrature amplitude modulation

QoT quality of transmission

QoT-E QoT estimator

RGSNR required GSNR

ROADM reconfigurable optical add-drop multiplexer

RS route space

RWA routing and wavelength assignment

SA spectrum allocation

SDM spatial-division multiplexing

SDN software-defined networking

SNAP statistical network assessment process

SNR signal-to-noise ratio

SNR_{NL} nonlinear signal-to-noise ratio

SOA semiconductor optical amplifier

SPM self-phase modulation

SRS stimulatted Raman scattering

SSME spectrally separated Manakov equation

SSMF standard single-mode fiber

TDFA thulium doped fiber amplifier

TFF-WDM thin-film-filter wavelength-division multiplexer

TIP Telecom Infra Project

UWB ultra-wide band

WA wavelength assignment

WDM wavelength-division multiplexing

WSS wavelength-selective switch

XPM cross-phase modulation

List of Scientific Contributions

A list of the scientific contributions carried out during the PhD are described here.

Peer Reviewed International Journals

1. Bruno Correia, Rasoul Sadeghi, Emanuele Virgillito, Antonio Napoli, Nelson Costa, João Pedro, and Vittorio Curri. Power control strategies and network performance assessment for C+L+S multiband optical transport. *Journal of Optical Communications and Networking*, 13(7):147, jul 2021

2. Nicola Sambo, Bruno Correia, Antonio Napoli, João Pedro, Leily Kiani, Piero Castoldi, and Vittorio Curri. Network upgrade exploiting multi band: S- or E-band? *Journal of Optical Communications and Networking*, 14(9):749, sep 2022

3. Andrea D'Amico, Bruno Correia, Elliot London, Emanuele Virgillito, Giacomo Borraccini, Antonio Napoli, and Vittorio Curri. Scalable and Disaggregated GGN Approximation Applied to a C+L+S Optical Network. *Journal of Lightwave Technology*, 40(11):3499–3511, jun 2022

4. Rasoul Sadeghi, Bruno Correia, Andre Souza, Nelson Costa, Joao Pedro, Antonio Napoli, and Vittorio Curri. Transparent vs Translucent Multi-Band Optical Networking: Capacity and Energy Analyses. *Journal of Lightwave Technology*, 40(11):3486–3498, 2022

5. Matheus Sena, Pratim Hazarika, Caio Santos, Bruno Correia, Robert Emmerich, Behnam Shariati, Antonio Napoli, Vittorio Curri, Wladek Forysiak, Colja Schubert, Johannes K. Fischer, and Ronald Freund. Advanced DSP-Based Monitoring for Spatially Resolved and Wavelength-Dependent Amplifier Gain Estimation and Fault Location in C+L-Band Systems. *Journal of Lightwave Technology*, 41(3):989–998, feb 2023

Contributions to International Conferences

1. Emanuele Virgillito, Rasoul Sadeghi, Alessio Ferrari, Antonio Napoli, Bruno Correia, and Vittorio Curri. Network Performance Assessment with Uniform and Non-Uniform Nodes Distribution in C+L Upgrades vs. Fiber Doubling SDM Solutions. In *2020 International Conference on Optical Network Design and Modeling (ONDM)*, pages 1–6. IEEE, may 2020

2. Bruno Correia, Rasoul Sadeghi, Emanuele Virgillito, Antonio Napoli, Nelson Costa, Joao Pedro, and Vittorio Curri. Networking Performance of Power Optimized C+L+S Multiband Transmission. In *GLOBECOM 2020 - 2020 IEEE Global Communications Conference*, pages 1–6. IEEE, dec 2020

3. Rasoul Sadeghi, Bruno Correia, Emanuele Virgillito, Nelson Costa, Joao Pedro, Antonio Napoli, and Vittorio Curri. Multi Bands Network Performance Assessment for Different System Upgrades. In *2020 IEEE Photonics Conference (IPC)*, pages 1–2. IEEE, sep 2020

4. Bruno Correia, Rasoul Sadeghi, Emanuele Virgillito, Antonio Napoli, and Vittorio Curri. Optical Power Control Strategies for Optimized C + L + S-bands Network Performance. In *Optical Fiber Communication Conference (OFC) 2021*, page W1F.8, 2021

5. Rasoul Sadeghi, Bruno Correia, Emanuele Virgillito, Antonio Napoli, João Pedro, and Vittorio Curri. Performance Comparison of Translucent C-band and Transparent C + L-band Network. In *Optical Fiber Communication Conference (OFC) 2021*, volume 1, page M3E.4, 2021

6. Emanuele Virgillito, Elliot London, Andrea D Amico, Bruno Correia, Antonio Napoli, and Vittorio Curri. Single- vs . Multi-Band Optimized Power Control in C + L WDM 400G Line Systems. In *Optical Fiber Communication Conference (OFC) 2021*, page Th4C.3. OSA, 2021

7. Rasoul Sadeghi, Bruno Correia, Emanuele Virgillito, Antonio Napoli, Nelson Costa, Joao Pedro, and Vittorio Curri. Comparison of Transceiver and C+L Band Upgrades: Network Traffic and Energy Assessment. In *2021 International Conference on Electrical, Communication, and Computer Engineering (ICECCE)*, pages 1–6. IEEE, jun 2021

8. Rasoul Sadeghi, Bruno Correia, Emanuele Virgillito, Antonio Napoli, Nelson Costa, Joao Pedro, and Vittorio Curri. Network Comparison of C+L-band Transparent versus C-band Translucent Upgrade. In *2021 International Conference on Optical Network Design and Modeling (ONDM)*, pages 1–6. IEEE, jun 2021

9. Bruno Correia, Rasoul Sadeghi, Emanuele Virgillito, Antonio Napoli, Nelson Costa, Joao Pedro, and Vittorio Curri. Multiband Power Control Impact on the Transmission Capacity of Optical Line Systems. In *2021 IEEE Photonics Society Summer Topicals Meeting Series (SUM)*, pages 1–2. IEEE, jul 2021

10. Rasoul Sadeghi, Bruno Correia, Emanuele Virgillito, Antonio Napoli, Nelson Costa, Joao Pedro, and Vittorio Curri. C+L-band Network Upgrade: Capacity and Energy Analyses with Different Transceivers. In *2021 IEEE Photonics Society Summer Topicals Meeting Series (SUM)*, pages 1–2. IEEE, jul 2021

11. Rasoul Sadeghi, Bruno Correia, Emanuele Virgilito, Elliot London, Nelson Costa, Joao Pedro, Antonio Napoli, and Vittorio Curri. Optimized Translucent S-band Transmission in Multi-Band Optical Networks. In *2021 European Conference on Optical Communication (ECOC)*, pages 1–4. IEEE, sep 2021

12. Rasoul Sadeghi, Bruno Correia, Emanuele Virgillito, Antonio Napoli, Nelson Costa, Joao Pedro, and Vittorio Curri. Cost-Effective Capacity Increase of Deployed Optical Networks to Support the Future Internet: the Multi-Band Approach. In *2021 12th International Conference on Network of the Future (NoF)*, pages 1–7. IEEE, oct 2021

13. Rasoul Sadeghi, Bruno Correia, Emanuele Virgillito, Antonio Napoli, Nelson Costa, Joao Pedro, and Vittorio Curri. Network Capacity and Energy Consumption: Transparent C + L -band vs Translucent C-band. In *2021 IEEE Photonics Conference (IPC)*, pages 1–2. IEEE, oct 2021

14. B. Correia, A. Donodin, R. Sadeghi, V. Dvoyrin, V. Dvoyrin, A. Napoli, J. Pedro, J. Pedro, N. Costa, W. Forysiak, S. K. Turitsyn, S. K. Turitsyn, and V. Curri. QoT Evaluation of Optical Line System Transmission with Bismuth-Doped Fiber Amplifiers in the E-Band. In *Asia Communications and Photonics Conference 2021 (2021)*, page M4I.5. Optica Publishing Group, oct 2021

15. Andre Souza, Bruno Correia, Nelson Costa, Joao Pedro, and Joao Pires. Accurate and Scalable Quality of Transmission Estimation for Wideband Optical Systems. In *2021 IEEE 26th International Workshop on Computer Aided Modeling and Design of Communication Links and Networks (CAMAD)*, volume 2021-Octob, pages 1–6. IEEE, oct 2021

16. Rasoul Sadeghi, Bruno Correia, Emanuele Virgillito, Antonio Napoli, Nelson Costa, João Pedro, and Vittorio Curri. Optimal Spectral Usage and Energy Efficient S-to-U Multiband Optical Networking. In *Optical Fiber Communication Conference (OFC) 2022*, page W3F.7, Washington, D.C., mar 2022. Optica Publishing Group

17. Nicola Sambo, Bruno Correia, Antonio Napoli, João Pedro, Piero Castoldi, and Vittorio Curri. Transport Network Upgrade exploiting Multi-Band Systems: S- versus E-band. In *Optical Fiber Communication Conference (OFC)*, page W3F.8. Optica Publishing Group, mar 2022

18. André Souza, Rasoul Sadeghi, Bruno Correia, Nelson Costa, Antonio Napoli, Vittorio Curri, João Pedro, and João Pires. Optimal Pay-As-You-Grow Deployment on S+C+L Multi-band Systems. In *Optical Fiber Communication Conference (OFC) 2022*, page W3F.4, Washington, D.C., mar 2022. Optica Publishing Group

19. Rasoul Sadeghi, Bruno Correia, Andre Souza, Antonio Napoli, Nelson Costa, Joao Pedro, and Vittorio Curri. Capacity and Energy Consumption Comparison in Translucent versus Transparent Multi-band Designs. In *2022 International Conference on Optical Network Design and Modeling, ONDM 2022*, pages 1–3. IEEE, may 2022

20. Rasoul Sadeghi, Bruno Correia, Antonio Napoli, Nelson Costa, João Pedro, and Vittorio Curri. Capacity and Energy Usage of Translucent and Multi-Band Transparent Optical Networks. In *Optica Advanced Photonics Congress 2022*, page NeTu3D.2, Washington, D.C., jul 2022. Optica Publishing Group

21. Rasoul Sadeghi, Bruno Correia, Nelson Costa, João Pedro, João Pedro, Antonio Napoli, and Vittorio Curri. Extending the C+L System Bandwidth versus Exploiting Part of the S-band: Network Capacity and Interface Count Comparison. In *European Conference on Optical Communication (ECOC) 2022*, page We1B.2. Optica Publishing Group, sep 2022

22. Muhammad Umar Masood, Ihtesham Khan, Lorenzo Tunesi, Bruno Correia, Rasoul Sadeghi, Enrico Ghillino, Paolo Bardella, Andrea Carena, and Vittorio Curri. Networking Analysis of Photonics Integrated Multiband WSS Based ROADM Architecture. In *2022 International Conference on Software, Telecommunications and Computer Networks (SoftCOM)*, pages 1–6. IEEE, sep 2022

23. Muhammad Umar Masood, Lorenzo Tunesi, Bruno Correia, Ihtesham Khan, Enrico Ghillino, Paolo Bardella, Andrea Carena, and Vittorio Curri. Photonics Integrated Multiband WSS Based ROADM Architecture: A Networking Analysis. In *2022 Asia Communications and Photonics Conference (ACP)*, pages 1243–1247. IEEE, nov 2022

24. Muhammad Umar Masood, Ihtesham Khan, Lorenzo Tunesi, Bruno Correia, Enrico Ghillino, Paolo Bardella, Andrea Carena, and Vittorio Curri. Network Traffic Analysis of Modular Multiband Integrated WSS based ROADMs. In *IEEE Photonics Conference, IPC 2022*. Institute of Electrical and Electronics Engineers Inc., 2022

25. Muhammad Umar Masood, Ihtesham Khan, Lorenzo Tunesi, Bruno Correia, Enrico Ghillino, Paolo Bardella, Andrea Carena, and Vittorio Curri. Network Performance of ROADM Architecture Enabled by Novel Wideband-integrated WSS. In *GLOBECOM 2022 - 2022 IEEE Global Communications Conference*, pages 2945–2950. IEEE, dec 2022

26. Muhammad Umar Masood, Lorenzo Tunesi, Ihtesham Khan, Bruno Correia, Enrico Ghillino, Paolo Bardella, Andrea Carena, and Vittorio Curri. Network performance analysis of a PIC-based reconfigurable add-drop multiplexer for multiband applications. In *Next-Generation Optical Communication: Components, Sub-Systems, and Systems XII*, volume 12429, pages 81–86, San Francisco, California, mar 2023. SPIE

27. Bruno Correia, Rasoul Sadeghi, Antonio Napoli, Nelson Costa, João Pedro, and Vittorio Curri. C+L+S-Band Optical Network Design Exploiting Amplifier Site Upgrade Strategies | IEEE Conference Publication | IEEE Xplore. In *2023 International Conference on Optical Network Design and Modeling (ONDM)*, pages 1–6, Coimbra, 2023

28. Rasoul Sadeghi, Bruno Correia, Elliot London, Antonio Napoli, Nelson Costa, João Pedro, and Vittorio Curri. Performance comparison of optical networks exploiting multiple and extended bands and leveraging reinforcement learning. In *2023 International Conference on Optical Network Design and Modeling (ONDM)*, pages 1–6, 2023

Chapter 1

Introduction

In a world growing more connected and relying on technologies that requires an increasing data traffic exchange, optical networks are essential to support that demand. In this thesis, we present our novel contributions in the context of modelling and evaluation of ultra-wide band (UWB) systems in optical networks. Particularly, we report our results regarding UWB input power optimization going beyond C+L systems. Moreover, we present an optical network design analysis applied to the UWB context, showing the requirements in terms of costs for the deployment of such systems, with comparable performance as the nowadays C-band systems.

This thesis is organized as follows: In Chapter 1 we describe the optical communication and network development, from the first installed systems to the most advanced ones. Moreover, we present the main research topics, which represents the possible solutions for future optical network technologies. Next, the optical transmission modelling is described in Chapter 2. The main components and their effects, which take place in this type of transmission, are presented in details. Moreover, a briefly overview of the optical networks hierarchy, softwarization and disaggregation concepts are shown. Finally, Chapter 2 describes in details the opportunities and challenges of UWB transmission systems, highlighting the differences from conventional C-band systems. In Chapter 3 is presented the first set of published results carried out during our work, tackling the problem of launch power optimization applied to UWB systems. In this chapter, we start by evaluating the impact of launch power in systems performance and later we shown our results, applying for each spectral band a different tilt and offset, using two different strategies, in order to

maximize system performance. Chapter 4 starts by modelling a potential network upgrade using a specific amplification type, providing a capacity increasing with minimum impact on systems already in use. Later we showed a comparison between two possible bands upgrades, analyzing also their impact, in both OLS and network levels. Finally, is presented a optical network design algorithm for UWB, showing a tradeoff between capacity and overall network costs. Finally, in Chapter 5 we report our main conclusions.

1.1 Evolution of optical communications and networks

The history of optical communications can be traced back several centuries, with significant milestones and developments shaping the field. Early experiments in optical signaling involved the use of semaphore systems, which relied on visual cues to transmit messages over long distances. One notable figure in this era was Claude Chappe, who developed a network of optical telegraphs consisting of towers with movable arms that could convey messages across vast distances. The first system developed by the French engineer, between the cities of Paris and Lille with distance of 230 km, was able to transmit a complete message in less than a hour, a remarkable duration for that period [34].

The true breakthrough in optical communications base on fiber transmission came mainly with the advent of two elements in the 1960's. The first one was the invention of the laser, an acronym for Light Amplification by Stimulated Emission of Radiation, build for the first time in 1960 at Hughes Research Laboratories based on the work of A. L. Schawlow and C. H. Townes [35]. The second breakthrough came with the advent of optical fibers. In the beginning, researchers did not believe that fibers could be used for optical transmission due to the higher losses of such elements. This changed when the idea, based in Charles Kao's pioneering work on the transmission of light in fibers which earned him a Nobel Prize in 2009, of fibers with losses bellow 20 dB/km were possible to be fabricated, if the impurities of the silica glass were removed. This loss was archived in 1970 at Corning Glass Works, making the fiber low-loss and high-bandwidth characteristics ideal for transmitting light signals over long distances. Afterwards, fiber losses achieved values of around 1.0 dB/km operating in the region of 1300 nm. Finally, in 1979 the NTT Ibaraki Electrical Communication Laboratory achieve the close to limit loss of 0.2 dB/km at

1550 nm [36], showing the superiority of optical fibers over traditional copper-based communication systems in terms of bandwidth, signal quality, and resistance to electromagnetic interference.

The introduction of the first commercial fiber optic communication systems, known as first generation, occurred in the 80's. These systems operate near the 800 nm region using GaAs semiconductor lasers with bit rate up to 45 Mbps, requiring repeaters after 10 km. Next, systems started to use the region of 1300 nm, due to the lower losses and minimum dispersion of that region. This second generation of optical systems became available in the early 80's with bit-rate up to 100 Mbps for multimode fibers and up to 2 Gbps for single-mode fibers, with repeaters spacing around 50 km. The third generation of optical systems operate in the region of 1550 nm, as this region is where fibers presents the lower attenuation window [37]. In contrast, this region presents a large fiber dispersion, causing the spread of the laser pulse, factor in which conventional InGaAsP semiconductor lasers could not work properly. The solution proposed was the usage of dispersion-compensating fiber (DCF), presenting the minimum dispersion around that wavelength, as well as limiting the laser spectrum to a single longitudinal mode [34]. Combining these solutions, commercially optical systems operating at 1550 nm started to be deployed with bit-rate up to 10 Gbps with repeaters spread between 60 and 70 km apart. Following that, two main advances were important to the development of the fourth generation of optical systems. The first one was the application of wavelength-division multiplexing (WDM), approach that can multiplex several signals generated by different sources, each signal using a specific frequency, into a single comb to be transmitted together over the fiber [38]. WDM grown up from less than 10 to more than 100 channels at the time, and it is still used in modern optical networks. Even with higher spectral usage provided by WDM, the requirement of periodic repeaters was a drawback in optical systems. These repeaters were used to apply the optical-electrical-optical (O-E-O) regeneration, requiring a high electrical consumption and large number of equipment. The development of erbium doped fiber amplifiers (EDFAs) overcome this constraint, providing optical amplification without the requirement of O-E-O. These devices were composed by a fiber doped with the rare earth element erbium, which is pumped to an excited state, being capable to perform the amplification of multiple signals at many frequencies simultaneously. The commercially available optical systems using both WDM and EDFA started to be deployed in the beginning of the 90's, achieving the remarkable distance of

21000 km at 2.5 Gbps per channel [39]. This advance allowed intercontinental transmission using submarine cables and supported the Internet develop, with the first of these systems being deployed in middle 90's. The fifth generation was introduced with the deployment of more complex modulation schemes like quadrature amplitude modulation (QAM), which were able to modulate the signal in amplitude, phase and polarization. Moreover, the DCF were replaced by standard single-mode fibers (SSMFs) operating in C-band, as the receiver was capable to digitally compensate the dispersion through digital signal processor (DSP) [40]. Finally, the development of reconfigurable optical add-drop multiplexers (ROADMs) transformed the optical networks from point-to-point connections to a fully optically transparent systems. These devices enabled signals between source and destination to be transparently routed through several optical nodes, increasing the flexibility of such systems, leading to faster network speeds, reduced latency, and improved energy efficiency. This optical systems generation scale up from 10 to up to 400 Gb/s per channel, showing a huge capacity increasing provided by optical networks [41].

1.2 Challenges and trends of optical networks

The continuous increase in traffic demand [42] has become a significant challenge in the field of telecommunications. The deployment of 5G networks has introduced a new era of connectivity, enabling high-speed wireless communication, ultra-low latency, and massive device connectivity [43–45]. This technology has unlocked new possibilities, including autonomous vehicles, smart cities, and Internet of Things (IoT) applications. However, the deployment of 5G networks has also led to a surge in data traffic, requiring robust infrastructure and network capacity to handle the massive volume of data generated by 5G-enabled devices. Moreover, data center interconnection is another key driver of increasing traffic demand [46]. As organizations increasingly rely on cloud-based services, the demand for data centers and their interconnection has skyrocketed. These data centers serve as hubs for storing, processing, and delivering vast amounts of data. As a result, data center operators are continually expanding their infrastructure and upgrading their networks to cope with the escalating demand for interconnection services. Finally, the growth of IP traffic [42], driven by the increasing use of digital services and applications, has further fueled the demand for network capacity. The proliferation of video

streaming, social media platforms, e-commerce, and cloud-based services has led to an explosion in IP traffic. This surge in data requires robust and scalable networks capable of handling the ever-increasing bandwidth requirements. Network operators are continually investing in upgrading their infrastructure, deploying advanced optical technologies, and optimizing their routing and switching architectures to accommodate the surge in IP traffic.

To cope with that traffic demand, several technologies are being applied or being developed in order to increase optical systems capacity. Advanced DSP techniques can compensate for several transmission impairments, such as chromatic dispersion (CD) and polarization-mode dispersion (PMD) among others [40]. Additionally to that, more efficient modulation formats using probabilistic shaping (PS) can bring fiber transmission capacity even closer to the theoretic Shannon limit [47–49]. Combining these aspects with flexible rate transceivers, system are being commercially available providing capacity up to 800 Gbps per channel [50]. Another development is the spatial-division multiplexing (SDM) technique [51, 52], applying multi-core, multi-mode and/or multi-fibers, in order to increase the number of network channels per link. These technique is based in parallel systems, expanding the channels cardinality based on the number of fiber, modes or cores. Nowadays, only multi-fiber SDM is commercially available, as it is based on already mature technology of C-band systems. SDM based on core or modes are still in research stage, with several field trials providing great potential [53, 54] as long-term solution, as it will require the upgrade of the whole fiber infrastructure already installed. In recent years, the possibility to transmit beyond C-band gained attention in both academia and industry, called UWB, band-division multiplexing (BDM) or MBT [55]. This technique is already commercially available, expanding the used bandwidth to C+L-bands, from 4.8 THz (C-band) to 9.6 Thz, doubling the fiber capacity [56]. Furthermore, MBT could achieve even higher spectral usage, as the SSMF bandwidth presents a low-loss window of more than 50 THz, going from U- to O-bands, presenting a huge spectral potential. MBT systems are the main topic os this thesis, focusing on the benefits and challenges provided by this approach, which will be described in details in Chapter 2.

Chapter 2

Physical layer modelling, optical network architecture and multi-band systems

In this chapter, we introduce the fundamental concepts of modern optical transmission systems, which are based on WDM with dual-polarization (DP) coherent technologies. We start by listing the main components of these systems, describing in details how they operate. Next, we detail all the physical impairments raised by these components during the optical transmission, focusing on the assumption that WDM optical data transport can be simplified by approximating transparent lightpaths as DP additive white and Gaussian noise channels [57]. Next, in Section 2.2, is presented the details of optical network architectures. In this section, three main concepts are described: (1) firstly is presented a generic overview of the geographic hierarchy of optical networks nowadays; (2) secondly, we tackle the concept of SDN, which among other things provides a decoupling of the control plane from the date place, as well as enabling programmability for network application development [58], and (3) finally we describe the idea of network disaggregation, enabling interoperability between network elements, possibly from multi-vendors. In the last section, the main concepts of UWB optical networks [55] are presented, describing the main differences regarding transmission modelling as well as component requirements for the deployment and usage of these systems.

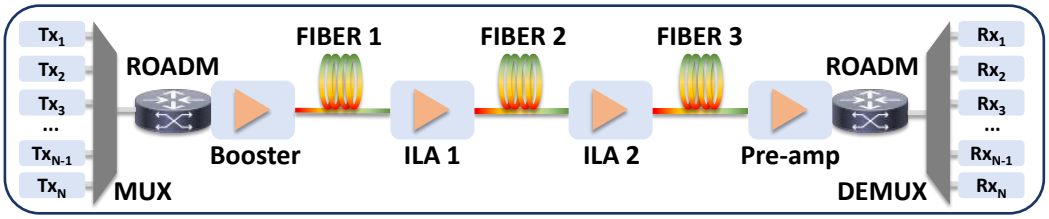

Fig. 2.1 Illustration of an OLS and its main components.

2.1 Optical transmission modelling

In Figure 2.1 is presented a OLS schematics, composed by several devices. First, most left part of the Figure 2.1, are the N transmitters, which are responsible to convert the electrical signal to the optical domain in order to transmit over the optical fibers. Details of this procedure are presented in Section 2.1.1. All the signals, each one using a different frequency, are then multiplexed, as already mentioned in Section 1.1. After multiplexing, the signals are routed through a ROADM node, which usually connect several fibers. After pass the ROADM, a sequency of amplifiers and fiber follows, with the formers being responsible to compensate for the signal degradation (described in Section 2.1.3) and the later responsible for carrying the signal over a fixed distance (described in Section 2.1.2). At the last part of the transmission, the signals are routed to other fibers (connected to the last ROADM) or demultiplexed and sended to the N receivers, in order to be converted to digital domain.

2.1.1 Coherent Transmitter/Receiver

Modern optical transmitters apply the coherent multi-level modulation format transceivers, in which both the in-phase (I) and quadrature (Q) components of each of two orthogonal polarizations (X and Y) of an optical carrier are modulated. Figure 2.2a presents the basic structure of this device, composed by the a laser source, polarization beam splitters (PBSs) and Mach-Zehnder modulators (MZMs). The PBSs are responsible for separate the laser beam into vertically and horizontally polarized beams. For each polarization, both I/Q components are modulated. Finally, the both polarizations are combined by a PBS. By proper tuning the laser frequency, we can transmit the signal centered in frequency (f), being able to use the WDM

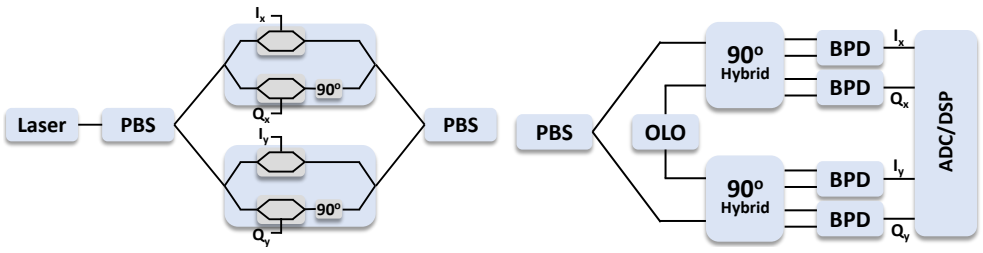

(a) (b)

Fig. 2.2 Structure of coherent (a) transmitter and (b) receiver.

technique to transmit several channel together [40]. The receiver side, shown by Figure 2.2b, is composed by a PBS applied to the incoming signal, again splitting it in both polarizations [59]. Each polarization is mixed with a reference optical carrier, that is provided by an optical local oscillator (OLO), by a 90^o optical hybrid. The optical hybrid is a passive optical device that consists of two primary input ports and four output ports. It is constructed using 3 dB couplers and a 90^o phase rotator. At the output of the optical hybrid, each two pairs of electric fields components are combined by balanced photodetectors (BPDs), producing the in-phase an quadrature components of each polarization. The fours components are sent to an analog-to-digital converter (ADC) and later to the DSP [40]. The latter is composed by several stages, responsible for recovering the phase and amplitude of the signals, as well as perform impairment compensation, such as chromatic dispersion and the polarization-mode dispersion [60].

2.1.2 Fiber impairment modelling

Fiber attenuation

In optical transmission systems, attenuation is a fundamental propagation effect that leads to a linear reduction in the power of the light propagating through the fiber. It is caused by several factors: the Rayleigh scattering, the violent and infra-red absorption, the OH-ion absorption peaks at approximately 1.25 and 1.39 μm, and the absorption due to phosphorous within the fiber core [61]. The attenuation of the fiber is fully characterized by an attenuation coefficient (α), usually given in dB/km [34]. It is important to note that attenuation is not constant across all frequencies and can vary with the frequency of the transmitted light. Hence, when dealing with a wide

range of frequencies, as it is used in WDM transmission, it becomes necessary to consider attenuation as a function of frequency, denoted as $\alpha(f)$. The power at the output of the fiber (after propagation) is given by:

$$P_{out}(f) = P_{in}(f)e^{-2\alpha(f)L_s} \tag{2.1}$$

where P_{in} and P_{out} represents the input and output powers, respectively, for channel centered in frequency f, while L_s is the fiber length.

Chromatic dispersion

Chromatic dispersion is a well-known phenomenon in optical transmission systems. It refers to the broadening of optical pulses as they propagate through an optical fiber due to the wavelength-dependent refractive index of the medium [34]. This dispersion can lead to pulse spreading, limiting the achievable data rates and transmission distances [62]. The effect of chromatic dispersion can be mathematically described by expanding the propagation constant using a Taylor series. The propagation constant, denoted as β, represents the phase constant of the optical signal and is a function of the angular frequency ω. Presenting the Taylor expansion of β provided in [34] in frequency, in which $\omega = 2\pi f$, we obtain:

$$\beta(f) = \beta_0 + 2\pi\beta_1(f - f_0) + 2\pi^2\beta_2(f - f_0)^2 + \frac{4}{3}\pi^3\beta_3(f - f_0)^3 \tag{2.2}$$

in which f_0 is the reference frequency of the Taylor expansion. Equation 2.2 describe the frequency components propagate at different speed within an optical channel. β_0 represents a phase shit and β_1 represents a propagation delay. These parameters do not affect the QoT, remaining β_2 and β_3 responsible for pulse broadening called group-velocity dispersion (GVD), consequently having a potential impact in QoT. β_2, given in $\mathrm{ps}^2/\mathrm{km}$, represents the GVD parameter and it is related to the actual dispersion parameter D as:

$$\beta_2(f) = -\frac{c}{2\pi f^2}D(f) \tag{2.3}$$

where c is the speed of light in vacuum. The dispersion parameter D $(\mathrm{ps}/(\mathrm{nm}\cdot\mathrm{km}))$ determines the magnitude and sign of chromatic dispersion. Positive dispersion ($D > 0$) causes longer wavelengths to propagate slower than shorter wavelengths, resulting

in pulse broadening. Conversely, negative dispersion ($D < 0$) leads to shorter wavelengths traveling slower, resulting in pulse compression. In practical applications, fiber manufacturers provides the D parameters within fiber data sheets. Finally, based on [34], the third order term β_3 is related to the dispersion slope S and is given by:

$$\beta_3(f) = \frac{c}{2\pi f^2} S(f) - \frac{2f}{c} \beta_2(f) \tag{2.4}$$

In practical applications, however, fiber manufacturers provide only S_0 in $\mathrm{ps}/(\mathrm{nm}^2 \cdot \mathrm{km})$ for the zero dispersion frequency [3]. Both second and third order dispersion parameters are crucial to modelling the fiber propagation, as they interact with the Kerr effect and consequently impacting the QoT. Overall, in coherent systems the CD can be fully compensated the accumulate dispersion by DSP at the receiver side, defined by the transceivers maximum tolerable CD [39].

Polarization-mode dispersion

PMD is a significant impairment in optical transmission systems that arises due to the birefringence in optical fibers. It refers to the differential delay experienced by two orthogonal polarization states of light as they propagate through the fiber, even when transmitting in single-mode fibers [63]. The occurrence of PMD is primarily caused by small departures from cylindrical symmetry, resulting from random variations in the core shape along the fiber length. These variations break the mode degeneracy and lead to a mixing of the two polarization states [34]. In coherent transmission, however, PMD does not significantly affect the signal quality of transmission as it can be fully compensated by DSP techniques at the receiver side. By employing advanced algorithms and adaptive equalizers, the adverse effects of PMD can be effectively mitigated, allowing for reliable data recovery. In practical scenarios, the maximum tolerable PMD for transceivers is defined by vendors based on their system specifications and design considerations. These specifications provide guidelines for system deployment and ensure reliable operation within specified performance bounds [57].

Polarization dependent loss

Polarization dependent loss (PDL) is a notable phenomenon observed in optical transmission systems, resulting in power attenuation experienced by an optical signal due to the polarization state of light as it propagates through an optical component or fiber link [64]. The polarization-dependent characteristics of optical components, such as optical amplifiers (OAs) and ROADMs, contribute to the varying response of the component or link to different polarization states, leading to differential attenuation and a loss imbalance between the two orthogonal polarizations [65]. The presence of PDL can introduce power imbalances between the two orthogonal polarization states, leading to signal degradation and performance limitations in optical communication systems. It is essential to quantify PDL to assess its impact accurately. PDL is typically expressed in decibels (dB) and measured as the maximum difference in power loss between the two orthogonal polarization states [57]. This parameter is commonly referred to as the PDL coefficient.

Stimulated Raman Scattering

Stimulatted Raman scattering (SRS) is a nonlinear phenomenon that occurs in optical transmission systems. It arises from the interaction between the propagating optical signal and the molecular vibrations within the fiber medium. In the context of WDM systems, SRS can significantly impact their performance by facilitating the transfer of energy from one channel to the neighboring channels [62]. This energy transfer predominantly occurs from higher frequency channels to lower frequency channels, leading to a power tilt across the transmitted WDM spectrum [66]. Furthermore, it is worth noting that the SRS effect can also be exploited for Raman amplification applications [67]. Raman amplification involves the introduction of a high-power pump laser into the fiber alongside the signal, resulting in signal amplification through the energy transfer facilitated by SRS [68].

The key parameter characterizing this effect is the Raman gain coefficient (C_r), which describes the growth of Stokes power as pump power is transferred to it through SRS. The power evolution produced by the SRS effect for a single channel centered in frequency f within the WDM comb can be described by the following

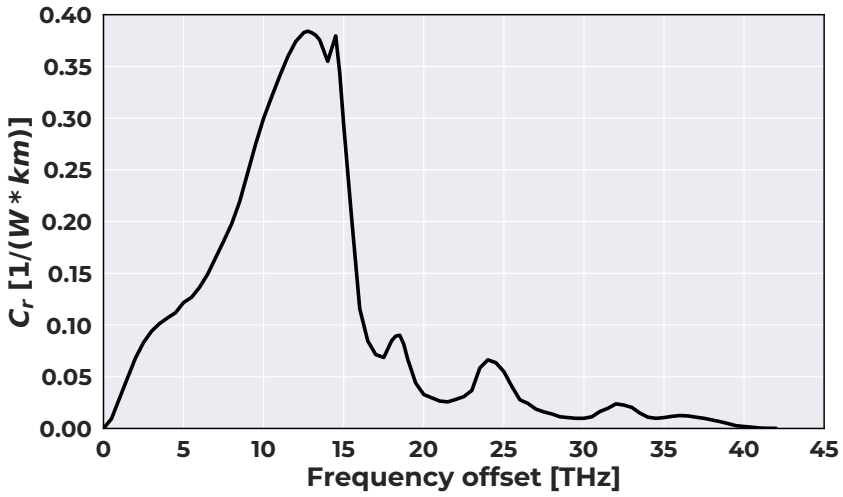

Fig. 2.3 Experimental Raman gain coefficient of SSMF.

equation:

$$\begin{aligned}\frac{\partial P(f,z)}{\partial z} &= -\alpha P(f,z) - P(f,z)\sum_{f>f_m} C_r(|f-f_m|)P(f_m,z) \\ &\quad + P(f,z)\sum_{f<f_m} C_r(|f-f_m|)P(f_m,z)\end{aligned} \tag{2.5}$$

where $P(f,z)$ is the power evolution along z and f_m represents all the WDM comb channels besides the evaluated one. By Equation 2.5, it is clear that the channel will loose power for the channels on the left part in spectrum (represented by $f > f_m$) while it will gain power from the channels on the right side of the WDM comb ($f < f_m$).

An experimental characterization of the Raman gain profile for SSMF is presented in Figure 2.3, illustrating the frequency offset between the pump channel and the signal. The peak of the SRS effect is observed around a frequency offset of 13 THz, although the taylor of the Raman gain effect can be observed up to 40 THz. The literature also provides various Raman gain profiles for different fiber types [66]. Given the prominent gain peak around 13 THz, SRS becomes particularly critical in UWB systems, as discussed in Section 2.3 and analyzed further in Section 3.1. Overall, understanding and managing the impact of SRS on optical transmission systems are crucial for achieving efficiency and reliability.

Kerr effect

The Kerr effect is a nonlinear phenomenon in optical transmission that arises due to the response of the optical medium to the intensity of light. In optical transmission systems, the Kerr effect can cause various nonlinear impairments, such as self-phase modulation (SPM), cross-phase modulation (XPM), and four-wave mixing (FWM). SPM is a phase shit caused by the change in refractive index as the signal propagates through the fiber. XPM is caused when one signal affects the phase of another one, both transmitted alongside each other. Finally, FWM when the the intensity of two or more signals combines in a nonlinear medium, producing signals in a different frequency. These effects can lead to distortions and interferences in the transmitted signal, resulting in degradation of the overall system performance [69]. The kerr effect is included in the nonlinear Schrödinger equation (NLSE) [70], which describe the propagation of an optical signal traveling through the fiber. In order to facilitate the nonlinear interference (NLI) estimation, we can simplify the NLSE using the spectrally separated Manakov equation (SSME) by neglecting the PMD introduced by the fiber propagation [71]. A general form to estimate the NLI power, split into the three different contributions, is given as follows:

$$\begin{aligned} P_{\mathrm{NLI}}(f) &= P_{\mathrm{SPM}}(f) + P_{\mathrm{XPM}}(f) + P_{\mathrm{FWM}}(f) \\ &= \eta_{\mathrm{SPM}} P(f)^3 + \sum_{f \neq f_m} \eta_{\mathrm{XPM},f_m} P(f) P(f_m)^2 \\ &\quad + \sum_{f_i, f_j, f_k \in \mathrm{FWM}, f} \eta_{\mathrm{FWM},f_i f_j f_k} P(f_i) P(f_j) P(f_k) \end{aligned} \tag{2.6}$$

where the index $\eta_{\mathrm{SPM},f}$, η_{XPM,ff_m} and $\eta_{\mathrm{FWM},ff_if_jf_k}$ represent the efficiency for SPM, XPM and FWM, respectively, with their respective frequency channel combinations. In most cases, due to its decay with channel spacing, large channel symbol rates and larger fiber dispersion, the FWM can be neglected, remaining SPM and XPM as the main contribution to NLI [72, 73]. Several mathematical models proposed in the literature rely on different approaches and approximations for ηs computation, considering the entire link or for a given propagating channel comb [57].

In modern optical networks, where coherent multi-level modulated signals traverse uncompensated optical links, the overall impact of NLI on the signal can be characterized as the introduction of phase noise and additive Gaussian noise. Based on this assumption, plus that the signals are Gaussian distributed and the non-linearity

is a perturbation of the propagating electric field [74], the Gaussian noise (GN)-model was proposed [75–78]. The GN-model provides a conservative estimation of the produced NLI, being experimentally validated for several scenarios [79, 80]. On the other hand, when we consider a wider spectral bandwidth, where the SRS effect is dominant, the most suitable NLI estimation is given by the generalized Gaussian-noise (GGN) [81, 82]. This GN derivation incorporate the SRS power evolution (Equation 2.5) to the NLI estimation. Using the GGN, we can write the η (Eq. 2.6) for SPM and XPM (for a single interfering channel in frequency f_m) contributions as [3]:

$$\eta_{\text{SPM}}(f) = \frac{\gamma(f)^2}{R_s^3(f)} W_{SPM} I_f^f(L_s) \tag{2.7}$$

$$\eta_{\text{XPM},f_m}(f) = \frac{\gamma(f)^2}{R_s(f)R_s(f_m)^2} W_{XPM} I_{f_m}^f(L_s) \tag{2.8}$$

where $\gamma(f)$ is the nonlinear coefficient of the channel under test (CUT) centered in frequency f, $W_{XPM} = 2\frac{16}{27}$ represents the XPM weight and $W_{\text{SPM}} = (1+C_\infty)\frac{16}{27}$ the SPM weight, both coming from the statistics and the polarization. The GGN provides a disaggregated NLI model, computing the NLI contribution at each fiber span for each channel separated. This capacity of separate the contribution per channel/span is known as spectrally (channel) and spatially (span) disaggregation [83]. The spatial disaggregation requires consideration of the coherent accumulation of the SPM, which is achieved by the C_∞ coefficient and represents the maximum amount of SPM that may be generated in a single span for a specific configuration [84, 85]. Finally, Eq. 26 of [3] provides the description of $I_{f_m}^f(L_s)$, where in Eq. 27 of [3] is shown the inclusion of the term $\rho(f,z)$, which represents the power evolution of the channel centered in frequency f along the z-axis. Following that approach, we can compute the NLI as individual contributions, from all the other channels in the WDM comb as well as the channel itself, taking into consideration the SRS affect which, as discussed in Section 3.1, is the dominant effect in MBT scenarios.

2.1.3 Amplification modelling

OA plays a crucial role in optical transmission systems, as they enhance the signal power without the need for conversion to the electrical domain. The amplifiers, and their respective terminology, are defined by their position within the OLS (shown in Figure 2.1): (1) booster amplifiers placed right after the ROADM, aiming to

compensate the losses raised in these devices; (2) Inline amplifiers (ILAs) responsible for compensation of power depletion during the fiber transmission; (3) Pre-amps, placed right before the receivers, responsible for improving the signal-to-noise ratio (SNR) and enhance the detection sensitivity of these devices, ensuring accurate and reliable signal detection. In optical communications, three types of amplifiers can be used to compensate the power loss. The first type are semiconductor optical amplifiers (SOAs), which are active devices based on semiconductor materials that provide amplification to optical signals through the injection of current and exhibit a wide range of applications in optical communication systems [86]. Secondly are the doped fiber amplifiers (DFAs), which are the most common type of amplification used in optical transmission. DFAs employ a length of fiber doped with rare-earth ions to provide amplification to optical signals through stimulated emission [87]. Finally, as briefly described in 2.1.2, Raman amplification can be used to compensate the signal power depletion, using the SRS effect to transfer power from high power pumps to the desired signals [67]. To accurately model optical amplification, it is important to consider the amplified spontaneous emission (ASE) power generated by the all amplifier types. ASE is a phenomenon in which spontaneous emission occurs in the gain medium of the amplifier, leading to the generation of noise that degrades the signal quality [3]. The ASE power of the channel centered in frequency f is directly related to the gain (G) and noise-figure (NF) of the amplifier and can be mathematically expressed as follows:

$$P_{\text{ASE}}(f) = hf(G(f) - 1)\text{NF}(f)B_{\text{ref}} \tag{2.9}$$

where h is the Planck constant and B_{ref} is the reference noise bandwidth, which is equal to the channel symbol rate $R_s(f)$ or a predefined value. Accurately modeling the ASE power is crucial for analyzing the SNR and the overall performance of optical transmission systems. A detailed explanation on how the ASE power is used to compute the system QoT is presented in Section 2.2.3.

2.2 Optical network architecture

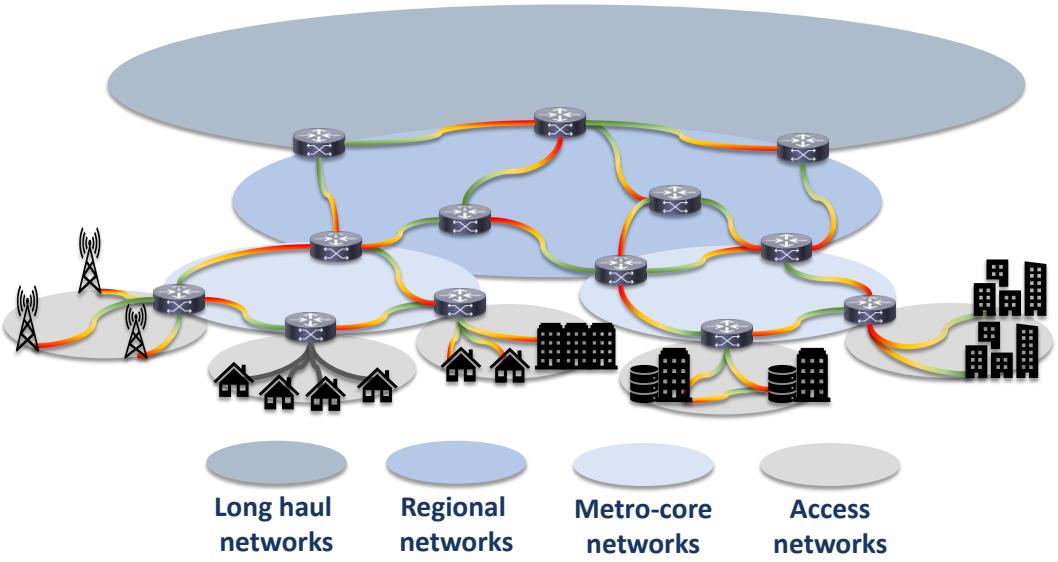

Fig. 2.4 General optical network hierarchy.

2.2.1 Optical networks geographic hierarchy

In Figure 2.4 we present a illustration of the general optical network hierarchy. Starting by the higher level, long haul (or backbone) optical networks are responsible for the transmission of high-capacity optical signals over long distances, typically spanning hundreds or even thousands of kilometers [88]. These networks use high-performance optical transmission systems, such as dense wavelength-division multiplexing (DWDM), to achieve long reach and maximize the overall system capacity. Regional networks connect various cities and towns within a specific geographic region. They serve as intermediaries between long haul networks and metro networks, providing connectivity between major metropolitan areas. Regional networks often employ optical transport technologies, including optical amplifiers and wavelength selective switches, to efficiently route and manage traffic flows. The design of regional networks focuses on minimizing latency, maximizing capacity, and ensuring reliable connectivity between different regional hubs. Metro networks, also known as metropolitan area networks, operate within a metropolitan region, serving as a bridge between regional networks and access networks. This network level employ advanced optical technologies, such as ROADMs, to enable flexible and dynamic traffic routing. The design of metro networks emphasizes low latency, high scalability, and efficient traffic grooming to accommodate the growing demand for high-bandwidth services [38]. Finally, access networks represent the final link

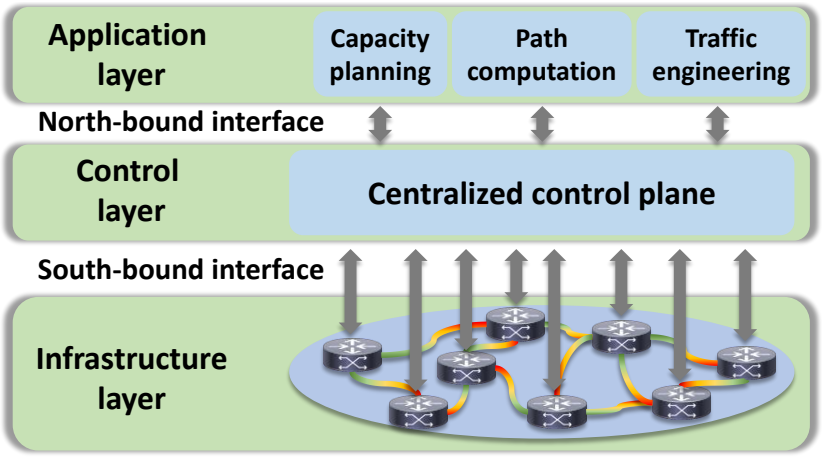

Fig. 2.5 SDN model, composed by three layers: Infrastructure, control and application layers.

in the optical network hierarchy, providing connectivity to end-users, enterprises, and residential areas, as shown in Figure 2.4. These networks encompass various access technologies, such as passive optical networks (PONs) [89, 90] and Ethernet-based solutions [91], to deliver high-speed internet access, video streaming, and other services. Access networks face unique challenges, including fiber deployment to individual premises, power budget limitations, and the need for cost-effective solutions.

2.2.2 SDN and disaggregated optical networks

Software-defined networking have emerged as a promising paradigm for enhancing the flexibility, scalability, and manageability of modern optical networks. They provide a centralized and programmable control plane that separates the control and data planes in network architectures. By decoupling network control from forwarding functions, SDNs enable dynamic network management and provisioning, as well as the implementation of network-wide policies and services [58, 92]. The structure of the SDN is based on three layers, as shown in Figure 2.5. The bottom one, called infrastructure layer, is composed by the elements of the network, such as routes and switches. This layer is responsible to collect and store the network status, like topology and traffic statistics, and send them to the control layer [93]. This information is transmitted by the so called south-bound interface, responsible for this interaction between infrastructure and the upper layer. On top of that is the controller layer, which will be responsible to communicate with the data plane

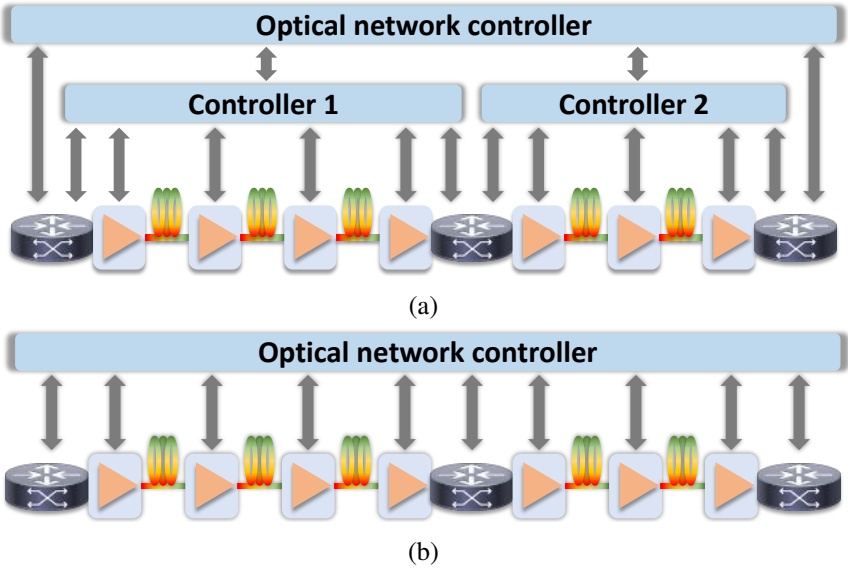

Fig. 2.6 Concept of (a) partially (composed by two OLS controllers from different vendors), and (b) fully-disaggregated networks.

through specific functions, enabling the control of infrastructure layer devices. This layer will interact with the upper layer through the so called north-bound interface, providing service access points in various forms. Moreover, this layer can dialogue with others control layers, as the network can be divided between several of them. Finally we have the application layer, containing SDN applications designed to fulfill user requirements [58]. These applications include capacity planning, path computation, traffic engineering among others.

In the context of SDN, is possible to apply the concept of disaggregated optical networks, in which possible multi-vendor network element (NE), such as amplifiers, ROADMs and transceivers, can be controlled independently (fully disaggregated) or entire OLSs are controlled independently (partially disaggregated) [57]. This multi-vendor elements or systems uses a vendor-agnostic protocols, enabling controlling of different systems implementations [94]. Figure 2.6 presents a illustration of how partially and fully-disaggregated network operates. Using this interoperability of these systems, the central optical network control can provide control and management capability of hardware equipment and the overall network, including configuration, performance monitoring, and alarm management [46]. For the rest of this work, we made use of the assumption of a fully-disaggregated optical network, in which all the OLS configuration are set by a unified control plane.

2.2.3 Optical transport model and QoT metric

Based on a open and disaggregated approach, the optical transport network can be modeled by approximating transparent lightpaths as DP additive white and Gaussian noise channels [57]. This equivalent Gaussian disturbance includes both the ASE noise and NLI accumulated over the entire lightpath [1]. In Figure 2.7 is presented the models for amplification, fiber transmission and for the lightpath (LP) traversing several links and nodes within the network. For the amplification case, the channel power at the input of the device is amplified ($G(f)$) and the ASE noise is added. Moving forward to the fiber transmission, the NLI power is added to the incoming signal, provided by equation 2.6. After, the attenuation profile (in our case considering the SRS effect – G_{SRS}) is applied to the signal, in which $G_{\text{SRS}} = \frac{P(f,L_s)}{P(f,0)}$, where L_s is the fiber length. To obtain the output power after the fiber propagation, we use the set of equations (all channels) shown in Equation 2.5. With both disturbance included and the assumption of a DP additive white and Gaussian noise channels, we can model the QoT of each fiber span (s), composed by fiber and amplifier, by the signal-to-noise ratio (GSNR) [95, 96], given by:

$$\text{GSNR}_s(f) = \frac{P(f)}{P_{\text{ASE}}(f) + P_{\text{NLI}}(f)} = (\text{OSNR}(f)^{-1} + \text{SNR}_{\text{NL}}(f)^{-1})^{-1} \tag{2.10}$$

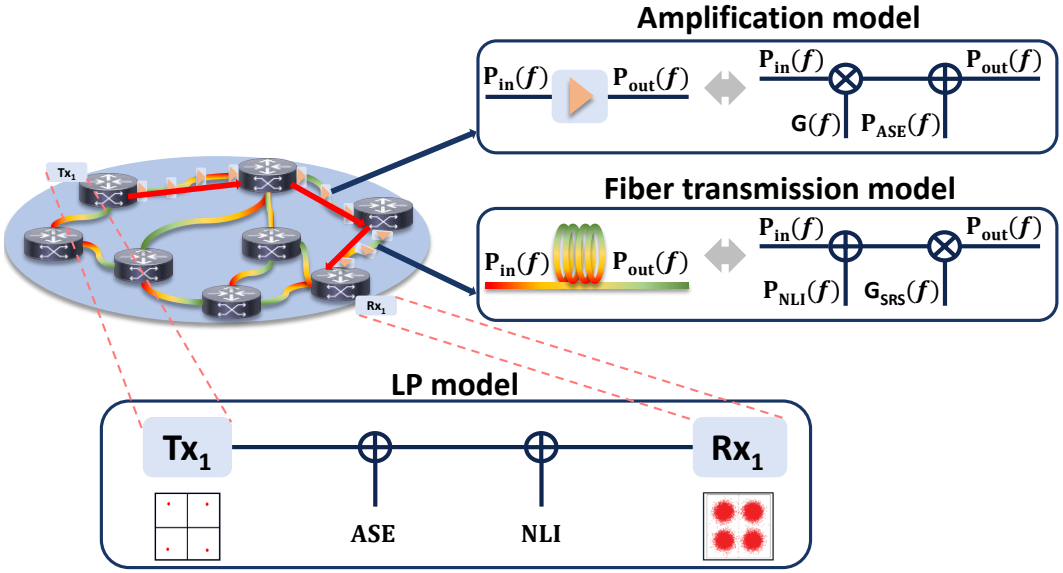

Fig. 2.7 Models for amplification, fiber transmission and total LP.

where the optical signal-to-noise ratio is $\mathrm{OSNR}(f) = \frac{P(f)}{P_{\mathrm{ASE}}(f)}$ and the nonlinear signal-to-noise ratio is $\mathrm{SNR}_{\mathrm{NL}}(f) = \frac{P(f)}{P_{\mathrm{NLI}}(f)}$. In order to compute the QoT for each network link (l), we define the GSNR as:

$$\mathrm{GSNR}_l(f) = \left(\sum_{s \in l} \mathrm{GSNR}_s^{-1}(f) \right)^{-1} \tag{2.11}$$

Finally, we can evaluate the GSNR for a entire LP between two nodes, as shown in Figure 2.7 for three network links an four nodes, as follows:

$$\mathrm{GSNR}(f) = \left(\sum_{l \in \mathrm{LP}} \mathrm{GSNR}_l^{-1}(f) \right)^{-1} \tag{2.12}$$

Hence, to simplify the representation of the optical network, a weighted graph can be employed, as depicted in Figure 2.7. In this graph, each node corresponds to a ROADM node, and each edge represents a link between nodes, with the weight assigned based on the contribution of the link's GSNR. By utilizing this network abstraction, it becomes possible to evaluate the overall GSNR from the source to the destination by summing up the GSNR contributions of all the links along the selected path, as described in Equation 2.12.

In order to apply the concepts previously described, in this work we made use of the Gaussian noise simulation in Python (GNPy) [96–98, 57, 78] QoT estimator (QoT-E). GNPy is a software developed by Telecom Infra Project (TIP) in order to serve as a common, open source, and vendor-neutral set of algorithms to assess the optical impairments in an open optical line system [95]. GNPy uses the network input parameters, such as fiber parameters, amplifiers characteristics, and network physical topology description, to compute the GSNR for a specific path within this network, considering all the noise contributions detailed in this section. In order to assess the network performance, we use the GNPy weighted graph into statistical network assessment process (SNAP) framework [99]. SNAP performs a Monte Carlo analysis (MCA) by generating several realizations of progressive random traffic requests coming from the logical to the optical transmission layer. It statistically test the network load with possibly different traffic models [1] or resource allocation policies, such as independent routing and wavelength assignment (WA) algorithms. Figure 2.8 illustrate the network assessment workflow using SNAP. SNAP three types of parameters which can be set independently. The first parameters refer to

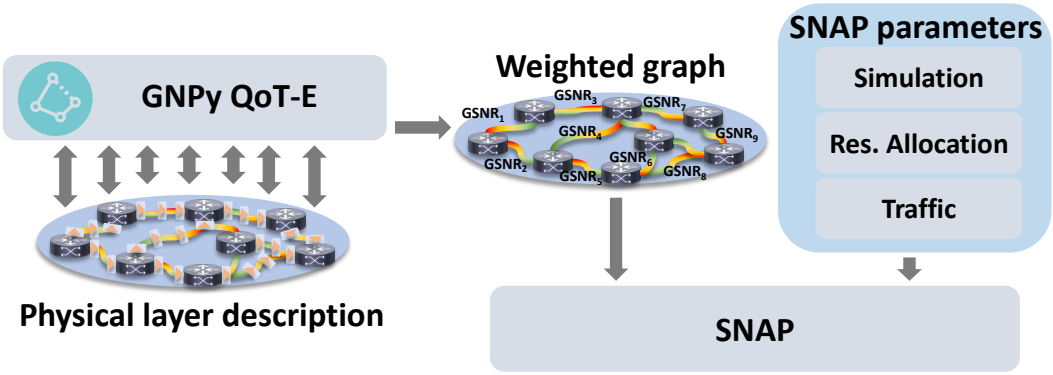

Fig. 2.8 SNAP workflow.

the simulation itself, options like threshold blocking-probability (BP), number of Monte Carlo iterations, and possibility of LP regeneration [100, 101]. The second set of parameters define the resource allocation policies, like routing [102, 103], WA [104] and how the connections are routed in ROADMs [105, 106]. Finally, we have the traffic parameters, which will define how the traffic is performed, like new connection per bit rate or per LP, the size of each connection, and also how the joint probability density function (JPDF) of connection between nodes are generated. Most of the network assessments performed in this work are done using SNAP, in which several specific functions were added to the framework during the development of the activities.

2.3 Multi-band systems

Due to the continuous increasing in capacity demanded from optical networks, several approaches aiming this capacity expansion have been proposed (as described in Section 1.2), combining research efforts from both academia and industry. In this work, we focus in MBT solutions, which have being investigated for several years [107–110] and that presents several opportunities and challenges. The main goal of MBT consists in expand the spectral usage of fiber transmission [55], which from the last two decades are based in C-band systems covering a range of 35 nm [37], as presented in Figure 2.9. During the last years, solutions emerged covering a wider spectral range, combining transmission in C- and L-bands [56, 111], with potential to cover a range of 95 nm. This spectral scenario is also commercially available

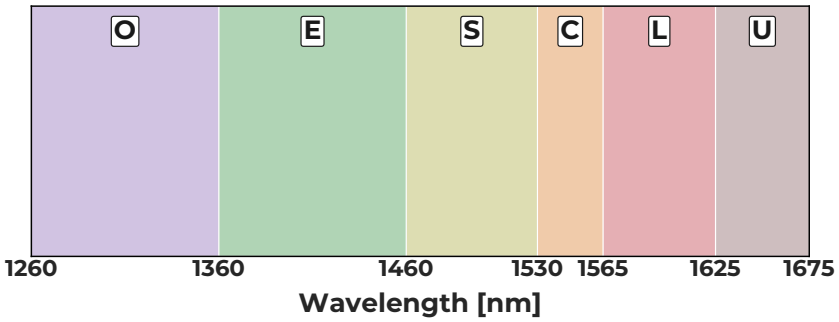

Fig. 2.9 ITU-T spectral bands definition, from O- to U-band.

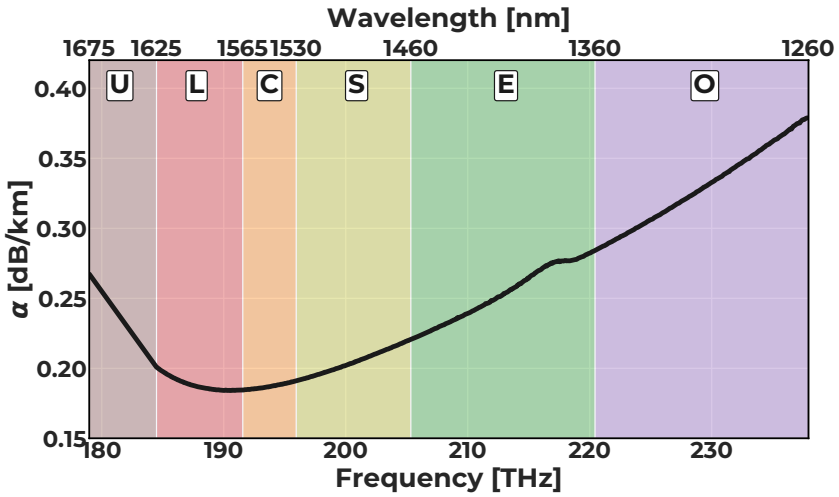

Fig. 2.10 Loss profile of SSMF from U- to O-bands.

and has been deployed in recent years [112]. As shown in Figure 2.10, the entire low-loss (bellow 0.4 dB/km) spectral range of SSMF goes from U- to O-band and provides more than 50 THz in total, presenting a huge potential of capacity without the requirement of new fiber deployment [113, 114].

The first challenge of MBT systems is regarding the modelling of such systems, which requires a proper fiber parameters characterization for the entire used spectrum. The parameters are attenuation profile (α), chromatic dispersion (D), and nonlinear coefficient (γ), shown in Figures 2.10, 2.11, and 2.12, respectively, from U- to O-bands. Moreover, the propagation modelling demands the consideration of the SRS effect, which, as already mentioned in Section 2.1.2, is the dominant effect in MBT. On top of that, the Raman gain must be properly scaled in frequency, as described in [115, 3], in order to model MBT in a accurate way. A detailed analysis on how

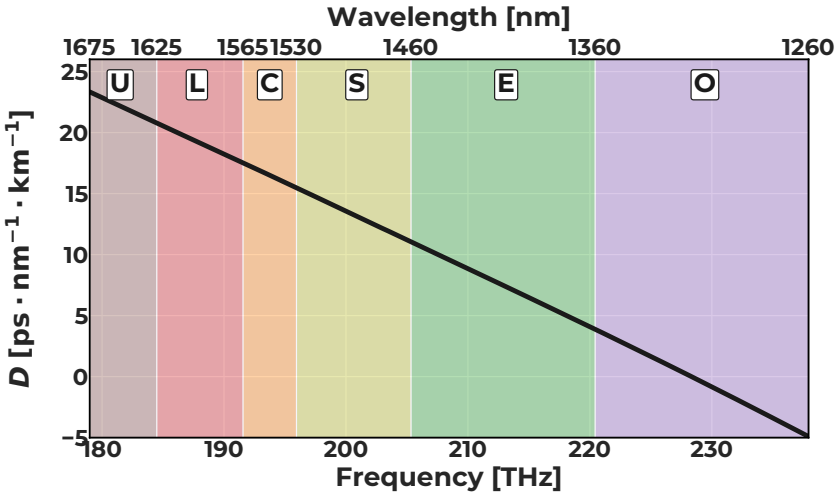

Fig. 2.11 Dispersion profile of SSMF from U- to O-bands.

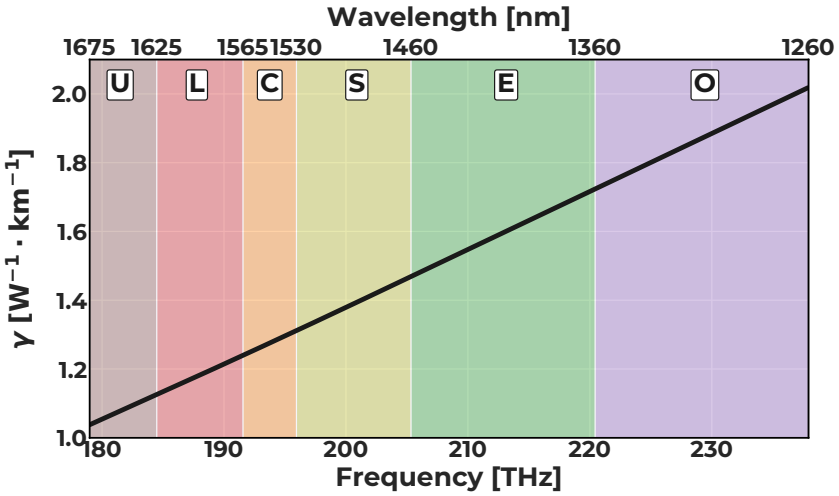

Fig. 2.12 Nonlinear coefficient profile of SSMF from U- to O-bands.

the SRS effect impact the QoT is presented in Section 3.1. Finally, the last aspect regarding modelling in MBT scenarios is the requirement of the SRS effect inclusion in NLI computation. Because of that, for all the simulations performed in this work we made use of the GGN model [81], in which has being shown a very accurate NLI estimation, even for wide spectrum scenarios [3].

The next challenge of MBT systems are the availability of components, which allow the network to operate in other spectral bans. Starting by transceivers, two approaches can be applied. The first option is the design of specific transceivers for each band (or at least a frequency range within a band), which will require the

development of components such as tunable lasers, dual-polarization IQ modulator and coherent receiver front end [116]. This approach is still far from be commercially available, so in recent years a second option emerged as possible short/mid-term solution. The second possible solution is the usage of C-band transceivers in other spectral bands, in which several works tackle this solution [117–119], evaluating the additional penalties when these devices are used outside the designed spectral range. The latter solution presented promissory results, with further investigations being required. The next element is the wavelength-selective switch (WSS), main component required for the ROADM design. While C+L WSS are already commercially available [120], studies on wider devices are being carried out [121], in order to allow wider and completely flexible multi-band network nodes. Finally, we describe the possible solutions for MBT amplifiers. Although the EDFAs present a highly reliable and efficient amplification technology due to development and refinement over the years, their operational spectrum range is limited to C- and L-bands. Recent EDFA technology can achieve up to 6 THz of spectral range [122] for both bands. Nonetheless, this type of amplification is not suitable for other spectral regions. Several other types of doped amplifiers, each one tailored for a specific spectral range have been investigated during the recent years [123, 124]. Among many possibilities, we highlight the thulium doped fiber amplifier (TDFA) [125] targeting the S-band, the neodymium doped fiber amplifier (NDFA) for E-band [126], and finally the bismuth doped fiber amplifier (BDFA), which can cover a wide spectral range, from O- to S- and also from L- to U-bands [127, 128]. As shown in Equation 2.9, the proper characterization of gain and NF of these devices should be carefully take into consideration, in order to proper model a MBT system. In Figure 2.13, we illustrate how an OLS can be upgraded from a C-band to a MBT system, in this particularly case a C+L+S spectral scenario. We also need to add that the additional penalties, shown in Figure 2.13, for band separation required for specific amplification, also need to be considered. Putting together all these considerations specific for MBT scenarios (fiber transmission impairments and devices characteristics), we carry several analysis in the next chapters, evaluation the MBT performance an impact at both OLS and network levels.

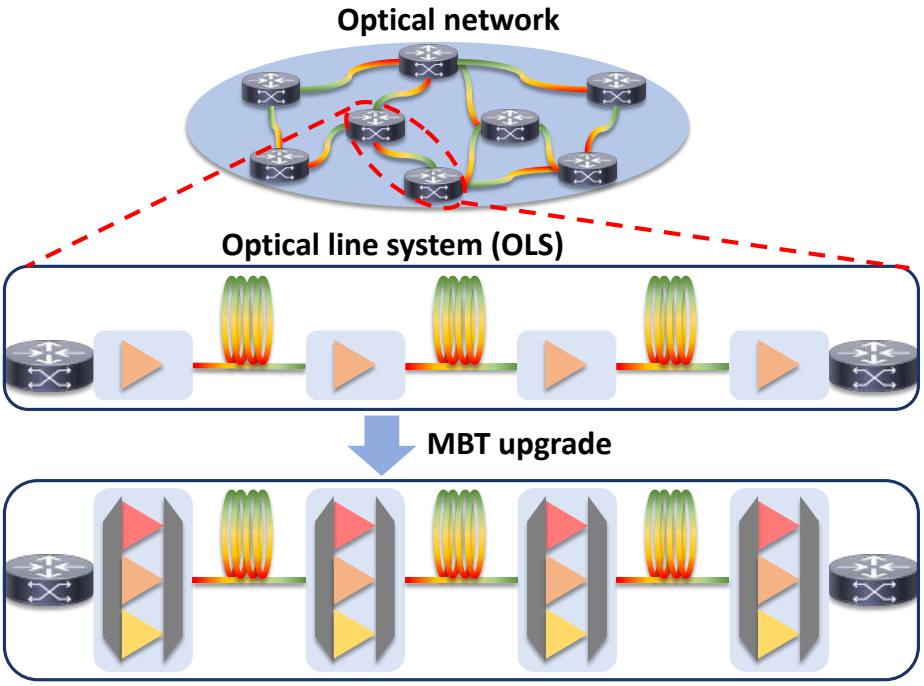

Fig. 2.13 Example of an OLS upgrade, from a C-band to a C+L+S system.

Chapter 3

Launch power optimization for multi-band systems

In the past, a straightforward method to achieve optimal QoT in OLS involved conducting a simple input power sweep. This technique aimed to determine the best WDM input power profile that would maximize system performance. However, with the adoption of multi-band systems, starting with the C+L-bands, the complexity of the interactions between channels and the unique characteristics of devices used in each band increased significantly. As a result, the previously used input power optimization methods, such as the local-optimization global-optimization (LOGO) based on the GN-model proposed in [129], became inadequate, especially when dealing with scenarios that extended beyond C+L systems.

To address these challenges and develop more effective power control strategies, extensive research has been conducted [130–132]. First in this chapter, we aim to explore the impact on QoT when considering a single band approach without proper power tilt compensation for SRS, expanding on the analysis presented in [14]. By examining the consequences of neglecting power tilt compensation for SRS in a single band scenario, we can understand the limitations and potential degradation in system performance. Moreover, our research findings, which have been published in [1, 7], shed light on the analysis carried out in a multi-band C+L+S scenario. We investigated the application of a power offset/tilt strategy in this scenario, recognizing the need for effective power control across multiple bands. The strategy involves strategically adjusting the power levels to compensate for the spectral tilt induced by

SRS, which can significantly impact QoT. Additionally, we incorporated an evolutionary algorithm based on GA into this strategy, aiming to reduce computational effort while providing slightly improved solutions. The application of GA, presented in [9], allows for a more efficient exploration of the power parameter space, enabling the discovery of optimal or near-optimal power offset/tilt configurations.

In summary, this chapter expands on previous research by examining the impact of neglecting power tilt compensation for SRS in a single band approach and extends the analysis to a more complex multi-band C+L+S scenario. By applying a power offset/tilt strategy and incorporating a GA-based approach, we aim to enhance the QoT of optical communication systems and enable efficient utilization of the available spectral resources. Finally, we would like to highlight that the work presented in Section 3.2 and 3.3 were made together with the Infinera team, part of the WON project.

3.1 Launch power control an its impact on OLS QoT

The transmission of optical signals in glass is influenced by a nonlinear phenomenon called SRS, which induces a power exchange from higher to lower frequencies. This phenomenon causes a reduction in power at higher frequencies, resulting in increased attenuation, while lower frequencies undergo power amplification, leading to a decrease in the inherent fiber loss [132]. When considering SRS in conjunction with other factors like ASE noise and NLI generation, it becomes evident that ASE noise affects higher frequencies more significantly due to their greater attenuation caused by SRS. As a result, higher amplification is necessary to compensate for this power loss. Conversely, NLI has less impact on higher frequencies as the power exchange caused by SRS mitigates its generation. On the contrary, lower frequencies demonstrate an opposite trend.

SRS exhibits maximum efficiency at around 13 THz spectral spacing. Although it has a visible impact on C-band transmission, causing a spectral tilt that can be compensated by using devices like gain flattening filter (GFF), its significance remains relatively weak. However, in MBT systems spanning a wider spectral range, such as C+L-band or C+L+S-band line systems, SRS becomes the dominant factor in power control. Figure 3.1 illustrates this behavior by presenting the input (0.0 dBm) and output power profiles (with and without considering the SRS effect) after transmit-

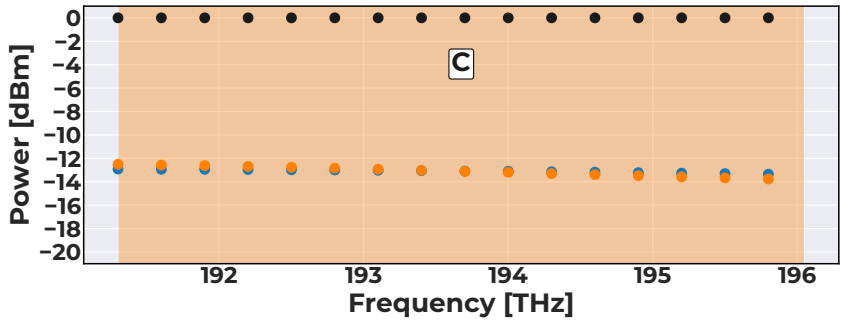

(a)

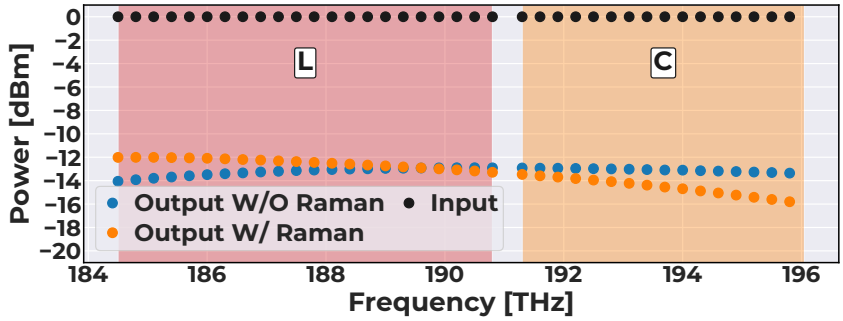

(b)

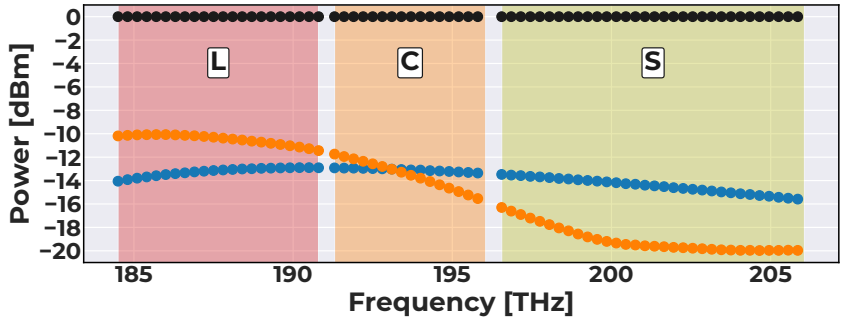

(c)

Fig. 3.1 Input (black circles) and output power profile with (orange circles) and without (blue circles) considering the SRS effect after transmission over a 75 km long SSMF for (a) C-band, (b) C+L and, (c) C+L+S.

ting over 75 km of SSMF for C-band, C+L, and C+L+S scenarios. For the C-band transmission only (Figure 3.1a), the negligible impact of the SRS effect is evident, with a maximum output power difference of approximately 0.4 dBm between considering (orange) and not considering (blue) SRS. Expanding the spectral width to C+L transmission (Figure 3.1b), the more pronounced power transfer from higher to lower frequency channels becomes noticeable, resulting in a maximum difference of approximately 2.6 dBm. Lastly, in Figure 3.1c, the C+L+S scenario demonstrates an

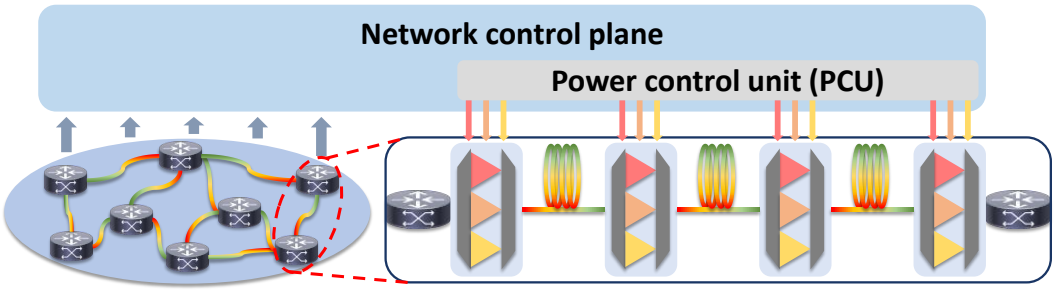

Fig. 3.2 Illustration of a the application of a PCU to control multiple multi-band amplifiers in a OLS.

even more significant effect, with the maximum output power difference reaching approximately 5.2 dBm. These findings emphasize the necessity of implementing appropriate power control techniques in OLS, that take into account the SRS effect in MBT systems to maintain optimal performance, or, at least, minimize the degradation raised in such systems.

The control plane of MBT OLSs encompasses the power control unit (PCU) as a vital component. Its primary objective is to enhance performance and maximize the GSNR for every wavelength in a WDM system. Our proposed MBT optical system incorporates optimized components for each band, particularly the optical amplifiers [133]. In this scenario, the PCU operates simultaneously on all amplifiers within an OLS to optimize transmission. Figure 3.2 visualizes the PCU effectively controlling the operating points of amplifiers for each individual spectral band.

Figure 3.3 showcases the QoT of a single span, where the PCU regulates the gain/output power of the amplifiers to compensate for fiber transmission loss. Furthermore, the input power per band in this scenario is based on [129], with values of 0.9, 0.6, and 1.4 dBm per channel for L-, C-, and S-bands, respectively, for 64 channels, per band, of 75 GHz. The plot presents the OSNR (red triangles), $\mathrm{SNR_{NL}}$ (green squares), and GSNR (blue circles) for different transmission scenarios: single-band transmission (solid lines), C+L transmission (dashed lines), and C+L+S transmission (dotted lines). In the case of single-band transmission, we observed average OSNR values of 32.3, 32.2, and 29.5 dB, $\mathrm{SNR_{NL}}$ values of 34.7, 34.7, and 32.0 dB, and GSNR values of 30.3, 32.2, and 27.5 dB for L-, C-, and S-bands, respectively. The OSNR and $\mathrm{SNR_{NL}}$ demonstrate a proper balance for all bands, thanks to the LOGO approach. Moving on to the C+L transmission scenario, we observed a change in behavior between the linear and nonlinear regimes of the

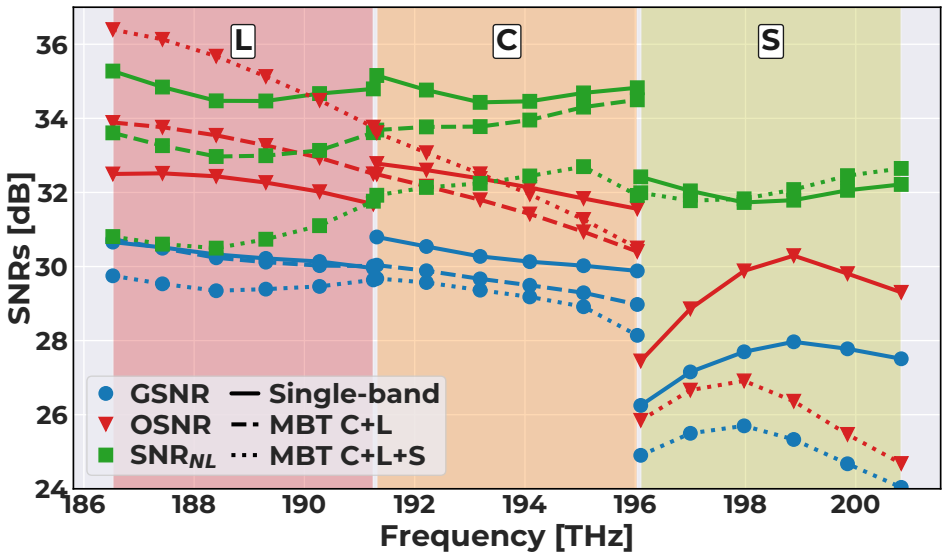

Fig. 3.3 Single-span OSNR (red triangles), SNR_{NL} (green squares), and GSNR (blue circles) for three spectral scenarios: single-band transmission (solid lines), C+L transmission (dashed lines), and C+L+S (dotted lines).

bands. The C-band exhibited an increase in SNR_{NL} and a decrease in OSNR, while the L-band showed the opposite effect. Furthermore, the GSNR decreased for the C-band but remained relatively constant for the L-band, with values of 30.2 and 29.6 dB, respectively. Finally, with the wider transmission spectrum in the C+L+S scenario, we observed degradation in all bands, with the S-band experiencing the highest QoT degradation. The average GSNR values for this scenario were 29.5, 29.2, and 25.1 dB for L-, C-, and S-bands, respectively. Notably, the L-band entered a highly nonlinear regime due to the significant power transfer induced by SRS. Despite the PCU controlling the gain/output power of the amplifiers to maintain consistent power levels, the degradation in MBT QoT requires proper power compensation for the SRS effect.

Figure 3.3 provides insights into how the single-span QoT is affected in a MBT system. In order to evaluate on how this performance degradation is translated to OLS capacity, in Figure 3.4 it is presented the OLS total capacity per band versus the total number of OLS spans for the same previous scenarios tested. The OLS capacity was computed for each channel, within each band, based on the GSNR and the possible bit rate accordingly to the transceiver ZR+ specification provide in Table B.1, presenting three modulation formats and four possible bit rates (100 to 400 Gbps). Starting with the L-band, it is clear that the OLS capacity almost does

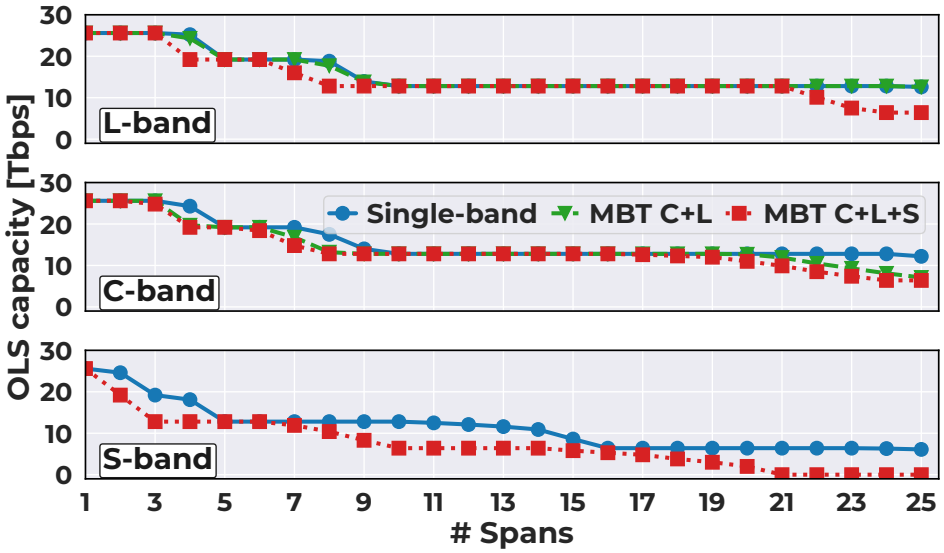

Fig. 3.4 OLS capacity versus number of spans per band for three spectral scenarios: single-band transmission (blue circles/solid line), C+L transmission (green triangles/dashed line), and C+L+S (red squares/dotted lines).

not change between the single-band and C+L transmissions, achieving a maximum decrease of 1.1 Tbps for a OLS composed of 8 spans. Furthermore, this maximum capacity decreasing achieves 6.4 Tbps for 24 spans. Going further, for the C-band results the impact of MBT systems starts to appear already when C+L systems are used. The maximum decrease in this band for C+L systems achieved is 5.1 Tbps, while this maximum difference increase to 6.4 Tbps using C+L+S scenario. Unlike the L- and C-bands, in which the impact of MBT in single span not always results in decrease in OLS capacity, the S-band presents a decrease in overall capacity for almost every OLS number of spans. The maximum difference in capacity comparing single-band transmission with C+L+S system is 6.4 Tbps, with only three OLS lengths presenting the same capacity (1, 5, and 6 spans). Both plots (Figures 3.3 and 3.4) highlight that the input power per channel need to be proper defined based on the multi-band system, even with the PCU being able to control the amplifiers in order to compensate only for the amount of loss during transmission. Moreover, this difference, even if it is small for single OLS, can increase significantly specially in regional and backbone networks, as they are composed by several OLSs, with high average number of spans per LPs.

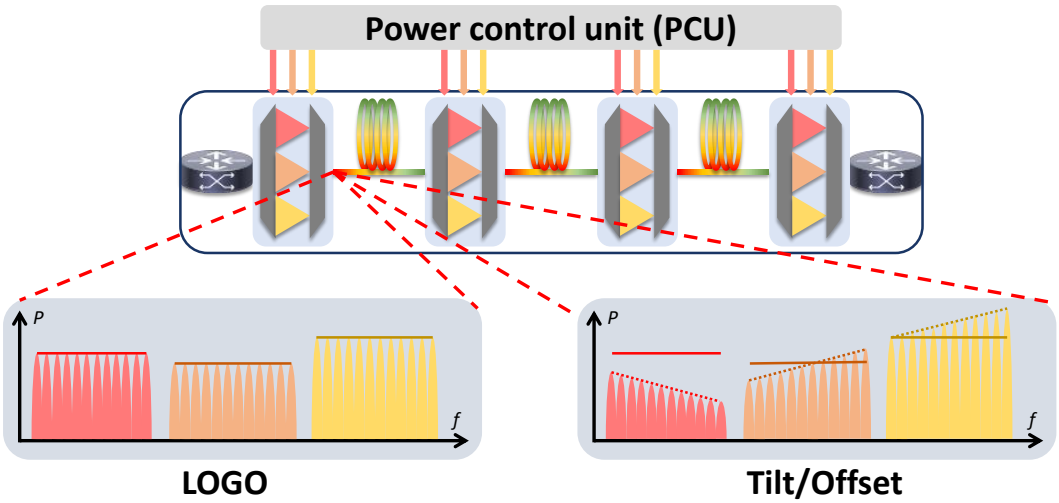

Fig. 3.5 Illustration of only LOGO (left) and tilt/offset (right) strategies for C+L+S-band transmission scenario.

3.2 Multi-band power control strategy

In this section, we present the findings from our study [1]. To optimize power in a disaggregated approach, we adopt a span-by-span strategy [134, 135], using the LOGO algorithm as a starting point. This algorithm aims to maximize the QoT under the assumption of full link spectral loading [129]. In Figure 3.5, the left spectrum illustration depicts this approach, with the power levels per channel represented by solid lines. In our work, we follow a similar approach, operating on the two parameters typically adjustable in commercial amplifiers: the average gain/output power and the associated tilt. The objective of an optimized PCU is to determine the optimal average output power and tilt per band simultaneously. This optimization aims to maximize and flatten the per-band GSNR, consequently enhancing the deployable capacity [136]. The optimization process for a single fully loaded span, comprising a fiber and an amplifier, begins by setting a flat launch power at the per-band optimum [135], disregarding frequency variations and SRS. Subsequently, the per-band power offset and tilt are adjusted to achieve the optimal solution. The result of this strategy is depicted in the right spectrum illustration in Figure 3.5, where the final power profile per band is represented by the dotted lines. In this configuration, the L-band channels (red) are launched into the optical fiber with a negative offset (power of the central L-band channel below the LOGO value) and negative tilt (measured in dBm/THz). The C-band channels (orange) are

launched into the optical fiber without power offset and with a positive tilt. Similarly, the S-band channels (yellow) are launched into the fiber with a positive power offset (power of the central S-band channel above the LOGO value) and positive tilt, indicating an increase in power along the S-band channels. To determine the optimal per-band offset and tilt, we performed a brute-force computation, analyzing all combinations and evaluating the GSNR for each scenario using GNPy [95, 57]. While the approach described has previously been investigated for C- and C+L-band scenarios in previous studies [6, 137], we expanded it here to include the S-band. The results of the optimization serve as a hypothesis for operational settings in the network control plane, allowing for the abstraction of the network topology for physical-layer-aware networking analysis [138]. This network abstraction is then utilized for assessing network performance, enabling an examination of the impact of multi-band provisioning with optimized power control on overall networking performance. Additionally, the power optimization procedure is applied to the C-only scenario to facilitate networking analyses in the context of SDM applications, which serve as a benchmark for the BDM approach.

3.2.1 Transmission analysis

In our study, we assume that all fiber spans in the amplified lines have identical lengths of 75 km and are composed of ITU-T G.652D SSMF fiber type. To recover the full loss in the system, we employ lumped amplification. For channels in the C- and L-bands, we utilize commercially available EDFAs as amplifiers. In the S-band, we employ a TDFAs benchtop amplifier. The characteristics of these amplifiers are reported in [125]. Since there are no commercially available amplifiers for the S-band, we rely on the NF values obtained from the aforementioned benchtop amplifier. Fig. 3.6 illustrates the NF of the amplifiers, showing an average value of approximately 6.5 dB for the S-band amplifier. For the C- and L-band amplifiers, the average NF is approximately 4.2 dB and 4.7 dB, respectively, as depicted in Fig. 3.6. The noise figure profile of the TDFA exhibits significantly lower performance compared to the commercially available EDFAs. We assume a constant NF profile for the amplifiers, irrespective of their power, tilt, or spectral configuration. Our analysis, which is closely related to the fixed NF profiles used, aims to demonstrate that it is possible to achieve acceptable performance in terms of QoT and delivered traffic with the current development stage of these amplifiers. Each band operates on the

ITU-T 50 GHz WDM grid, with transceivers set at a symbol rate of 32 GBaud. The guard bands between adjacent bands have a minimum width of 500 GHz. For the C- and L-bands, we utilize 96 channels each. In the S-band, we consider two different channel arrangements: 96 channels adjacent to the C-band, respecting the guard band distance, and the utilization of the entire S-band, corresponding to 192 channels. Initially, the launch power per channel is set to -2.1 dBm for the C-band, -1.99 dBm for the L-band, and -2.0 dBm for the S-band.

To determine parameters in a multi-band power control scenario, a brute force (BF) approach was employed, considering a range of pre-tilts and offsets specific to each band. For the C and C+L scenarios, the pre-tilt range varies from -0.5 to 0.5 dBm/THz, with a step size of 0.1 dBm/THz. The offsets range from -1.0 to 2.0 dB and -2.0 to 1.0 dB for the C-band and L-band scenarios, respectively. The step size for both offsets is 1.0 dB. This results in 44 combinations for the C-band and nearly 2000 combinations for the C+L band case. Different parameter sets were utilized for the scenarios involving the S-band to avoid an excessive number of combinations. For the C- and L-bands, the pre-tilt ranges from -0.5 to 0.5 dBm/THz with a step size of 0.2 dBm/THz. The tilt value remains flat, and the offset varies from -1.0 to 1.0 dB. For the S-band, the pre-tilt ranges from 0.0 to 3.0 dB for both cases (with 96 and 192 channels in the S-band), with a step size of 1.0 dB. This results in approximately 12000 combinations for each scenario. To expedite the algorithm, the NLI contribution is computed for 5 channels within each band containing 96 channels, and for 10 channels in the S-band case with 192 channels. The computation is performed for the central channel of the spectral band, with a frequency distance of approximately 1 THz used for the remaining computed

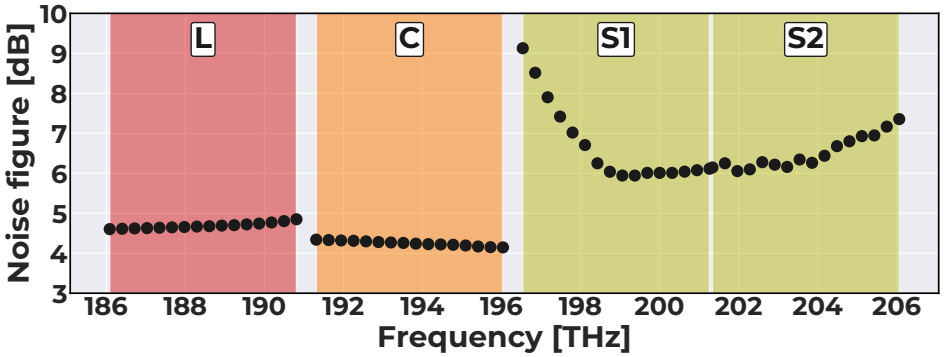

Fig. 3.6 Amplifier noise figures for all spectral bands used in BDM analysis.

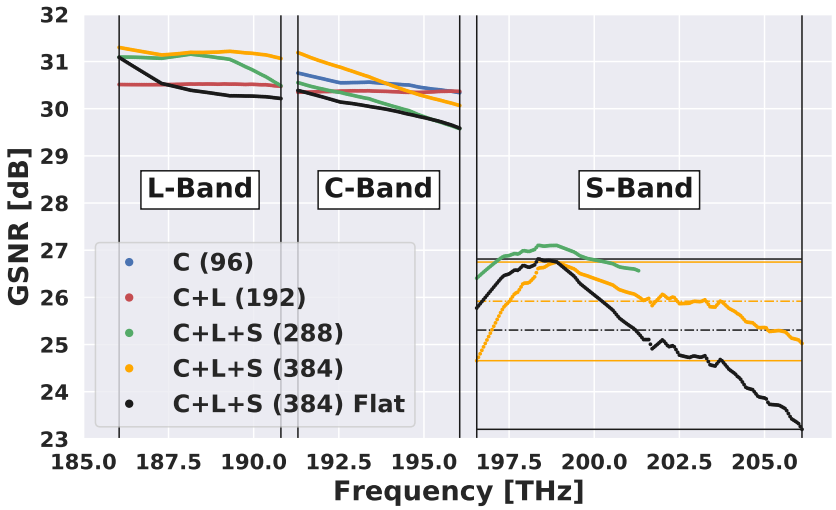

Fig. 3.7 75 km fiber span GSNR versus frequency for all analyzed scenarios, maximum and minimum GSNR for the S-band (lines) and average GSNR (dashed lines) for the S-band, comparing launch power control with flat input powers.

channels. For the remaining channels, their GSNR values are interpolated from those that have already been computed, following the same procedure outlined in [137].

Figure 3.7 displays the optimized per-span GSNR profiles for the four multi-band scenarios considered in this study: (1) the reference scenario, C-band only, with 96 channels, (2) the C+L-band scenario with 192 channels, and the C+L+S-band scenarios with (3) 288 and (4) 384 channels. For each scenario, the tilt and offset values corresponding to the optimized solutions are listed in Table 3.1. These values were obtained using the BF optimization method described earlier. In the case of deploying only the C-band (blue curves), the average per-span GSNR for the

Table 3.1 Optimum launch power tilts and offsets per band for the C-, C+L- and both C+L+S-band transmission cases.

Bands (N^o of channels)	**Pre-tilts [dBm/THz]**			**Offsets [dB]**		
	L	**C**	**S**	**L**	**C**	**S**
C (96)	-	-0.5	-	-	0.0	-
C+L (192)	0.3	0.4	-	-2.0	-1.0	-
C+L+S (288)	-0.5	0.5	0.1	-1.0	-1.0	2.0
C+L+S (384)	-0.5	0.5	0.5	-1.0	-1.0	0.0

96-channel WDM comb is 30.5 dB. By activating the L-band with an additional 96 channels (red curves) using a multi-band power controller, the per-span average GSNR is 30.3 dB for the C-band and 30.5 dB for the L-band. Consequently, the C+L-band BDM incurs a penalty of only 0.2 dB compared to doubling the C-band transmission capacity. Despite this decrease, the launch power strategy maintains an almost flat GSNR profile for both bands. When an additional 96 channels are activated in the S-band, creating a C+L+S-band BDM line system of 288 WDM channels (green curves), the optimal multi-band power control guarantees an average per-span GSNR of 30.1 dB, 31.0 dB, and 26.8 dB for the C-, L-, and S-bands, respectively. Within the C+L+S-band BDM implementation, the C-band experiences an additional but limited average per-span GSNR penalty of 0.2 dB compared to the C+L-band case. On the other hand, the L-band benefits from SRS pumping into the lowest spectrally located channels, slightly improving its QoT. The S-band's 96 channels exhibit a poorer GSNR due to SRS and the higher NF of the S-band amplifier. However, the overall penalty in the S-band is limited to 4 dB, enabling a reasonable transmission capacity while minimally affecting the C+L-band performance. Although the per-band GSNR flatness is worse compared to the C+L-band case, the difference between the maximum and minimum per-band GSNR is confined within 1.0 dB. Finally, when the entire S-band is activated with 192 channels (orange curves) in a C+L+S-band WDM multi-band line system, the optimal power control ensures an average per-span GSNR of 30.6 dB, 31.2 dB, and 25.9 dB for the C-, L-, and S-bands, respectively. In this case, the spectral availability is equivalent to four C-band only line systems. The transmission capacity of the 192 lower frequency channels exhibits slightly larger QoT than the combined capacity of the two C-band only line systems, thanks to the SRS pumping enabled by the S-band channels. For the additional 192 available channels in the S-band, the average GSNR is approximately 5 dB smaller. Nevertheless, this value still guarantees good transmission capacity with a per-span GSNR of 25.9 dB. Regarding GSNR flatness, this last scenario demonstrates excellent performance with values of approximately 0.1 dB in the L-band and 1.1 dB in the C-band, with most values surpassing the C+L-band case.

We also conducted a comparison between the proposed multi-band power control strategy and the flat spectrum power control, known as the LOGO strategy, applied independently to each band in the C+L+S-band BDM with a total of 384 channels. To highlight the benefits of the proposed multi-band power control strategy over

LOGO, we focused on the S-band. In Fig. 3.7, we added yellow and black horizontal lines specifically for the S-band, representing the minimum, maximum, and average GSNR (shown as dashed lines). It is worth noting that the multi-band power control strategy achieves a gain of 0.6 dB in the average GSNR and improves the flatness by 1.5 dB compared to the LOGO strategy alone.

Shifting our attention to the C- and L-bands, the proposed method increases the average GSNR by 0.6 dB for the C-band and 0.7 dB for the L-band, with the L-band exhibiting almost flat QoT. From a network management perspective, the flatness of GSNR is just as important as maximizing the average value. It enables a larger pool of wavelengths with equivalent performance, simplifying the routing and wavelength assignment (RWA) algorithms and reducing the impact of the wavelength continuity constraint in traffic allocation.

To assess the impact of different upgrades in an OLS using the GSNR profile obtained through power optimization, Fig. 3.8 illustrates the allocated traffic as the number of spans increases. For 10 spans, the C-band only case delivers a capacity of 41.2 Tbps. By employing SDM, the capacity increases to 82.4, 123.6, and 164.8 Tbps for the scenarios with 2, 3, and 4 times more channels, respectively. With the BDM upgrade, and also considering 10 spans, we achieved capacities of 82, 117, and 150 Tbps for the BDM scenarios with 192, 288, and 384 channels, respectively. The allocated traffic is determined based on the Shannon limit, and doubling the channels results in nearly the same limit for both BDM and SDM upgrades. However, for 3 and 4 times more channels, SDM outperforms BDM, with differences of approximately 6% and 9%, respectively. These results demonstrate the degradation in delivered traffic due to the lower QoT profile of the BDM upgrade. They serve as a reference to evaluate if the impact on a network scenario follows a similar behavior.

3.2.2 Network assessment

To assess the impact of various physical layer optical transport solutions on overall network performance, we utilized the SNAP framework [99]. SNAP operates on the physical layer abstraction of the network and evaluates the GSNR degradation introduced by each network element [138]. It statistically tests the network's progressive load using different traffic models. LPs are allocated based on the defined

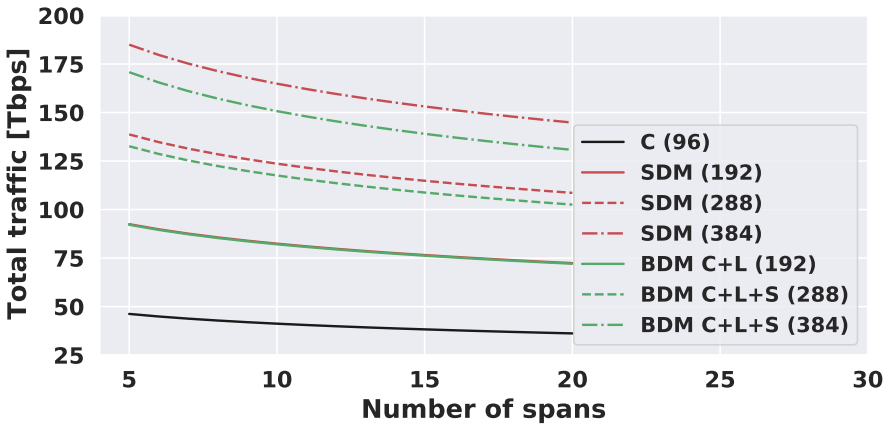

Fig. 3.8 Total allocated traffic vs. number of fiber spans for all upgrade scenarios.

RWA algorithm and transceiver characteristics, and networking metrics are obtained through Monte Carlo analyses. In this study, we assume the presence of ideal flexible transceivers that can adapt the bit-rate continuously based on the available LP GSNR. This allows us to explore the fundamental limitations and determine the capacity limits of the BDM upgrade. The SNAP framework supports two types of traffic models, leading to different types of analyses. The first is the given-traffic analysis, where all traffic (in terms of the number of lightpaths or bit-rate) between all nodes in the network is known in advance. The second is the progressive traffic analysis, where the model generates requests progressively until reaching a predefined stop criterion, such as the total number of requests or the total number of blocked requests. The progressive traffic analysis stresses the network and provides both static and progressive metrics, representing the loading evolution of the network. For progressive traffic analysis, SNAP can handle different types of traffic distributions by modifying the JPDF, which determines the frequency of requests between each pair of nodes in the network. SNAP produces outputs such as the bit-rate of each allocated LP, average bit-rate per lightpath, spectral occupation details, and the number of blocked requests by nodes or links, among other metrics. In this study, we compare different scenarios based on the BP versus the overall allocated traffic. Additionally, we focus on congestion in ROADM-to-ROADM connections, considering a target BP of 10^{-2}.

Three network topologies are considered to statistically assess the network performance: (1) German (DT) network shown in Fig. A.1a, (2) US-NET topology shown in Fig. A.1b, and (3) European (COST) network shown in Fig. A.1c. All network topologies parameters and metrics, as number of nodes, number of links,

among other, are described in details in Chapter A. To obtain stable networking metrics using the SNAP framework, we set the number of iterations as $N_{\mathrm{MC}} = 30000$ for the Monte Carlo algorithm in the German topology and $N_{\mathrm{MC}} = 20000$ for the US-NET and COST topologies. The latter topologies are larger networks, requiring a reduction in the number of iterations to minimize computational effort. For routing, we employed a k-shortest path algorithm with $k = 15$, and the first-fit (FF) algorithm was applied for WA in progressive traffic analysis to obtain both dynamic and static metrics [99]. Specifically, in the SDM case, the WA attempts to allocate lightpaths in all channels of the first fiber set (e.g., C-band 1) before moving on to the second set, following the FF strategy. Lightpath requests are generated progressively for each Monte Carlo run, considering two scenarios with statistical traffic models characterized by JDPFs. The first scenario uses a uniform JPDF, where the probability of connection is the same for any source-destination pair. The second scenario employs a nonuniform JPDF based on population [137]. In the nonuniform JPDF, requests between optical nodes in cities with higher populations have a higher probability of occurrence compared to nodes in less populated cities.

The probabilities $P(s,d)$ of selecting a source-destination node pair in the uniform and nonuniform JDPFs are formally given by:

$$P(s,d) = \frac{1}{N(N-1)} \tag{3.1}$$

$$P(s,d) = \frac{pop_s \cdot pop_d}{\sum\limits_{(i,j)\in A} pop_i \cdot pop_j} \tag{3.2}$$

Here, N represents the total number of nodes in the network topology, pop_x corresponds to the population of the city geographically associated with node x, and $(i,j) \in A$ denotes all possible source-destination node pairs (i,j) in the network topology A. The network performance is evaluated based on the multi-band amplifier power control, utilizing the optimal GSNR profile obtained through the previously described brute force approach. The bit-rate allocation over each LP assumes the use of ideal elastic transceivers that adapt the bit-rate according to the available GSNR as prescribed by Shannon's law. Consequently, our focus lies in exploring the fundamental transmission limitations within the considered network topology, without being constrained by a specific transceiver implementation.

The optimized transmission techniques presented in Section 3.2.1 are subsequently utilized to conduct network-level analyses. The GSNR values obtained for each WDM channel are used to construct a weighted topological graph, where the weights correspond to the GSNR degradation [138]. This graph serves as the basis for implementing the SNAP framework. Since the GSNR profiles are derived for fully loaded spans, whereas the network analysis is performed for progressive traffic, we assume the presence of optical noise-loading capability in the network. This means that the ROADMs emulate fully loaded OLSs and can maintain the QoT levels with minimal changes compared to the transmitted modulated signals. For all three network topologies considered, we assume a different BDM solution for WDM transmission, with the C-band only scenario serving as the reference. In each case, SNAP is applied to uniform and nonuniform traffic models for both BDM and SDM, assuming the same spectral availability. In the following analysis, we compare the following scenarios: i) C+L BDM to SDM $2\times$; ii) C+L+S-band (96 channels) BDM to SDM $3\times$; and iii) C+L+S-band (192 channels) BDM to SDM $4\times$. The results are presented as a statistical average over the Monte Carlo runs, displaying the BP versus the progressively allocated total traffic for each BDM and its equivalent SDM scenario, considering both traffic models. To provide a fair comparison between the different transmission solutions, we calculate the enabled traffic multiplication factor based on the reference BP value of $\text{BP} = 10^{-2}$ and the corresponding traffic values. This multiplication factor allows us to compare the performance of the various transmission techniques on an equal basis.

We comment on the networking results starting from the German topology whose results are displayed in Fig. 3.9. Figures 3.9a and 3.9b illustrate the BP versus the progressively total allocated traffic for the considered BDM and SDM solutions, considering uniform and nonuniform traffic models, respectively. In Figure 3.9a, for the German topology and uniform traffic model, with $\text{BP} = 10^{-2}$, we observe that the reference C-band only case (black curve) achieves a total allocated traffic of 268 Tbps. By employing the BDM upgrade (green curves), we achieve approximately $568, 867, 1149$ Tbps of total allocated traffic for C+L-band, C+L+S-band (288 channels), and C+L+S-band (384 channels), respectively. The equivalent reference C-band SDM solutions (red curves) based on 2, 3, and 4 fibers exhibit slightly larger total allocated traffic values, specifically $570, 879, 1187$ Tbps, respectively. A similar trend is observed in Figure 3.9b for the nonuniform traffic model. In general, this network topology appears to be well-designed for a traffic model proportional to

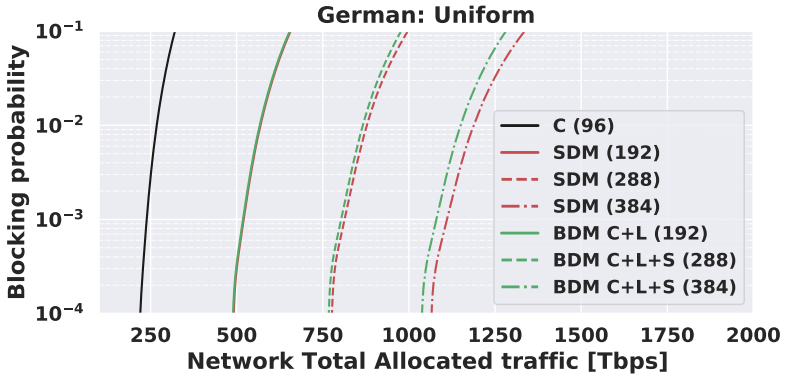

(a)

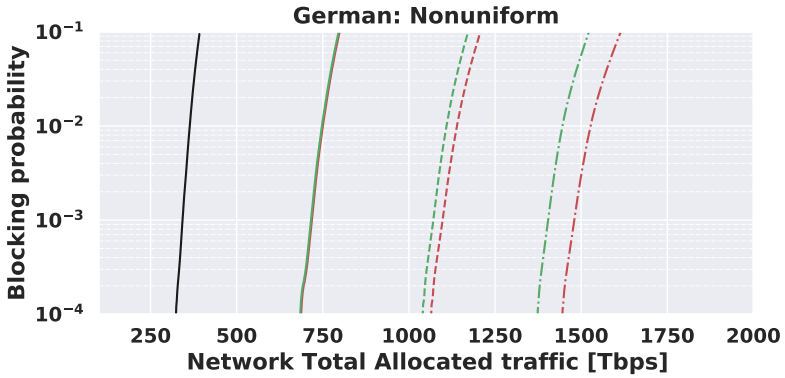

(b)

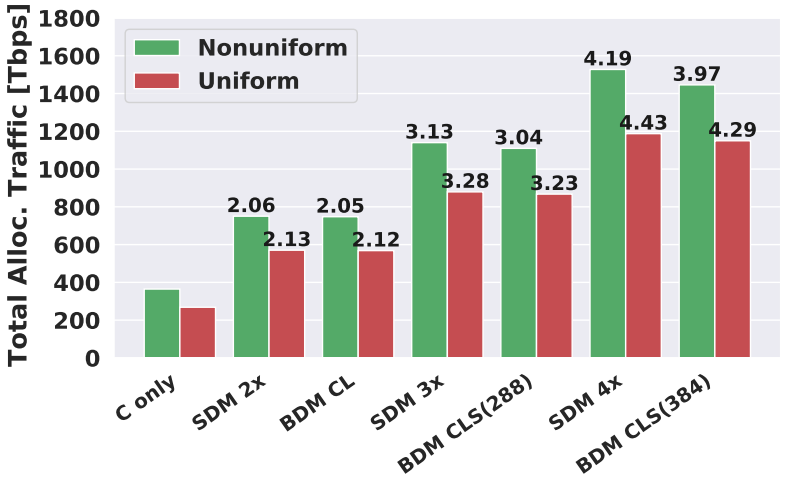

(c)

Fig. 3.9 Network performance results for German topology: Total allocated traffic versus BP with (a) Uniform and (b) Nonuniform JDPFs, and (c) total allocated traffic multiplicative factor for BP $= 10^{-2}$.

the population in the urban areas where each ROADM node is located. With the nonuniform traffic model, the total allocated traffic is consistently higher compared to the uniform case. The largest difference in allocated traffic is observed when comparing the SDM solution with 4 fibers (1527 Tbps) to C+L+S (384 channels) BDM (1445 Tbps). All results for the German topology are summarized in Figure 3.9c for comparison. The green bars represent the nonuniform traffic model, while the red bars represent the uniform traffic model. In addition to the traffic values, the allocated traffic multiplication factors are displayed, considering the C-only scenario as the reference. It can be observed that the nonuniform traffic consistently exceeds the uniform traffic for both BDM and SDM solutions with a relatively constant proportionality. Only in the case of nonuniform traffic, the BDM solution with a cardinality of 4 achieves a multiplication factor of only 3.97. As previously mentioned, this behavior is enabled by a topology that is well-suited for this traffic model. When analyzing the BDM/SDM upgrade, it is evident that both solutions enable a traffic multiplication factor that exceeds the BDM/SDM cardinality. Comparing the BDM and SDM solutions, it is observed that the reference SDM consistently outperforms BDM by less than 3%, reaffirming that MBT can be a viable approach to expand network traffic capacity without relying on new fiber structures or unused dark fibers.

Figure 3.10 illustrates the results for the US-NET topology. In the case of the C-band, the total allocated traffic for BP $= 10^{-2}$ with a uniform JPDF traffic model is 410 Tbps, as shown in Figure 3.10a. For the same JPDF and BP, the BDM upgrade provides total allocated traffic of approximately $835, 1244, 1630$ Tbps for the C+L-band, C+L+S-band (288), and C+L+S-band (384) cases, respectively. On the other hand, the SDM upgrade allocates more traffic in all considered scenarios, achieving approximately $839, 1267, 1700$ Tbps for C-band upgrades with 2, 3, and 4 fibers, respectively. In contrast to the German topology, the nonuniform traffic model based on the population applied to the US-NET delivers less total traffic than the uniform case, as presented in Figure 3.10b. This can be attributed to the characteristics of the topology, where the most populated cities, where the ROADMs are located, are situated at the extremes of the network topology (East and West coasts). These cities demand ultra-long connections with higher frequency, resulting in lower total traffic compared to the uniform traffic distribution. At BP $= 10^{-2}$, the maximum capacity upgrade using BDM with 4 fibers reaches 1405 Tbps, while the SDM upgrade using 384 channels achieves 1352 Tbps. The multiplicative factor reported in Figure 3.10c

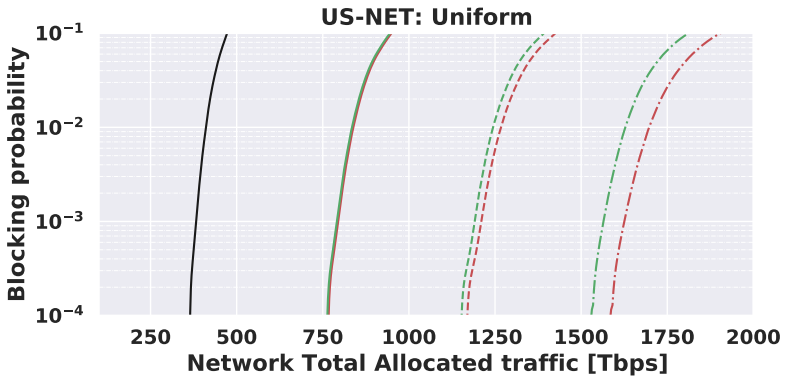

(a)

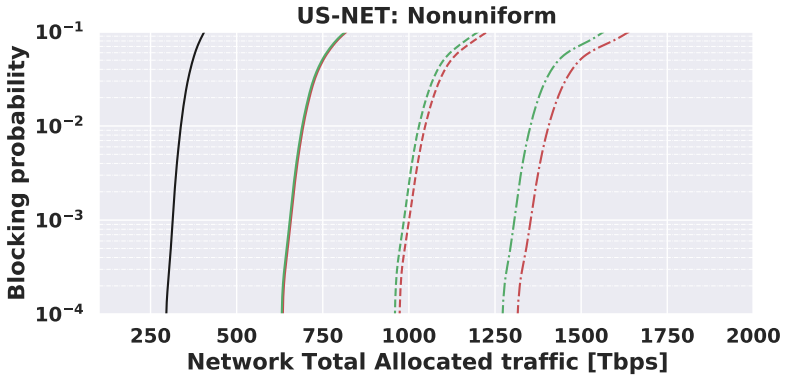

(b)

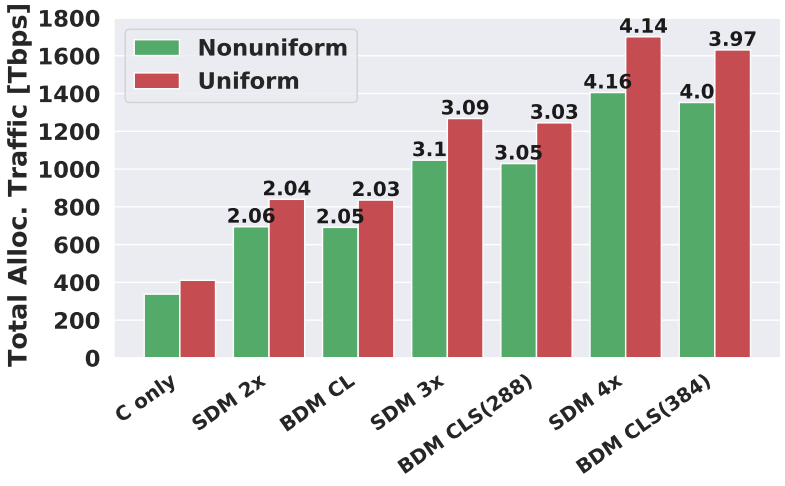

(c)

Fig. 3.10 Network performance results for USNET topology: Total allocated traffic versus BP with (a) Uniform and (b) Nonuniform JDPFs, and (c) total allocated traffic multiplicative factor for BP $= 10^{-2}$.

highlights that both upgrade scenarios using BDM more than double, triple, and quadruple the capacity for the two considered traffic models. The highest difference in allocated traffic, approximately $\sim 3.8\%$, is observed when comparing BDM with SDM.

Finally, we present the results for the COST topology shown in Fig. 3.11. Figure 3.11a displays the results of allocated traffic for a uniform JPDF with $\mathrm{BP} = 10^{-2}$. The BDM upgrade achieves approximately $260, 543, 816, 1072$ Tbps for C-only, C+L-band, C+L+S-band (288), and C+L+S-band (384), respectively. The SDM solutions with 2, 3, and 4 fibers provide allocated traffic of approximately $547, 836, 1131$ Tbps. For the nonuniform JPDF traffic model presented in Figure 3.11b with the same BP, the maximum difference between SDM and BDM is approximately 50 Tbps. The multiplicative factor of this topology for both traffic JDPFs is shown in Figure 3.11c, exhibiting a similar behavior as observed in the previous topologies. Notably, only the BDM C+L+S-band with 384 channels does not exceed the proportional increase of total allocated traffic compared to the reference C-band only case. All three analyzed topologies, with the two traffic models shown in Figures 3.9, 3.10, and 3.11, demonstrate a small increase in the difference of allocated traffic between BDM and the corresponding SDM technique as the cardinality upgrade increases. The results are summarized in Table 3.2, which presents the allocated traffic multiplicative factors for all combinations of topology, upgrade scenario, and traffic JPDF. It is worth noting that the FF spectrum allocation policy used in this work prioritizes channels with lower frequencies, reserving higher frequency channels for more loaded network conditions, which corresponds to lower QoT levels. Table 3.2 also demonstrates that the BDM technique enables an increase in allocated traffic proportional to the cardinality upgrade in almost all cases, indicating its viability as an option for network upgrade scenarios in terms of delivered traffic. Furthermore, the randomness of the traffic distribution can explain why the multiplicative factors can exceed the cardinality upgrade.

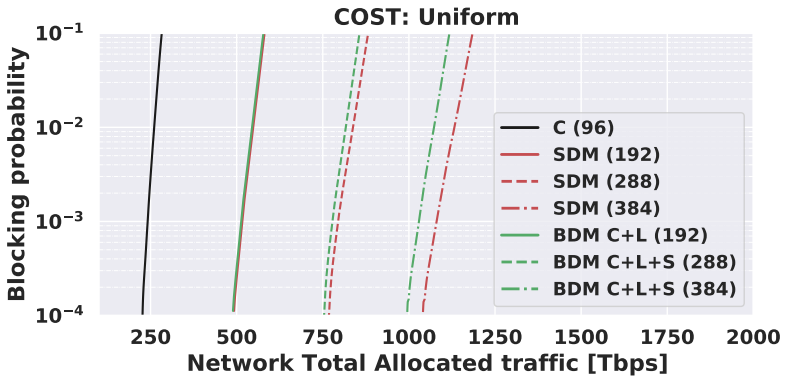

(a)

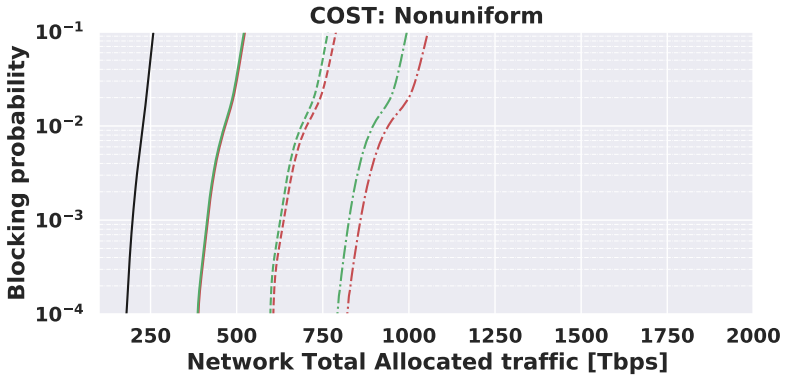

(b)

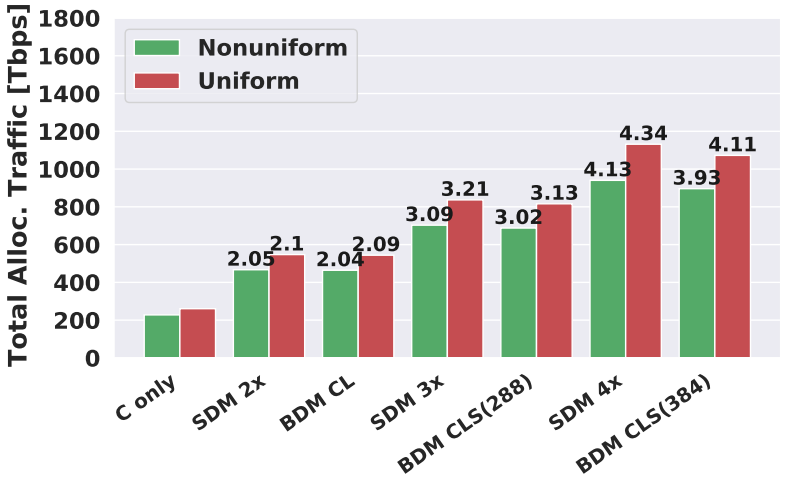

(c)

Fig. 3.11 Network performance results for COST topology: Total allocated traffic versus BP with (a) Uniform and (b) Nonuniform JDPFs, and (c) total allocated traffic multiplicative factor for BP $= 10^{-2}$.

Table 3.2 Allocated traffic multiplicative factors (C-only as reference) of German, US-NET and COST topologies for all upgrade scenarios and traffic distributions with BP $= 10^{-2}$.

Scenarios	German		US-NET		COST	
	Uni.	Nonuni.	Uni.	Nonuni.	Uni.	Nonuni.
SDM 2×	2.13	2.06	2.04	2.06	2.1	2.05
C+L	2.12	2.05	2.03	2.05	2.09	2.04
SDM 3×	3.28	3.13	3.09	3.1	3.21	3.09
C+L+S (288)	3.23	3.04	3.03	3.05	3.13	3.02
SDM 4×	4.43	4.19	4.14	4.16	4.34	4.13
C+L+S (384)	4.29	3.97	3.97	4.0	4.11	3.93

3.3 Evolutionary algorithm applied to tilt/offset strategy

This section explore the application of an evolutionary algorithm to the strategy shown in 3.2 and presented in [9]. In this work, we shown that the usage of a GA can generate slightly better OLS QoT results, considerable decreasing the computational time to obtain these results.

3.3.1 Overview of GA and its application to OLS input power optimization

During the mid-19th century, naturalism emerged as a movement challenging traditional notions of predictability and immutability. It proposed that all matter undergoes constant transformation, influenced by the environment and heredity. Charles Darwin's book, "On the Origin of Species," published in 1859, rejected fixed species and introduced the concept of gradual variations through small and favorable modifications.

Drawing inspiration from naturalism, genetic algorithms were developed by Holland and utilize genetic crossovers, mutations, and selection to optimize solutions [139]. Individuals represent potential solutions encoded in chromosomes, and populations evolve through generations. Crossover involves combining parent chromosomes through single-point, two-point, or uniform methods, among others, mutation introduces random modifications, allowing for exploration of new solutions

and avoidance of local minima, and selection is the process of choosing individuals for the next generation based on specific criteria [140]. Overall, genetic algorithms are inspired by naturalistic principles and provide a framework for solving optimization problems through the use of genetic operations and selection mechanisms.

In order to apply the GA to the OLS input power optimization problem, firstly we define the structure of the individual, which represents a possible solution inside the problem search space. For our case, each individual is composed by $2 \cdot b$ genes, in which b is the number of bands in our MBT scenario, representing the values of tilt and offset per band. We remark that for our particular case, as we use similar span lengths in all network links, these values does not require to be expanded for all OLS MBT amplifiers. Moreover, if different span lengths should be considered, the individual will be composed by $s \cdot 2 \cdot b$, in which s would represent the number of amplifiers within the OLS. Secondly, we define two metrics to evaluate each individual within the GA population: (1) maximize GSNR average, and (2) minimize the average ΔGSNR per band, which represents the GSNR flatness, also per band. As this problem presents two objective functions (GSNR average and flatness), we made use of the crossover, mutation and selection of [141] which proposes a multi-objective GA. Regarding selection, at the end of each iteration the algorithm produces Pareto-front, which will contain the non-dominated individuals of each iteration and where each individual can not improve an objective function without worsening the other [140].

3.3.2 Scenario description and results

To evaluate the performance of the multi-objective GA applied to our problem, we compare it with the BF approach described in Section 3.2. The BF optimization is performed for the C- and L-band, with pre-tilt and offset values set to [0.5 dBm/THz, -1.0 dB] for the C-band and [-0.5 dBm/THz, -1.0 dB] for the L-band. Next, the S-band is virtually divided into four independent sub-bands, each consisting of 48 channels, and different combinations of power settings are explored. Specifically, for each sub-band, the pre-tilt range considered varies from -0.5 to 0.5 dBm/THz (with a step of 0.5 dBm/THz), and the offset range considered varies from 0.0 to 2.0 dB (with a step of 1.0 dB). This results in a total of 6560 combinations that need to be evaluated. In contrast, the GA-based algorithm performs a total of 60 iterations with a population size of 60 individuals, resulting in a total of 3660 evaluations.

Here is important to notice that the population size was tunned after trying values varying from 10 to 80 with increment steps of 10. By the tries, the best results were provided by the population size of 60, 70 and 80, with no significant difference between them. As the structure of the individual (chromosomes) can be any real value between the ranges defined for tilt and offset of each band, we selected the simulated binary crossover and polynomial mutation as crossover and mutation, respectively, operators [141]. Both crossover and mutation operators present a constant to be set called distribution index (η), which is responsible to maintain the generated offspring close (high value of η) or far (low value of η) from their parents. For both operators, we used $\eta = 20$. For this particular parameter, setting $\eta = 20$ presented the best results, in which were tried values of 5, 10, 15, and 20 for both operators. The probability of crossover (p_c) and mutation (p_m) is set to 0.9 and $1/n$, respectively, where n is the number of chromosomes of each individual. The tunning of these parameters did not present any significant difference among the tried values, so we choose the same as used by [141]. From the last iteration of the GA, we obtain a solution from the Pareto front for comparison with the BF approach. It is important to note that the flatness is computed in terms of ΔGSNR, which represents the average difference between the maximum and minimum GSNR in each band. Therefore, the objective is to maximize the average GSNR while minimizing ΔGSNR.

Finally, we conduct a network evaluation using SNAP for the German topology depicted in Figure A.1a. This topology consists of 17 ROADM nodes and 26 links. The objective is to compare the network capacity achieved through BDM upgrade with that obtained through SDM upgrade, assuming the same total number of channels (384) for both upgrade strategies. We perform a comprehensive analysis considering $30,000$ Monte Carlo iterations. A progressive-traffic analysis is conducted, assuming uniform traffic distribution. We employ the k-shortest path routing algorithm with a maximum of $k_{\max} = 15$ paths and employ the best GSNR wavelength assignment policy. In evaluating the traffic for each allocated LP, we assume perfectly elastic transceivers based on the Shannon limit. This approach allows us to focus on transmission limitations rather than considering the constraints imposed by specific transceiver technologies.

The evolution of the GA is illustrated in Fig. 3.12, which showcases the initial population as well as the Pareto front for multiple iterations. The plot represents the trade-off between the average GSNR and ΔGSNR. Remarkably, even after a few

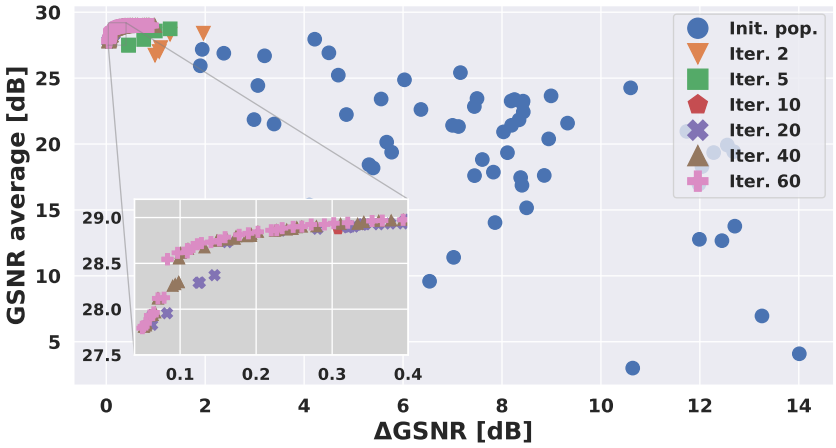

Fig. 3.12 Genetic algorithm evolution in terms of ΔGSNR and average.

iterations, the algorithm successfully discovers solutions in the top-left corner of the plot, characterized by high average GSNR and flatness. The zoomed plot of the final iterations demonstrates that the algorithm further enhances the population diversity, resulting in an increased number of non-dominated solutions.

Using a specific solution from the final Pareto front obtained in the GA strategy and the best solution found by the BF strategy, we compare them with the S-band without any compensation and present the results in Fig. 3.13. We also include the GSNR profile for the C-band only case (blue line), which was optimized using the BF approach. Firstly, we observe that the GA strategy (red lines) is capable of

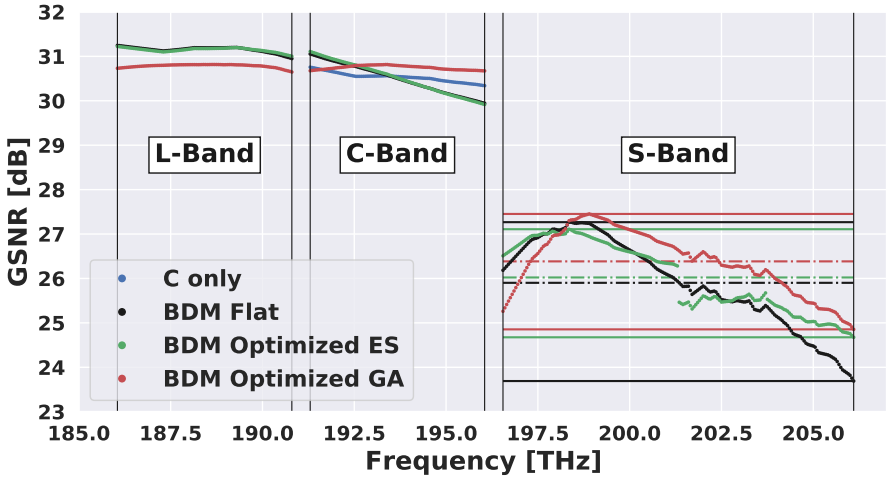

Fig. 3.13 GSNR profiles for all scenarios analyzed.

Table 3.3 ΔGSNR and GSNR average per spectral band for all scenarios analyzed.

Scenarios		Spectral bands		
		L	**C**	**S**
C-band only	**Avr.**	-	30.5	-
	ΔGSNR	-	0.4	-
BDM S-band flat	**Avr.**	31.1	30.5	25.9
	ΔGSNR	0.3	1.1	3.6
BDM Optimized ES	**Avr.**	31.1	30.5	25.9
	ΔGSNR	0.3	1.2	2.4
BDM Optimized GA	**Avr.**	30.8	30.7	26.4
	ΔGSNR	0.2	0.1	2.6

delivering an almost flat GSNR profile for the C- and L-band, increasing the average GSNR in the C-band compared to the C-band only case, while decreasing the average GSNR in the L-band. The decrease in the L-band is compensated by an increase in the average GSNR in the S-band (dashed line), while significantly improving the GSNR flatness in this band (solid lines representing the maximum and minimum values), compared to a profile without pre-tilt and offset in the same band (black lines). Regarding the BF strategy (green lines), the best profile found increases the flatness in the S-band (solid lines), compared to the BDM flat case, while slightly increasing the average GSNR (dashed line). The quantitative analysis of the average and flatness per band for each scenario is summarized in Table 3.3. When using the GA strategy, we obtain a ΔGSNR of 0.2, 0.1, and 2.6 dB, and average values of 30.8, 30.7, and 26.4 dB for the L-, C-, and S-bands, respectively. For the BF strategy, the values for flatness are 0.3, 1.2, and 2.4 dB, and the average values are 31.1, 30.5, and 25.9 dB for the L-, C-, and S-bands, respectively. Overall, the GA strategy demonstrates better performance with a fixed number of iterations. Since the GA algorithm typically uses a fixed number of iterations and population size, it can handle scenarios with more spectral bands and band subdivisions, similar to the approach used by the BF strategy, without increasing the total number of evaluations performed.

Finally, we present the results of the network assessment, comparing the performance of BDM-C+L+S (using the GA strategy) versus SDM (C-band only). To ensure a fair comparison, both techniques consider a total of 384 channels, which corresponds to four fiber pairs per link with 96 channels each. Figure 3.14 illustrates

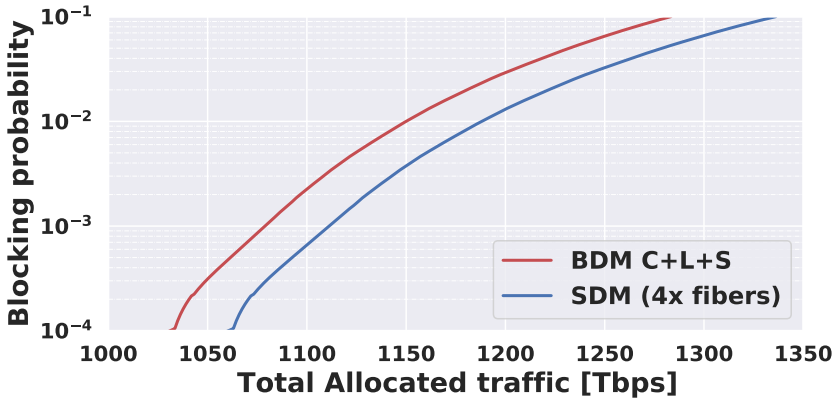

Fig. 3.14 Total allocated traffic versus BP applied to the German topology for BDM and SDM comparing with C-band only scenario.

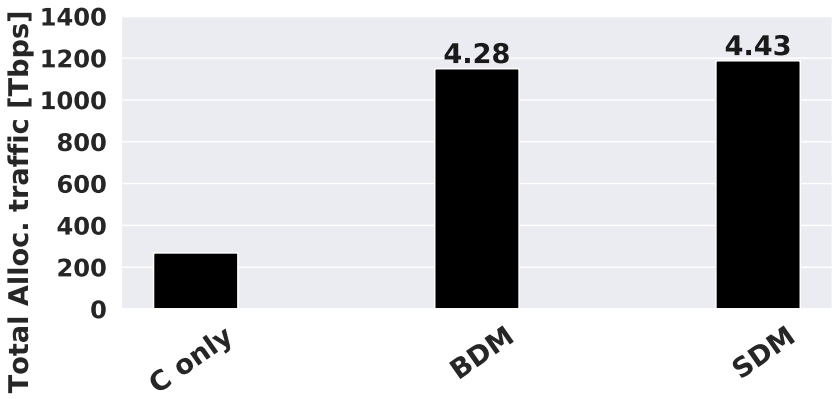

Fig. 3.15 Allocated traffic multiplicative factor applied to the German topology for BDM and SDM comparing with C-band only scenario.

the relationship between the total allocated traffic and the BP, ranging from 10^{-4} to 10^{-1}. Notably, the difference remains almost constant across the entire range of tested traffic loads. The largest discrepancy occurs at BP $= 10^{-1}$, where BDM achieves a total of 1284 Tbps, while SDM reaches 1337 Tbps. At BP $= 10^{-2}$, we present the traffic upgrade multiplicative factor in Figure 3.15, with the C-band single fiber pair case serving as the benchmark for both techniques. BDM increases the allocated traffic by a factor of 4.28 (1150 Tbps), while SDM achieves a factor of 4.43 (1188 Tbps). Although BDM upgrade performance is slightly worse, it is comparable to SDM in terms of delivered traffic. These findings indicate that the BDM solution, combined with an accurate multi-band power control strategy, is a

robust alternative for improving QoT and expanding network capacity without the need to install or lease new fibers.

Chapter 4

Multi-band optical network upgrade and design

In this chapter, we focus on how the multi-band upgrades can impact the already up-and-running C+L systems and how to minimize such impact. We start by analyzing the deployment addition of E-band transmission instead of S-band using experimental data characterization of BDFA, showing the addition of this band has low impact on C+L systems. The results were reported in [19]. This work is a jointly collaboration with WON team of Aston University, which were responsible to provide the BDFA characterization for the work presented in Section 4.1. Next, we present a comparison, for both transmission and network assessment, between the upgrade using S- and E-band and how they impact the C+L systems, which are reported in [22, 2]. In this work, we show how to provide a proper guard-band between the already running system and the new deployed spectral region can reduce the impact on that systems, and consequently reducing the number of deployed LPs which will require reconfiguration while considers different margins. This work was result of a collaboration with professor Nicola Sambo of Scuola Superiore di Sant'Anna. Finally, we present the work of [32] and extend it, showing a multi-band optical network design, in which in order to maintain the QoT levels the same as C+L system, we made use of deployment of new amplification site (AS). We shown that with a limited number of new ASs is possible to obtain the same or higher performance as SDM, reducing the number of required interfaces, depending on the topology where this approach is applied.

4.1 QoT evaluation of OLS transmission with BDFAs in the E-Band

To further extend network capability using additional transmission bands (e.g., the S-, E-, and O-bands) novel types of optical amplifiers are required. In this context, Bismuth-doped fibers have emerged as a promising solution for achieving broadband optical amplification due to their exceptional spectral flexibility and high performance characteristics [142–144]. However, there has been limited research conducted to evaluate the practical potential of BDFA for data transmission [145, 146]. In this study, we present a comprehensive numerical assessment of the QoT in an optical system where a BDFA, experimentally characterized in the S- and E-bands, is deployed to extend the transmission bandwidth beyond the conventional C+L-band system.

4.1.1 Bismuth doped fiber amplifier experimental setup

The experimental setup of the BDFA is presented in Figure 4.1(a). The optical amplifier configuration comprises two 14xx nm isolators, a pair of thin-film-filter wavelength-division multiplexers (TFF-WDMs), a 320 m long germanosilicate bismuth-doped fiber, a 1320 nm pump diode, and a 1320 nm isolator. The active medium of the amplifier is a germanosilicate bismuth-doped fiber fabricated at

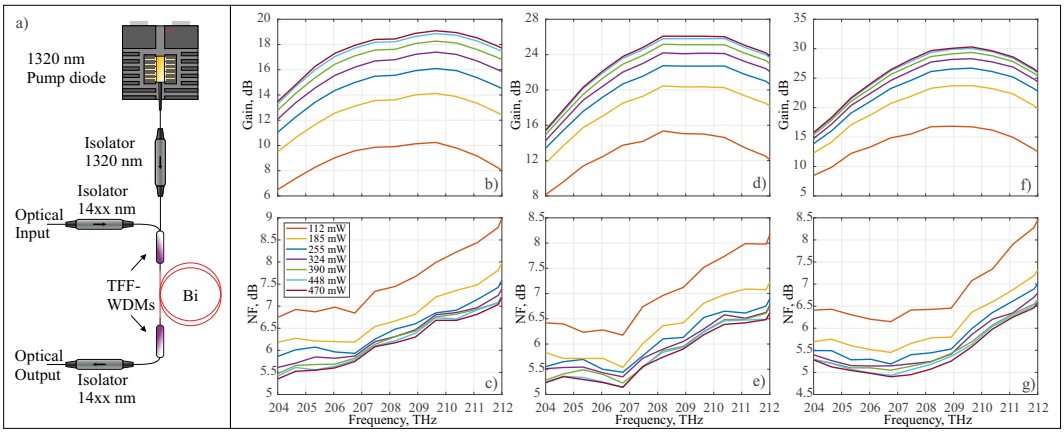

Fig. 4.1 a) schematic of BDFA; Dependencies of the measured gain (top) and noise figure (bottom) on frequency for different pump and b,c) 0 dBm; d,e) −10 dBm; f,g) −20 dBm input signal powers.

the Dianov Fiber Optics Research Center, Russia [142]. The fiber core composition, achieved through the modified chemical vapor deposition (MCVD)-solution doping technique, consists of 95 mol% SiO_2, 5 mol% GeO_2, and less than < 0.01 mol% of bismuth. The fiber core has a diameter of 9μm, while the cladding diameter is 125μm, ensuring full compatibility with SSMF. The bismuth-doped fiber has a numerical aperture of 0.14 and a cutoff wavelength of approximately 1.2μm. Due to the low concentration of Bi-related active centers, the optimal length of bismuth-doped fibers in optical amplifiers typically exceeds 100 m. The TFF-WDMs exhibit highly flat transmission characteristics in the 1300–1362 nm range and reflection characteristics in the 1370–1565 nm range, with an internal optical loss of about 0.1 dB. This low loss enables efficient coupling of wideband radiation into the bismuth-doped fiber. For forward pumping, a single 1320 nm pump diode is utilized, while the second TFF-WDM can be employed in conjunction with existing or additional pump diodes for backward or bidirectional pumping schemes. The forward pumping scheme is chosen to achieve the lowest noise figure compared to other pumping schemes with the same total pumping power level [144].

4.1.2 BDFA transmission modelling analysis

We commence by examining the optimal spectral region for data transmission in the E-band. In order to assess the QoT when employing the BDFA, Figure 4.2 illustrates the dependence of average, minimum, and maximum GSNR on the fiber length for a single span OLS operating with 64 channels at a baud rate of 64 Gbaud within a 75 GHz WDM grid. We consider two frequency ranges for evaluation: the range with the best average NF from 205.5 to 210.2 THz, and the range with the best average gain profile from 207.0 to 211.7 THz. The optimization of the average input power per channel is performed using the LOGO technique [129]. Figure 4.2 demonstrates that using the spectral region with the lower NF leads to an improvement of approximately 0.5 dB in the average GSNR compared to the region with the highest gain. Additionally, the BDFA exhibits better GSNR flatness in this case. Specifically, the variation in GSNR (ΔGSNR) for each OLS distance ranges from 1.8 to 2.0 dB and from 3.3 to 4.0 dB for the lower NF and higher gain frequency ranges, respectively. Given the superior performance of the frequency range with the lower NF, it will be the one considered henceforth.

To optimize the QoT, we investigated the impact of adjusting the average gain of the BDFA and correspondingly modifying the optimal launch power per channel. Fig. 4.3 depicts the relationship between the average GSNR in the E-band and the BDFA gain offset (in dB) for different OLS distances of 40, 60, and 80 km. The analysis considers data transmission in both the E-band alone and a scenario encompassing the C+L+E-bands. The reference point for the gain offset is the 0 dB setting, which corresponds to utilizing the default launch power calculated through the LOGO method, and adjusting the average gain of the BDFA accordingly. As depicted in Fig.4.3, the LOGO algorithm yields near-optimal launch power in both the E-band alone and together with C+L transmission. Additionally, the figure demonstrates the degradation in QoT within the E-band when the C+L system is active, compared to E-band transmission alone. The maximum GSNR degradation observed is 0.8 dB for the 80 km span (at optimum values). Furthermore, Fig.4.4 showcases the influence of adding the E-band to C+L systems, with the results presented for three different span lengths of 40, 60, and 80 km. The higher degradation of the larger spans is expected, as this span length will require a higher input power, and consequently will produce more NLI. Even so, this minor degradation suggests that utilizing a BDFA for E-band transmission holds promise for upgrading wideband scenarios in C+L systems, as the impact of the SRS effect is minimal. The top plot in Fig. 4.4 reveals that the average GSNR remains relatively unchanged when the E-band is added to the system. Conversely, the bottom plot illustrates a decrease in C+L flatness levels upon incorporating the E-band spectrum, as indicated by the increase in ΔGSNR. Notably, the highest increase is observed for a span length of 60 km. However,

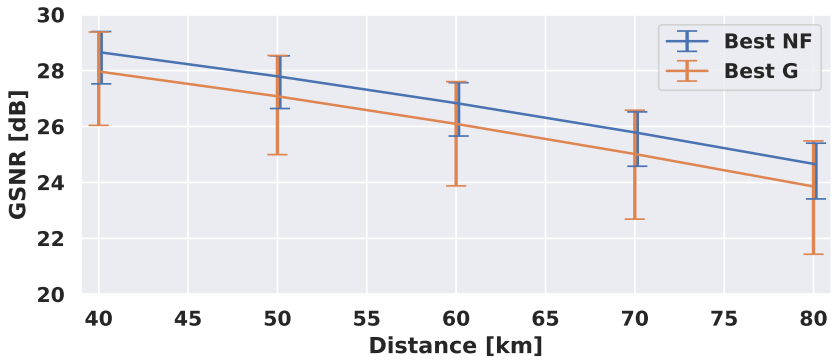

Fig. 4.2 Average GSNR (bars show the minimum and maximum value) dependency on a single span OLS considering the frequency ranges leading to the smallest NF (blue line) and highest gain (orange line).

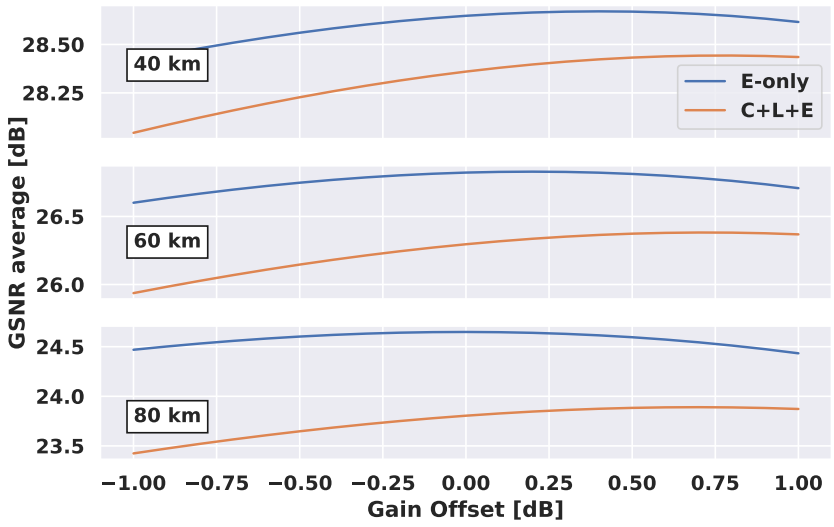

Fig. 4.3 Average E-band GSNR dependency on BDFA gain offset in a single span OLS for 40, 60 and 80 km with E-band only and C+L+E-band transmission.

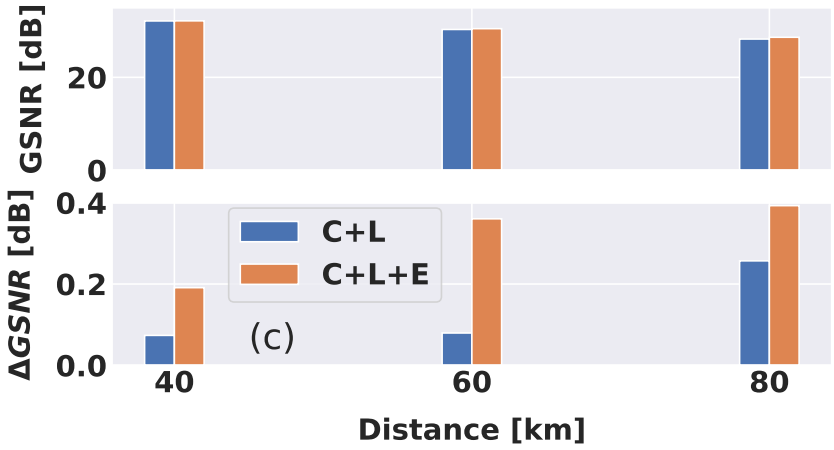

Fig. 4.4 GSNR average (top) and ΔGSNR (bottom) versus distance for the C- and L-bands using only C+L and C+L+E transmission.

despite this increase, the utilization of the E-band does not significantly attenuate the C+L systems. The change in flatness can be accommodated by existing system margins, ensuring that the upgrade scenario will not adversely affect the lightpaths already deployed.

Figure 4.5 showcases the relationship between the average GSNR per band and the number of spans, with each span of 80 km and the total distance varying from 80 to 640 km. Both C+L and C+L+E-band transmission scenarios are considered.

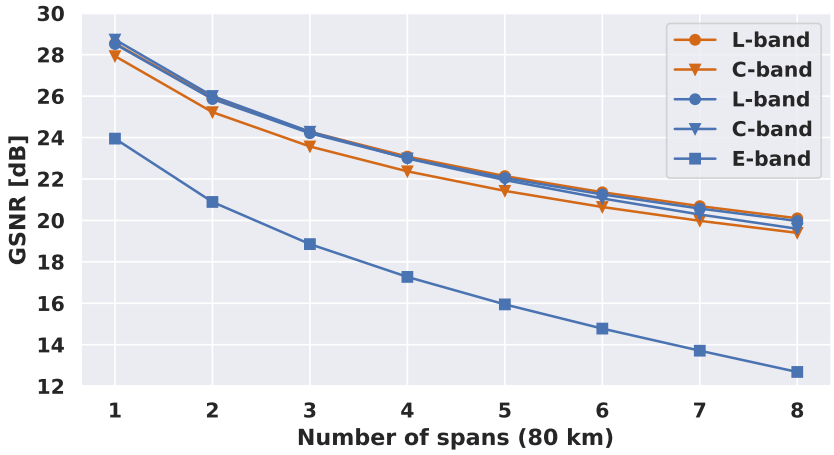

Fig. 4.5 Average GSNR per band vs number of spans for C+L (orange lines) and C+L+E (blue lines) transmission.

Notably, the addition of the E-band exhibits minimal degradation in the QoT for the C- and L-bands. This finding reinforces the feasibility of employing a BDFA for upgrading C+L systems by leveraging transmission over the E-band. As anticipated, the E-band experiences the highest degradation in GSNR, reaching a limit of 12.7 dB at the end of the last span. Consequently, the E-band can efficiently accommodate short-reach traffic offloading from the C- and L-bands. Furthermore, its utility can be enhanced by employing flexible transceivers such as ZR+ [147].

4.2 Network upgrade exploiting multi band: S or E-band?

When planning a network upgrade, e.g. to the S- or E-band, it is crucial to consider the impact of SRS on the existing channels in the C+L-band. The presence of SRS can lead to a degradation in the QoT of certain channels in the C+L-band, potentially falling below the forward error correction (FEC) threshold. Consequently, reconfigurations are necessary, such as switching to a lower-order modulation format or rerouting affected channels. The former adjustment may result in a reduction in bit rate, thereby requiring the allocation of additional channels to ensure the preservation of the original end-to-end capacity. Notably, these operational considerations related to the degradation of already active channels when activating an additional band have

not been extensively investigated in the existing literature on networking studies. While SRS is typically taken into account, the majority of contributions (e.g., [148–150]) primarily focus on provisioning schemes or resource allocation schemes, emphasizing the capacity enhancement achievable through the usage of multiple bands, rather than comprehensively analyzing issues pertaining to upgrades and operations.

In this section, we present the analysis of network upgrades based on the incorporation of the S- or E-band into an existing C+L-band system. For network upgrades leveraging the E-band, we propose the adoption of an optimized guard-band (GB) between the C- and E-band, as propose in [151]. The objective is to design the GB in a manner that significantly reduces or even eliminates the impact of the E-band on the C- and L-band traffic caused by SRS. This approach effectively avoids, at the cost of having fewer available channels, any degradation in the QoT for the channels already operating in the C- and L-band, ensuring a seamless upgrade process. Subsequently, a comprehensive evaluation of network performance is conducted to compare the two upgrade options: transitioning to the E-band with the optimized GB versus adopting the S-band. The evaluation considers the supported traffic increase and the reconfigurations required for the active channels in the C+L-band. The results indicate that upgrading to the E-band with a GB of 14 THz can be more advantageous, as it enables a comparable traffic increase to activate the S-band or the E-band with smaller GBs, while minimizing the need for reconfigurations on the existing channels in the C+L-band.

4.2.1 QoT comparison between C+L, C+L+S and C+L+E systems

In this study, we perform computations for different numbers of CUTs based on the proportion of total channels in each band: 4 cuts for the C-band, 7 cuts for the L-band, 7 cuts for the S-band, and 8 cuts for the E-band. Our analysis assumes optical channels operating at a symbol rate of 64 GBaud and a WDM grid spacing of 75 GHz. This configuration allows for a maximum allocation of 92 channels in the L-band, 54 channels in the C-band, 125 channels in the S-band, and 146 channels in the E-band. We also evaluate the impact in using an additional 1.5 THz of bandwidth in E-band by adding 20 channels more, resulting in 166 channels in total. For

the amplification, we consider commercial EDFA technology commonly used in C+L-band line systems, with average NF of 4.2 dB for the C-band and 4.7 dB for the L-band. It is important to note that we account for the frequency-dependent characteristics of the amplifiers. For the S-band amplification, we assume the use of TDFA with an average NF of 6.5 dB, as reported in [126]. In the E-band, we employ NDFA technology proposed in [152], with an average noise figure of 5.5 dB. Furthermore, in our analysis, we assume ideal amplifiers capable of fully recovering the input power at the end of each span. To perform the physical layer analysis, we utilize the GNPy open-source tool [95].

In order to assess the impact of upgrading an operational C+L system, we begin by establishing the working point of this system, which will remain unchanged during the upgrade deployment. To determine the launch power profile and evaluate the corresponding QoT, we follow the same procedure described in Section 3.2. For a span length of 60 km, the optimized launch power values are obtained as -1.62 dBm for the L-band and 0.58 dBm for the C-band. It is worth noting that this power optimization process is carried out for all span lengths in the network, as we will elaborate in the subsequent paragraphs. For the upgrades to S-band or E-band, we also perform the power optimization procedure for all span lengths, allowing adjustments to the tilt and offset parameters exclusively for the newly deployed band. Using this approach, we achieve average input power values of 0.76 dBm for the S-band and 2.27 dBm for the E-band. Based on our analysis, Figure 4.6 illustrates the GSNR profile for all CUTs, comparing three scenarios: (a) C+L-band, (b) C+L+S-band, and (c) C+L+E-band with a C-E band gap of GB $=$ 14 THz, for a single span of 60 km in length. The work presented in [151] has demonstrated that a C-E band gap of 14 THz provides a suitable bandwidth allocation with minimal impact on the QoT of the existing C+L band. This observation is further supported by Fig. 2.3, which shows that the Raman gain efficiency exhibits a peak intensity around this frequency offset, rapidly decreasing for larger spectral distances. By setting this gap, which represents unused spectrum, the channels in the E-band are sufficiently spaced from the C-band channels, reducing the interaction between them to a negligible level. While complete isolation cannot be achieved due to the long tails of the Raman efficiency, this gap effectively minimizes the interaction between the E- and C-band channels. Firstly, we confirm that employing this C-E band spacing for the C+L+E-band solution results in insignificant impact on the QoT. The average degradation of the minimum GSNR, considering all span lengths in the network,

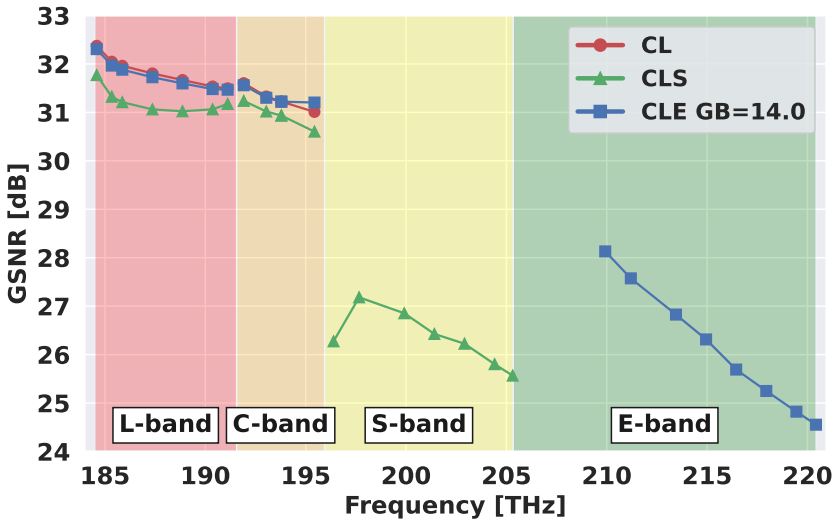

Fig. 4.6 GSNR profile versus frequency for C+L-, C+L+E- and C+L+S-band for a 60 km long span.

is less than 0.17 dB. In the E-band, the GSNR varies between 24.5 and 28.0 dB. Regarding the upgrade to the S-band, Fig. 4.6 highlights the impact (indicated by green triangles) on the minimum GSNR in the C- and L-band. The degradation in the minimum GSNR is 0.8 dB and 1.13 dB for the C- and L-band, respectively. Additionally, the GSNR in the S-band ranges from 25.5 to 27.2 dB.

Figure 4.7 illustrates the minimum GSNR as a function of the span length, ranging from 30 to 60 km, which represents the maximum span length in the considered network topology. The values are presented separately for each band and for each upgrade scenario. Analyzing the C-band (indicated by red curves), it can be observed that adding the S-band to the existing C+L-band system results in greater degradation compared to upgrading with the E-band. This difference is more significant for shorter spans, reaching a maximum degradation of approximately 0.92 dB. For the S-band upgrade (indicated by green curves), a similar behavior is observed with a higher impact on smaller spans. The maximum degradation of 1.3 dB occurs for a span length of 30 km. In contrast, the E-band upgrade shows negligible degradation across all span lengths in the C-band, with a maximum value of 0.2 dB. Comparing the QoT of the E-band and S-band upgrades, there is a nearly constant performance difference with an average of 1.5 dB. Despite the superior QoT performance of the S-band, the E-band can achieve comparable capacity by utilizing a wider bandwidth and accommodating more channels.

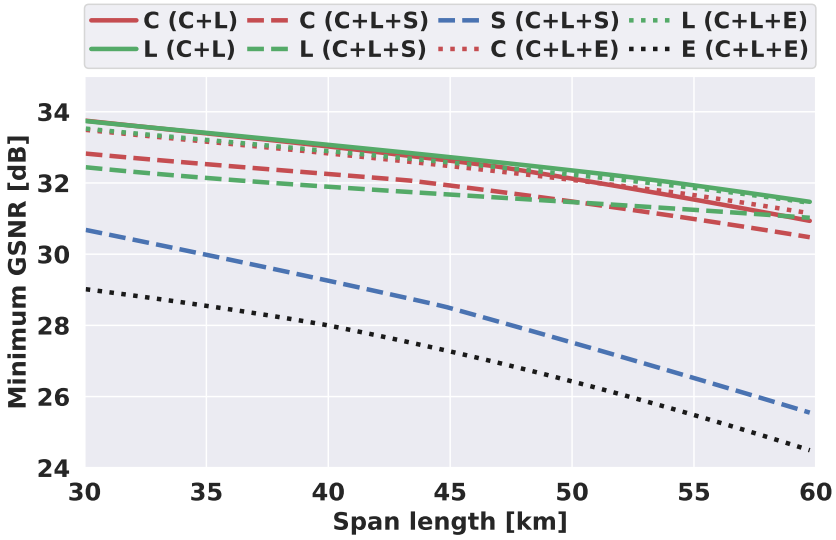

Fig. 4.7 Minimum GSNR per scenario (solid, dashed and dotted lines) per band (red, green, blue and black) versus span lengths.

Band	C+L+S	C+L+E (E=146 channels) GB=14 THz	C+L+E (E=166 channels) GB=12.5 THz
C-band	0.80	0.17	0.76
L-band	1.13	0.17	0.65

Table 4.1 Average GSNR penalty in dB per band/scenario.

Table 4.1 provides the average GSNR penalty for the different upgrade scenarios depicted in Figure 4.7. In addition to the two previously discussed scenarios, a third scenario is considered, where a smaller GB is employed, allowing an increased number of channels in the E-band, totaling 166 channels in this band. This third scenario aims to assess whether the addition of 20 channels, despite resulting in higher GSNR penalties due to a more limited guard band, can improve the overall network blocking probability. The results demonstrate that both the S-band upgrade and the wider E-band with a smaller guard band lead to higher penalties compared to the E-band with a 14 THz guard band, as presented in previous studies [151]. It is worth noting that the additional third scenario, with a more limited guard band but additional channels, explores the trade-off between GSNR penalties and the reduction of network BP.

4.2.2 Network upgrade assessment

The comparison between upgrades to the S-band and E-band is performed using a custom-built event-driven C++ simulator [2]. The simulation considers a 30-node Spanish backbone topology, as illustrated in Figure A.1f. The traffic follows a Poisson distribution with a mean inter-arrival time of $1/\lambda$. The mean connection holding time is exponentially distributed with a value of $1/\mu = 500$ s. The traffic load, expressed as λ/μ, is varied up to 7500 Erlang by adjusting $1/\lambda$. The simulation assumes dual polarization quadrature phase shift keying (DP-QPSK) and dual polarization 16 quadrature amplitude modulation (DP-16QAM) with a symbol rate of 64 GBaud. Requests for a net data rate of 400 Gbps are considered. These requests can be routed using a single 400 Gbps DP-16QAM signal occupying a 75 GHz frequency slot or two 200 Gbps DP-QPSK signals with a 150 GHz frequency slot allocated. The worst channel GSNR, considering cross-phase modulation, is assumed for each band. Threshold values for GSNR are determined to achieve a maximum pre-FEC bit error rate of 3×10^{-3}, following the back-to-back transceiver characterization in [79]. For DP-16QAM, the threshold is given by $\mathrm{TH}_{\mathrm{DP-16QAM}} = 16.1\mathrm{dB} + \mathrm{M}$, and for DP-QPSK, it is $\mathrm{TH}_{\mathrm{DP-QPSK}} = 9.5\mathrm{dB} + \mathrm{M}$, with M representing network margins accounting for factors such as aging [153]. Path computation is based on load balancing [154], and the FF policy is employed for spectrum allocation (SA) within the chosen band. The preference is given to the C-band, and if the spectrum continuity constraint cannot be satisfied in the C-band, the L-band is used. The S-band or E-band are use when the spectrum continuity constraint cannot be met in both the C-band and L-band. If the spectrum continuity constraint cannot be satisfied in any of the C-, L-, S-, or E-bands, the request is blocked. Upgrades to S- and E-band are compared in terms of both blocking probability and the number of reconfigurations required to guarantee QoT in C+L-band when activating the new band.

Figure 4.8 illustrates the BP versus traffic load for three network upgrade scenarios: C+L-band, C+L+S-band, and C+L+E-band (with guard bands of 12.5 THz and 14.0 THz between E-band and C-band) with no margins ($M = 0$). The exploitation of the S-band or E-band leads to a significant reduction in blocking probability. Interestingly, all three network upgrades exhibit similar blocking probabilities. For instance, at a blocking probability of 10^{-2}, the utilization of the E-band or S-band allows for supporting nearly double the traffic compared to the C+L-band alone.

When comparing the upgrade to the S-band with the upgrade to the E-band with a 14.0 THz guard band, although the latter exploits more spectrum (approximately 1.5 THz more), the GSNR in the E-band is lower than that in the S-band (around 1.0 dB for a single span). This difference in GSNR results in a higher utilization of lower-order modulation formats in the E-band, which requires more spectrum per request but balances the increased spectrum availability. A similar effect is observed when comparing the two different upgrades within the E-band, with guard bands of 12.5 THz and 14.0 THz, respectively. Despite the additional channels in the E-band with a smaller guard band, the blocking probability remains comparable. This is due to the lower GSNR associated with the 12.5 THz guard band, resulting in a greater impact of nonlinear effects and a higher usage of lower-order modulation formats.

Furthermore, it is important to note that the network upgrade may not always be seamless, as it can require reconfigurations in the C+L-band due to the influence of SRS when introducing a new band. Specifically, when upgrading with the S-band or E-band and a 12.5 THz guard band, an impact is observed on the already active channels in the C+L-band. Conversely, as mentioned earlier, it has been observed that deploying the E-band with a 14.0 THz guard band does not necessitate any reconfiguration of the channels in the C+L-band.

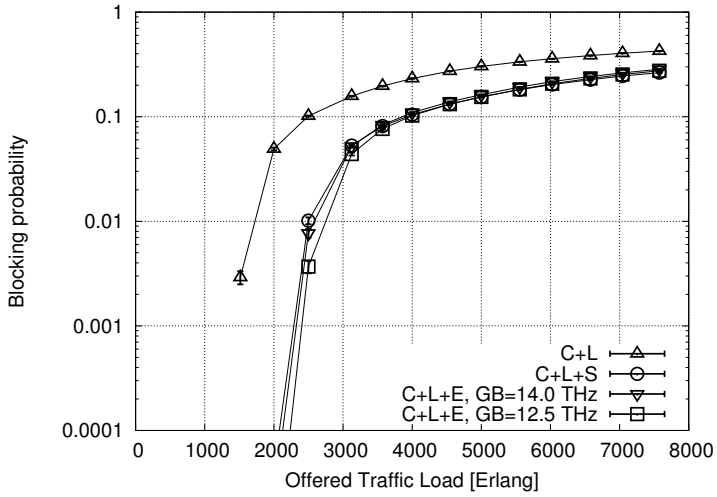

Fig. 4.8 Blocking probability versus traffic load with no margins.

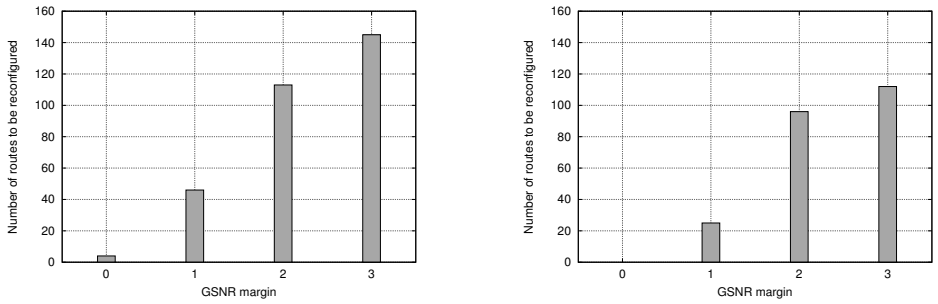

(a) (b)

Fig. 4.9 Margin M versus number of routes requiring reconfiguration when exploiting (a) S-band, and (b) E-band with GB = 12.5 THz.

Figure 4.9a illustrates the number of routes that necessitate reconfigurations, such as rerouting, modulation format changes, or bit rate reductions, as a function of the margin value M when upgrading to the S-band. It should be noted that the simulations assume a change in modulation format (always from DP-16QAM to DP-QPSK) with a corresponding reduction in bit rate in cases where reconfiguration is required. Alternatively, additional channels could be established to maintain the original bit rate. With no margins ($M = 0$), only 4 out of 870 routes require reconfigurations in the C+L-band channels when adopting the S-band upgrade. The number of routes requiring reconfigurations increases with larger margin values, as the QoT requirements become more stringent. Consequently, more routes become critical, with a GSNR close to the threshold, such that the GSNR variation caused by SRS brings it below the $\mathrm{TH}_{\mathrm{DP-16QAM}}$ threshold. For instance, with $M = 1$ dB, reconfigurations would be necessary for channels along more than 40 routes. Similarly, the upgrade to the E-band with a 12.5 THz guard band may also result in reconfigurations in the C+L-band, as depicted in Figure 4.9b. Although no reconfigurations are needed for the assumed scenario with $M = 0$, some reconfigurations are required when increasing the margin. For example, with $M = 1$ dB, reconfigurations would be required for channels along more than 20 routes. By comparing Figure 4.9a and Figure 4.9b, it becomes evident that upgrading to the S-band leads to more reconfigurations in the C+L-band compared to the upgrade to the E-band with a 12.5 THz GB.

Figure 4.10 depicts the blocking probability as a function of M at a load of 2500 Erlang. As anticipated, the blocking probability increases with larger margin values, as the QoT becomes more stringent, resulting in the adoption of the less

spectrally efficient DP-QPSK format, which requires a wider bandwidth (150 GHz instead of 75 GHz). For the given load, the upgrade to the E-band with a 12.5 THz guard band exhibits slightly better performance than the other upgrades when the margins are limited ($M \leq 2$ dB). However, with $M = 3$ dB, the upgrade to the E-band with a 12.5 THz guard band demonstrates slightly worse performance. This discrepancy can be attributed to two factors. Firstly, with a 12.5 THz guard band, the GSNR in the E-band is lower compared to that of the 14 THz guard band due to the influence of SRS. Secondly, a $M = 3$ dB margin imposes a higher threshold on the GSNR. Consequently, the combination of a lower GSNR and a higher threshold necessitates more frequent usage of DP-QPSK, resulting in the occupation of a wider bandwidth and consequently a higher blocking probability.

The network simulations have demonstrated that upgrading to the E-band with a well-chosen guard band between the E- and C-band may be more favorable compared to upgrading to the S-band. On one hand, both upgrade scenarios in the E-band and S-band achieve similar increases in traffic capacity, with the E-band allowing for nearly double the traffic compared to the original C+L-band system. On the other hand, upgrading to the E-band with a properly designed guard band (GB = 14.0 THz in the specific scenario considered) does not require any channel reconfigurations in the C+L-band, such as modulation format adjustments. However, the upgrade to

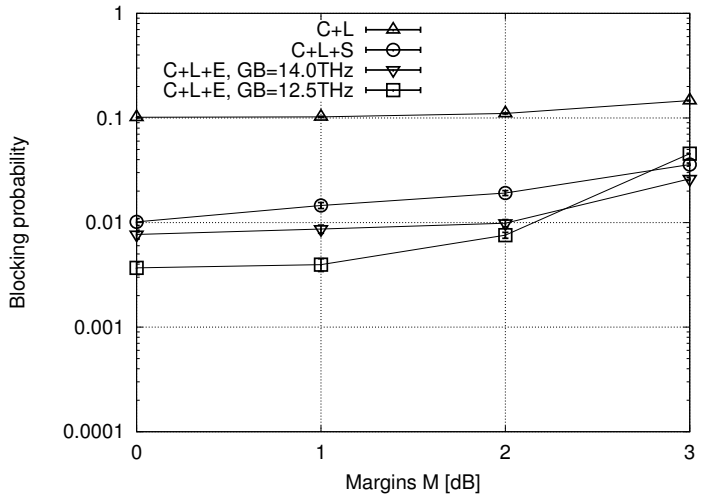

Fig. 4.10 Blocking probability versus margin M at a load of 2500 Erlang.

the S-band or the E-band with a smaller guard band of GB = 12.5 THz may have an impact on the quality of transmission in the C+L-band, necessitating channel reconfigurations to maintain the desired quality of transmission. Future research can explore network upgrades and reconfigurations in the presence of advanced transmission systems, such as probabilistic constellation shaping, which offer more refined trade-offs between optical reach and spectral efficiency.

4.3 Multi-band optical network design

In order to enable MBT upgrade, network design strategies need to be addressed in terms of performance and costs, analyzing parameters such as amplification placement and minimization of used interfaces. Several investigations have been carried out on the design of optical networks, with and without the usage of MBT systems. In [155], a network design strategy is presented for a geographically dependent, fiber-based capacity upgrade using C- and C+L-band systems, whereas in [156] a comparison between C+L-band systems and multi-fiber is reported, highlighting that MBT upgrades are beneficial even in the case of low costs for fiber leases. An amplifier placement strategy is carried out in [157], deploying additional amplifiers in protected mixed-line rate optical networks. An optimized hybrid Raman/EDFA placement is carried out in [158] in order to minimize the number of used 3R regenerators. In [159] three strategies for placing an L-band amplifier were analyzed to extend the C-band system, showing a trade-off between spectrum efficiency and costs. In this work, we consider the network design for the deployment of a fixed number of new amplification site applied to a network upgrade from C+L to C+L+S system. Moreover, due to band separation losses and costs associated with the deployment of a new AS, we assume that each AS amplifies all used bands, unlikely to occur with the work of [159]. Our analysis evaluates the overall network performance in terms of delivered traffic, as well as costs in terms of transceiver interfaces and the total number of amplifiers used. We compare this approach with the performance of a network with multiple fibers (2 and 3 times), in order to determine the additional capital expenditure (CAPEX) required to achieve the same performance as C-band only systems.

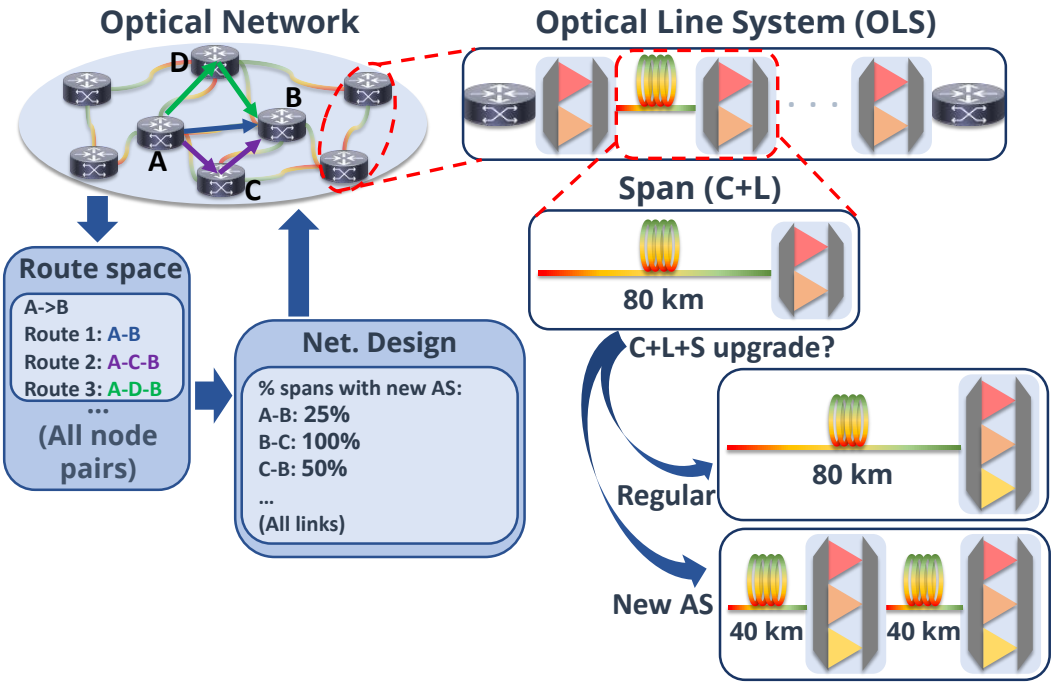

Fig. 4.11 Illustration of network and OLS abstraction for spans using C+L transmission systems with 80 km and two possible C+L+S upgrade scenarios: (1) Regular, which keeps the span length adding a S-band amplifier at the already deployed AS and (2) New AS, which divides the span in half, adding a new set of amplifiers for the three bands in a new AS.

4.3.1 Design and upgrade strategies for multi-band transmission networks

The multi-band upgrade beyond C+L systems is the use of the S-band spectrum, adding an amplifier specific to this band to each AS, as shown in Fig. 4.11 by the name of C+L+S Regular. This solution can increase the overall network capacity with a limited increase in capital or operational expenditure (CAPEX/operational expenditure (OPEX)). For spectral bands beyond the C+L-bands, the average fiber attenuation is higher, and the amplification technologies lack maturity. Moreover, due to the impairments that occur during wideband transmission, including nonlinear interference generation and SRS effects (described in detail in Section 2.1), these bands have different QoT values, producing a lower capacity per channel [14]. Due to that reason, another possible solution for multi-band upgrading networks beyond C+L is the addition of another AS, besides the same amplifier of Regular C+L+S strategy, decreasing by half the span length. The first point of this strategy, shown in Fig. 4.11 and named C+L+S New AS, is that instead of amplifying only the S-band,

Algorithm 1 Network design for new AS distribution

Require: $RS_{k=1}$: network route space only for the shortest path ($k = 1$); L: list of network links; p: percentage of spans to receive a new AS;
Ensure: A: List of new AS per link.

$t \leftarrow 0$
$A, U \leftarrow \emptyset$
for all link l in L **do**
    $A_l, U_l \leftarrow 0$
    $S_l \leftarrow$ number of spans of link l
    $t \leftarrow t + S_l$
end for
$n = t \cdot p$ ▷ Total number of new AS to distribute
$t \leftarrow 0$
for all route r in $RS_{k=1}$ **do**
    for all link l in r **do**
        $U_l \leftarrow U_l + 1$
        $t \leftarrow t + 1$
    end for
end for
for all link l in L **do**
    $A_l \leftarrow round(U_l/t \cdot n)$ ▷ Normalization times total number of new AS
    if $A_l > S_l$ **then**
        $A_l \leftarrow S_l$
    end if
end for
$s \leftarrow 0$ ▷ Spare ASs
if $\sum_{l \in L} A_l < n$ **then**
    $s \leftarrow n - \sum_{l \in L} A_l$
end if
while $s > 0$ **do**
    $l \leftarrow$ link with higher usage U_l in which $A_l < S_l$
    if $(S_l - A_l) \leq s$ **then**
        $s \leftarrow s - (S_l - A_l)$
        $A_l \leftarrow S_l$
    else
        $A_l \leftarrow A_l + s$
        $s \leftarrow 0$
    end if
end while

which presents the higher QoT penalties, we added amplifiers for all bands. The amplification of only the bands with higher penalties is not justified, as most of the CAPEX is on the extra amplification site infrastructure, not on the amplifiers. Second, this approach drastically increases the overall network CAPEX/OPEX, as each 80 km span requires an AS deployment, which can be unfeasible in terms of costs.

This work proposes an allocation policy for a limited number of new ASs as a result of the significant increase in terms of the cost of the C+L+S New AS approach for all spans. The proposed network design is based on the network route space (RS), as illustrated in Fig. 4.11 (left side) and described in detail in Alg. 1. From our previous analysis, we found that focusing on the distribution of new AS only among the shortest paths (route space of $k = 1$) is more beneficial, even if during the allocation process we have $k = 5$ possibilities for each pair of nodes. The

analysis performed on the usage of the route space (RS) only for $k = 1$. Moreover, the algorithm requires the percentage of spans in the network in which the length is halved. Firstly, we initialize the sets of the number of new AS per link (A) and link usage (U) between lines 3 and 7, also counting the total number of spans (t) in the network. With the total number of network spans, we can compute the total number of ASs (n) which will be distributed among the links, as shown in line 8. Between lines 10 and 15 we count the number of times each link, as well as the total number of links (t), is used by the RS. The loop between lines 16 and 21 sets the amount of new AS per link, multiplying the normalized usage set U/t times n and then checking if this number is higher than the total number of spans in each link (line 18). As some links present a high degree of importance, the result of this multiplication can lead to the results that some links might receive more ASs than the number of spans. If that occurs, the proposed algorithm sets all spans in this link to receive a new AS. Moreover, in line 23 is evaluated if the total number of new AS (A) to be installed is less than the total number defined in n, computing the number of spare new ASs (s). Finally, the spare new AS that were not allocated are distributed among the links with higher utilization that have not reached the maximum number of upgrades (between lines 26 and 35). The proposed algorithm prioritizes the link with higher usage among the shortest paths, focusing on links that are more likely to be used during the connection allocation process in the network. Moreover, this allocation policy is traffic-independent, meaning that even if the traffic pattern changes during network operation, the distribution of new ASs may still be close to optimal. In this work, we evaluate the impact of the upgrade from a C+L system to all spans using the Regular upgrade, namely C+L+S 0% (indicating the percentage of network spans that will be halved and receive a new AS). In addition, we test the allocation policy when 10, 20, 40, and 60% of all network spans receive an extra AS, in order to evaluate whether with a limited CAPEX/OPEX increasing is possible to obtain the same or close to the approach in which all spans lengths are halved (C+L+S 100%).

In order to assume a more realistic transmission scenario, if compared to the simulations performed in previous sections, we add: 0.25 dB for connectors losses, multiplexer (MUX)/demultiplexer (DEMUX) insertion losses in amplification sites of 2 and 1 dB, respectively, ROADMs PDL of 0.5 dB/node traversed by the LP, ROADMs filtering penalties as proposed in [160] and splice losses of 0.01 dB/km, the latter in order to cope with fiber aging. Finally, the control plane sets a 1.0 dB

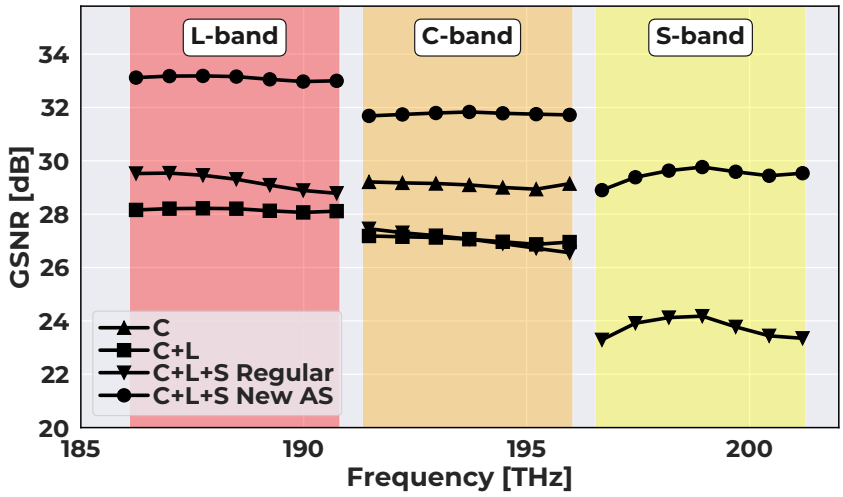

Fig. 4.12 GSNR profile of a single span for all scenarios.

system margin to cope with other detrimental effects and the impact of aging before choosing the supported modulation format for each lightpath.

It should be mentioned that the input power profile for all scenarios was obtained by the tilt and offset strategy proposed in [9], with the aim of delivering the highest and flat GSNR profile possible. Using this power optimization strategy, the C-only case presented an average input power per channel of 0.0 dBm while in the C+L scenario, we found an average power per channel of 0.3 and 0.6 dBm for the L- and C-bands, respectively. On the one hand, in the C+L+S Regular scenario, the average powers are -0.7, -0.6, and 3.0 dBm/channel for L-, C-, and S-bands, respectively. Finally, the average power per channel decreases to -3.4 dBm for the C-band, -2.9 dBm for the L-band, and -0.3 dBm for the S-band for the C+L+S New AS scenario. The GSNR profile for C-only, C+L, and C+L+S Regular, after a single 80 km span, and for C+L+S New AS, after two 40 km spans, are presented in the far right side of Fig. 4.12. First, the C-only scenario presents an average GSNR of 29.0 dB. The C+L transmission scenario presents an average GSNR of 28.1 and 27.0 dB for L- and C-bands, respectively. For the case in which the S-band amplifier is only added at the end of the 80 km span (C+L+S Regular), we obtain GSNR averages of 29.2, 27.0, and 23.8 dB for L-, C-, and S-bands, respectively. If we compare the C+L and C+L+S Regular cases, we can see a small improvement in the L-band GSNR average. This is caused by the additional channels in S-band, which generates a higher power transfer due to the SRS, causing this band to require less gain and consequently producing less ASE noise. Moreover, as the input power in

L-band is reduced, if compared to the C+L system, to compensate for the SRS effect, we are able to maintain the NLI levels, thus generating an increase in GSNR. Finally, the new approach, where a new amplification site is put after 40 km (C+L+S New AS), leads to improving the QoT in all bands. For example, the GSNR averages after 80 km are 33.1, 31.7, and 29.5 dB for L-, C-, and S-bands, respectively. In this approach, the GSNR values increased to 3.9, 4.8, and 5.7 dB in the L-, C-, and S-band, respectively, compared to the C+L+S-band Regular. According to this plot, adding an extra amplification site after 40 km can bring the S-band GSNR to values comparable to the ones of the C + L systems, which can be used in this band for more efficient modulation formats. However, this upgrade can greatly increase both the CAPEX and the OPEX of the network, as each span in the network requires an additional AS.

SNAP progressive-traffic analysis was performed for 1500 Monte Carlo iterations, in which the network is progressively populated with connection requests following the parameters used as input, such as request date rate (400 Gbps) and nodes distribution (uniform and population-based) [1] until a threshold criterion is achieved, in our case a maximum blocking probability of 5%. The SNAP control routing policy used is the algorithm of k-shortest paths with $k_{\max} = 5$ and FF as wavelength assignment policy. All established connections are fully transparent and the modulation format used, based on OpenZR+ MSA [147], depends on the absolute path GSNR, supporting three modulation formats (QPSK, 8QAM, and 16QAM) and four data rate values per channel (100, 200, 300 and 400 Gbps). The required GSNR (RGSNR) for all data rates supported by our transceiver assumption and its respective power consumption are reported in Table B.1. Besides all physical layer penalties described in this section, the SNAP control plane adds a QoT system margin of 1.0 dB for each lightpath to ensure correct system operation. Finally, the network assessment is performed for two network topologies: (1) Italian (Figure A.1d) with 21 nodes, 35 bidirectional links, an average link length of 209 km, and an average node degree of 3.4; and (2) Japanese (Figure A.1e) with 25 nodes, 43 bidirectional links, an average link length of 305 km, and an average node degree of 3.4.

4.3.2 Network design results

RS k usage analysis

As described in Section 4.3.1, our proposed AS allocation algorithm is based on RS, to determine the priority of the links for the allocation process. Moreover, is also mentioned that the RS is composed of 5 shortest paths between each node pair in the network. Regarding that, Fig. 4.13 presents a simulation using the C+L scenario (with $\mathrm{BP}_{thr} = 5 \cdot 10^{-2}$) for Italian and Japanese topologies for uniform and population-based traffic patterns, showing the ratio of which k-shortest path is used during the allocation process. Logically, we notice that when the network is free and starts to be populated with new connection requests, only the first k-shortest paths are used. Additionally, when the network becomes more congested, the other RS paths start to be used. Fig. 4.13 also presents (dotted lines) the lower percentage of $k = 1$ shortest path usage, varying between simulations from 75 to 58%, with the latter for the Italian topology using a population-based traffic, shown by Fig. 4.13b. With these results, it is clear that the ratio between the usage of the $k = 1$ path is higher than the sum of ratios of the other paths during the lifetime of a network, with a significant part of it using only the shortest path. As the new AS strategy improves the QoT, and consequently will improve the performance in terms of usage possibility of high modulation formats, if only a few numbers of them are available for allocation we should prioritize the links that are more likely to be used during the network lifetime. For this reason, our allocation strategy to deploy new ASs (described in Alg. 1) used the $\mathrm{RS}_{k=1}$.

Traffic versus BP analysis

The first analysis carried out evaluates the BP (varying from 10^{-4} to $5 \cdot 10^{-2}$) versus the network total allocated traffic for the reference C+L scenario, C+L+S 0%, and the cases where 20, 40, 60% and 100% of the network spans receives an additional amplification site. Moreover, all the delivered traffic values described for $\mathrm{BP} = 10^{-2}$ are presented in Table 4.2 for easier comparison. Fig. 4.14a presents the results for the Italian topology using the uniform traffic distribution. Notice that all mentioned delivered capacities for all scenarios are in the $\mathrm{BP} = 10^{-2}$. According to it, whereas the C+L MBT configuration delivers 196.8 Tbps, the C+L+S 0% supports 306.5 Tbps. It is clear that exploiting the S-band leads to extending the network

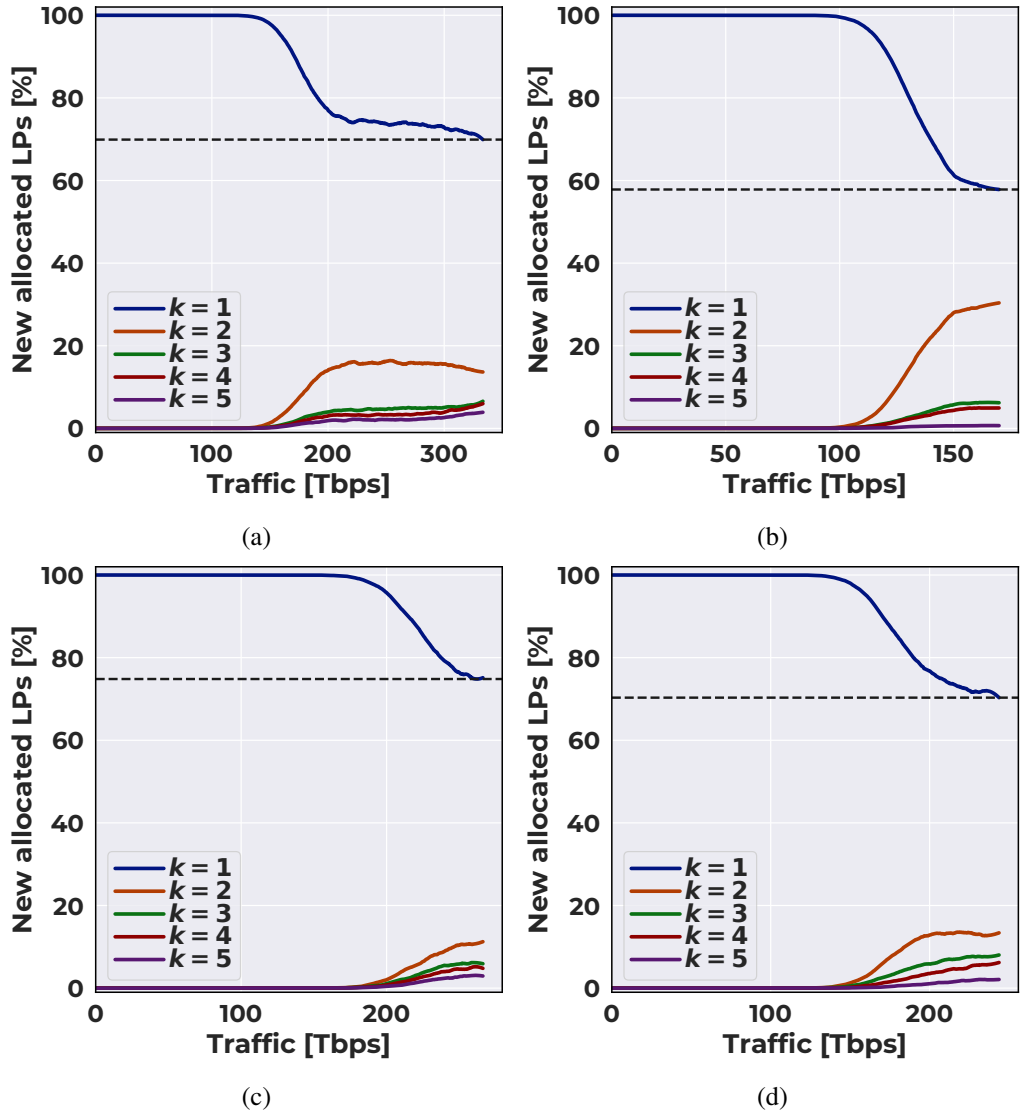

Fig. 4.13 RS k percentage usage versus traffic for C+L simulation for Italian topology, using (a) uniform and (b) population-based traffic, and for Japanese topology using (c) uniform and (d) population-based traffic with threshold BP $= 5 \cdot 10^{-2}$.

throughput by 56% compared to the reference C+L scenario. Moreover, C–2× delivers 236.8 Tbps (20% increase) and C–3× scenario delivers 356.5 Tbps (81% increase). In the C+L+S 100% case, the network capacity increases to 487.9 Tbps, which is 148% more than the C+L scenario. This huge capacity extension is because of the higher QoT of this MBT scenario, consequently supporting more efficient modulation formats of the transceiver used in this work. If the C+L+S 0% scenario is used as a reference, the deployment of the new ASs in all network spans (C+L+S 100%)

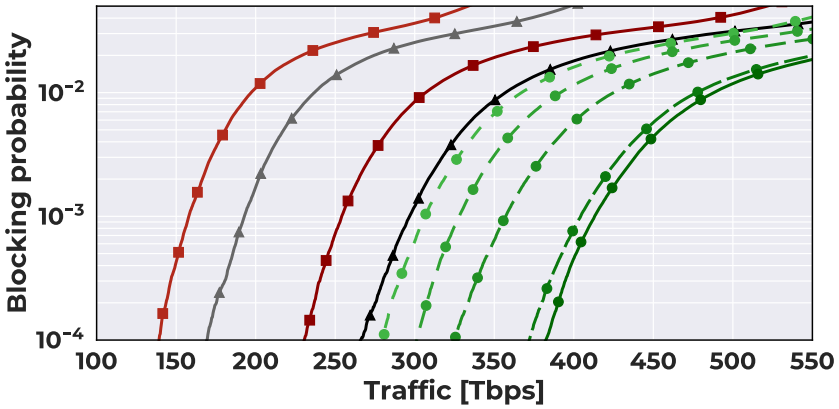

(a)

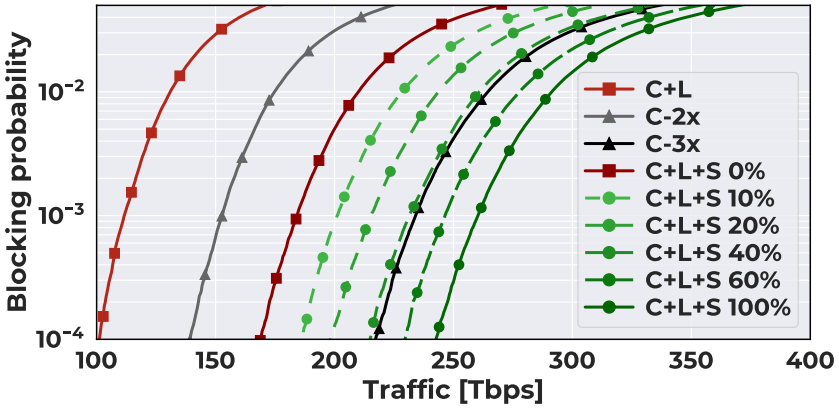

(b)

Fig. 4.14 Network overall delivered traffic versus blocking probability for Italian topology with (a) uniform traffic and (b) population based traffic.

results in a traffic increase of 59%, maximum traffic increase possible by the deployment of new ASs. Moreover, using the proposed deployment strategies, it is possible to increase the network capacity by 20% (366.7 Tbps), 28% (366.7 Tbps), 39% (392.8 Tbps), and 56% (451.9 Tbps) when restricting the upgrade to 10, 20, 40, and 60% of the total number of spans, respectively. This means that using the proposed site allocation policy, with 60% of the spans being halved, we can achieve almost the same traffic increase as C+L+S 100% (solid yellow curve). Additionally, receiving a new AS in only 10% of the network spans slightly outperformed the multi-fiber system with the same amount of channels (C–3×). Fig. 4.14b presents the analysis for the Italian network with a population based traffic node distribution. According to this figure, the network throughput in the C+L scenario is about 130.7 Tbps; Moreover, it grows to 209.9, 174.6, 264.2, and 291.1 Tbps by exploit-

ing C+L+S 0%, C–2×, C–3×, and C+L+S 100% MBT configurations, respectively. Comparing C+L+S 0% and 100%, the network capacity increases by 39%. For this traffic pattern, considering the C+L+S 0% as a reference case, the proposed allocation strategy was able to increase the overall delivered traffic by 9%, 16%, 24%, and 32% for 10, 20, 40, and 60% scenarios, respectively. If we consider the difference obtained from the C+L+S 0% to the C+L+S 100% scenarios as the maximum capacity enhancement possible, we achieve 61 and 82% of this enhancement with 40 and 60% in the new AS installed. Moreover, we can see that for this traffic pattern, the New acas strategy was able to achieve the same performance as the C–3× when 40% of the spans are halved. According to two Figs. 4.14a and 4.14b, it is clear that nonuniform traffic distribution presents a lower performance in terms of overall delivered traffic, compared to the uniform scenario. This can be explained by the population distribution and is a characteristic of the topology itself, as already shown in [1] for other topologies. Overall, although the network throughput decreases when applying a nonuniform traffic distribution to this network, the proposed method shows its benefit on the capacity extension for both cases.

Next, we present the SNAP simulation for the Japanese network topology using a uniform traffic pattern is presented in Fig. 4.15a. For BP $= 10^{-2}$, delivered network capacity is 314.8 (37% increase), 246.3 (7.0% increase), 375.4 (63% increase), and 475.6 Tbps (107% increase) for C+L+S 0%, C–2×, C–3× and C+L+S 100%, respectively, compared with the C+L scenario, which achieved 234.4 Tbps. Compared with the C+L+S 0% scenario, the network capacity gains achieve 9, 13, 30, 45, and 51% for the scenarios using 10, 20, 40, and 60% and 100% of additional AS, respectively. In this case, we can see that the performance of the C–3× scenario is between 20 and 40% cases. Moreover, by upgrading 60% of the spans we achieve 88% of the traffic increase provided by all spans receiving a new AS. The last traffic versus BP analysis is presented in Fig. 4.15b for the Japanese optical network topology with population-based traffic pattern. The total traffic delivered is 203.6, 219.0, 334.2, 282.0, and 426.5 Tbps for C+L, C–2×, C–3×, C+L+S 0%, and C+L+S 100%, respectively. Compared with the C+L+S 0% scenario, the proposed allocation obtained a traffic increase of around 12, 16, 34, and 46% with 10, 20, 40, and 60% of spans upgraded while this increase achieved 51% for C+L+S 100%. To be precise, the total allocated traffic for the C+L+S 60% and C+L+S 100% MBT scenarios are 411.1 and 426.5 Tbps, respectively. Also, for this traffic pattern, the results show that the proposed new AS allocation policy can achieve a network capacity close to

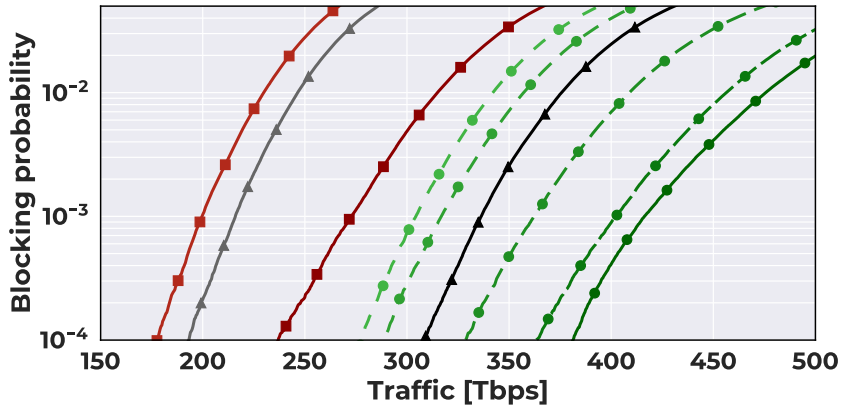

(a)

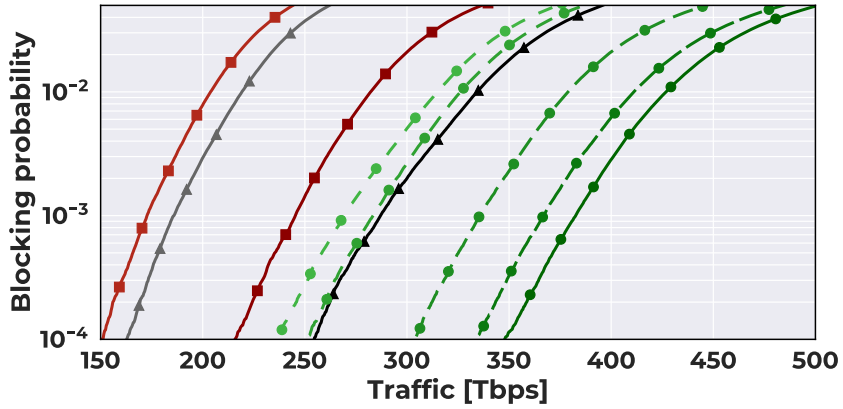

(b)

Fig. 4.15 Network overall delivered traffic versus blocking probability for Japanese topology with (a) uniform traffic and (b) population based traffic.

C+L+S 100% case with 60% of the network spans receiving a new AS. Additionally, the performance for the C+L+S 20% achieved almost the same performance as the C–3×. Finally, the proposed allocation strategy presented good results for the two topologies used with both traffic patterns tested, showing the benefits of using a traffic-agnostic allocation policy.

Number of amplifiers versus number of interfaces

Next, we show in Fig. 4.16 the results of our new AS allocation strategy in terms of the number of demanded interfaces and the total number of amplifiers used for a specific delivered traffic point, corresponding to the traffic delivered for BP $= 10^{-2}$ for the C+L scenario. Fig. 4.16a shows the results for the Italian topology for

Table 4.2 Overall delivered traffic for all upgrade scenarios, topologies and traffic patterns with BP $= 10^{-2}$.

Upgrade	Traffic [Tbps]			
	Italy		Japan	
	Uni.	Pop.	Uni.	Pop.
C+L	196.8	130.7	229.7	203.6
C-2x	236.8	174.6	246.3	219.0
C-3x	356.8	264.2	375.4	334.2
C+L+S 0%	306.5	209.9	314.8	282.0
C+L+S 10%	366.7	228.1	341.8	314.8
C+L+S 20%	391.3	243.6	356.8	325.9
C+L+S 40%	424.9	260.6	408.7	378.6
C+L+S 60%	477.2	277.6	456.2	411.1
C+L+S 100%	487.9	291.1	475.6	426.5

uniform, with allocated traffic of 196.8 Tbps, and for nonuniform, with allocated traffic of 130.7 Tbps. The reference uniform C+L scenario requires the use of 676 optical interfaces and C–2× requires 595, whereas the reference population-based C+L requires 420 and the C–2× 353, all cases using 332 optical amplifiers (166 for each band/fiber). When considering the C+L+S 0% scenario, the uniform case uses 617 interfaces while the population uses 376, both using a total of 498 amplifiers. Moreover, the C–3× required the same amount of interfaces as the C–2× using the same amount of amplifiers as the C+L+S 0% scenario. The decrease in the number of interfaces (C+L to C+L+S 0%) for both traffic patterns is a consequence of slightly higher GSNR levels in the L-band and the specific traffic point, which, as is not heavily loaded, does not use channels in S-band, due to the FF policy. The numbers of interfaces required for the uniform scenario are 547, 518, 499, 492, and 492 for C+L+S 10%, 20%, 40%, 60%, and 100%, respectively, whereas these values are 355, 338, 330, 326, and 326 for the population-based traffic. By Fig. 4.16a, we can see that upgrading only 10% (526 amplifiers in total) of the network spans is possible to achieve the same (population case) or lower (uniform case) number of interface levels as the C–3× scenario. Moreover, for this topology, we notice that the same interface count levels as the C+L+S 100% case are achieved when only 40% (610 amplifiers in total) of the spans receive a new AS. Fig. 4.16b presents the results for the Japanese topology for overall traffic of 229.7 (uniform case) and 203.6 Tbps (population based case). Starting with the total number of amplifiers

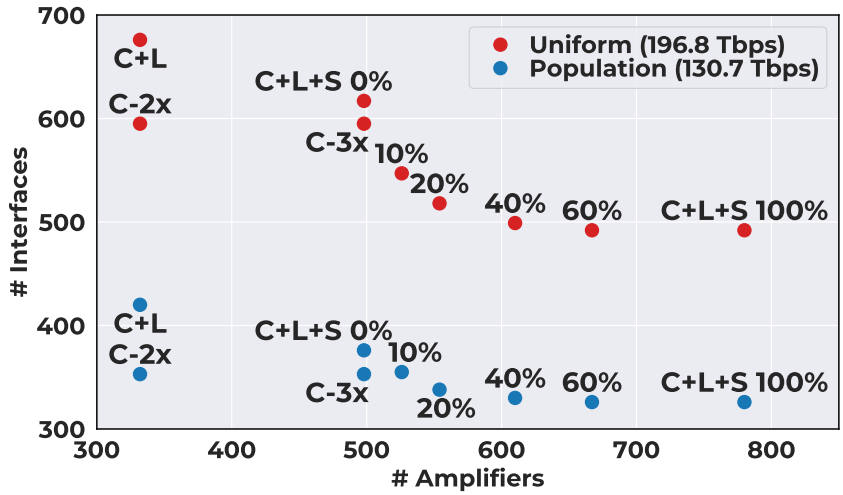

(a)

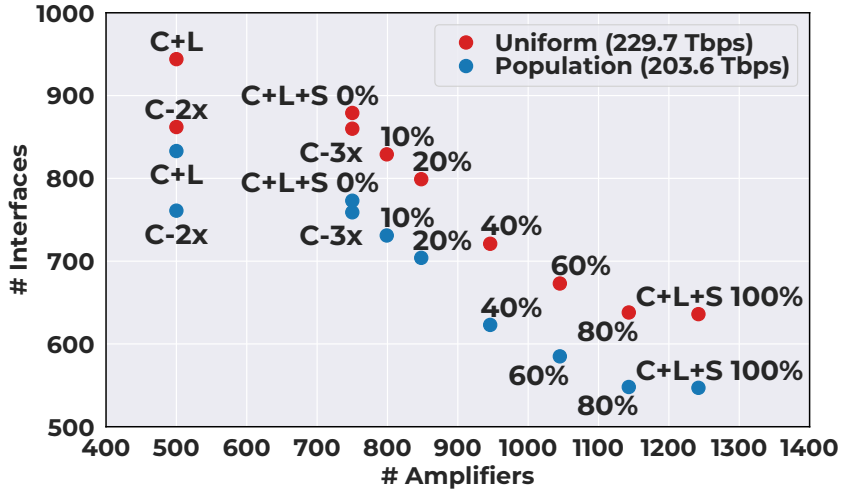

(b)

Fig. 4.16 Total number of amplifiers versus the number of used interfaces for (a) Italian for uniform and (b) Japanese topologies.

for both scenarios, the values are 500, 750, 799, 848, 946, 1045, and 1242 for C+L, C+L+S 0%, 10%, 20%, 40%, 60%, and 100%, respectively. For uniform traffic, the C+L scenario used 944 interfaces and the C–2× reduced this count to 862, whereas for the population traffic, these values are 833 and 761, both requiring 500 amplifiers in total. Using the S-band or triple the number of fibers requires a total of 750 amplifiers (250 amplifiers per band/fiber). The number of used interfaces for the C+L+S 0% are 879 and 773 for uniform and population-based cases, respectively. Similarly to the Italian topology, upgrading 10% (16 new ASs) of the network spans

overcomes the performance of the C–3× scenario. The demanded interfaces for the uniform case are 829, 799, 721, 673, and 636 and for the population-based case 731, 704, 623, 585, and 547 for C+L+S 10%, 20%, 40%, 60% and 100% scenarios, respectively. For the Japanese topology, the installation of new acpas in 60% of the network spans did not achieve the same levels of used interfaces as the C+L+S 100% case for both traffic patterns. Due to that, we added a scenario in which 80% os spans are upgraded, with a total of 1143 amplifiers and 131 new ASs. Only for that case we are able to achieve the best performance (C+L+S 100% scenario). Anyway, if we consider the decrease from C+L+S 0% to C+L+S 100% as a reference, we are able to achieve around 84% (both traffic patterns) of the maximum interface count decrease with 60% of spans being upgraded.

Chapter 5

Conclusions

This thesis starts with a brief introduction of the history of optical transmission and optical networks, from the first to the modern systems. It was also presented the traffic demand continues to increase, stressing to the limit the traffic capacity provided by todays systems. To tackle that problem, we shown the newest technologies which are the most promissory ones to provide the required capacity increasing, focusing mainly on MBT, but also discoursing about other possibilities.

In Chapter 2 three main topics were covered. Firstly, we start by describing all the details of an optical line system, showing the main components, e.g. transmitters, receivers, ROADMs, fiber and optical amplifier, presenting also how they impact the optical transmission. Secondly, we discuss about the optical network architecture, detailing about the geographic structure, the concepts of software-defined networking and disaggregation, and how we can model a transport network, considering all the physical layer impairments presented in it. We also presented the two main frameworks used in this work, GNPy and SNAP, in order to proper emulate how optical network operates. Lastly, we focus our attention in the main topic of this thesis, the multi-band transmission systems, discoursing the main differences between it and regular C-band systems, also showing the benefits an challenges.

Chapter 3 tackles the input power problem in MBT systems. We start by evaluating how consider the SRS is important in such systems and how this effect impacts the quality of transmission of the system. In Section 3.1 it is shown that MBT C+L+S transmission can decrease the QoT levels per band up to 2.4 dB, in average, per span when single band input powers are used. This QoT degradation leads to a decrease

in OLS capacity for multiple spans, achieving up to 6.4 Tbps less traffic, also comparing with single band transmission and shown in Section 3.1. Next, we present our first set of results, applying the tilt/offset strategy per band using a brute-force approach, in order to compensate the impairments raised in MBT. These first results show how important the proper power control is in MBT systems, being able to reduce the GSNR variation and improve the overall GSNR. Section 3.2.1 shows that the tilt/offset strategy for the C+L+S scenario was able to increase the S-band GSNR average by 0.6 dB and improve S-band flatness by 1.5 dB, while maintaining or improving L- and C-bands, if compared with no input power strategy. We expand our analysis to the network level, showing how the MBT can significantly improve network performance, comparable with multiple C-band systems. In Section 3.2.2 it is shown that MBT can achieve 94.8% of the delivered traffic of multiple C-band systems in the worst case. The results of this section suggest that MBT can be a viable solution for network capacity upgrade wit almost same performance as multiple C-band fibers using C-band transmission with the advantage of no new fibber deployment requirement. Finally, this chapter finishes with the application of a multi-objective genetic algorithm applied to the previously presented strategy and showed in Section 3.3. Our results show that this approach can decrease the number of simulations for a C+L+S scenario by almost half, providing equal or better OLS system performance. Specifically, the GA was able to maintain almost the same GSNR average and flatness for L-, increase the GSNR flatness by 0.9 dB in C-band, and, finally, increase the GSNR average by 0.5 dB in S-band.

In Chapter 4, we start by presenting our analysis with the usage of bismuth doped fiber amplifier in E-band, in order to upgrade a C+L optical system. In Section 4.1, our modelling results shown that the usage this type of amplifier presents a acceptable performance, even with higher penalties presented by this band. Accordingly to our results, an OLS of eight spans of 80 km still has enough QoT (12.7 dB) in E-band to transmit using low order modulation formats of flexible transceivers. Moreover, we show that adding this band presents a almost insignificant impact on C+L systems, presenting an increasing in GSNR variation up to 0.4 dB. The second part of this chapter, shown in Section 4.2, presents the analysis carried to evaluate two possible MBT upgrade scenarios: add the S- or the E-band to a C+L system already in use. Bringing this analysis also to the network level, our results show that the E-band upgrade does not require any LP reconfiguration, and if high margins are required, E-band upgrade provides a better performance. This chapter finishes by showing the

latest results of our work, a MBT network design presented in Section 4.3, in which limited number of additional amplification site are distributed withing the network, in order to increase the overall system performance, as well as being able to reduce the number of used transceivers. We performed a network assessment for a couple of physical topologies and two traffic patterns, showing the benefits of deploying new ASs, if is required a better performance of these MBT networks. We shown that up to 40% of te network spans receiving a new AS is able to deliver the same traffic performance as a network with multiple fibers using C-band systems. Moreover, it is presented that with already 10% of new AS is possible to reduce the number of used interfaces for a fixed traffic, also compare with C-band systems.

References

[1] Bruno Correia, Rasoul Sadeghi, Emanuele Virgillito, Antonio Napoli, Nelson Costa, João Pedro, and Vittorio Curri. Power control strategies and network performance assessment for C+L+S multiband optical transport. *Journal of Optical Communications and Networking*, 13(7):147, jul 2021.

[2] Nicola Sambo, Bruno Correia, Antonio Napoli, João Pedro, Leily Kiani, Piero Castoldi, and Vittorio Curri. Network upgrade exploiting multi band: S- or E-band? *Journal of Optical Communications and Networking*, 14(9):749, sep 2022.

[3] Andrea D'Amico, Bruno Correia, Elliot London, Emanuele Virgillito, Giacomo Borraccini, Antonio Napoli, and Vittorio Curri. Scalable and Disaggregated GGN Approximation Applied to a C+L+S Optical Network. *Journal of Lightwave Technology*, 40(11):3499–3511, jun 2022.

[4] Rasoul Sadeghi, Bruno Correia, Andre Souza, Nelson Costa, Joao Pedro, Antonio Napoli, and Vittorio Curri. Transparent vs Translucent Multi-Band Optical Networking: Capacity and Energy Analyses. *Journal of Lightwave Technology*, 40(11):3486–3498, 2022.

[5] Matheus Sena, Pratim Hazarika, Caio Santos, Bruno Correia, Robert Emmerich, Behnam Shariati, Antonio Napoli, Vittorio Curri, Wladek Forysiak, Colja Schubert, Johannes K. Fischer, and Ronald Freund. Advanced DSP-Based Monitoring for Spatially Resolved and Wavelength-Dependent Amplifier Gain Estimation and Fault Location in C+L-Band Systems. *Journal of Lightwave Technology*, 41(3):989–998, feb 2023.

[6] Emanuele Virgillito, Rasoul Sadeghi, Alessio Ferrari, Antonio Napoli, Bruno Correia, and Vittorio Curri. Network Performance Assessment with Uniform and Non-Uniform Nodes Distribution in C+L Upgrades vs. Fiber Doubling SDM Solutions. In *2020 International Conference on Optical Network Design and Modeling (ONDM)*, pages 1–6. IEEE, may 2020.

[7] Bruno Correia, Rasoul Sadeghi, Emanuele Virgillito, Antonio Napoli, Nelson Costa, Joao Pedro, and Vittorio Curri. Networking Performance of Power Optimized C+L+S Multiband Transmission. In *GLOBECOM 2020 - 2020 IEEE Global Communications Conference*, pages 1–6. IEEE, dec 2020.

[8] Rasoul Sadeghi, Bruno Correia, Emanuele Virgillito, Nelson Costa, Joao Pedro, Antonio Napoli, and Vittorio Curri. Multi Bands Network Performance Assessment for Different System Upgrades. In *2020 IEEE Photonics Conference (IPC)*, pages 1–2. IEEE, sep 2020.

[9] Bruno Correia, Rasoul Sadeghi, Emanuele Virgillito, Antonio Napoli, and Vittorio Curri. Optical Power Control Strategies for Optimized C + L + S-bands Network Performance. In *Optical Fiber Communication Conference (OFC) 2021*, page W1F.8, 2021.

[10] Rasoul Sadeghi, Bruno Correia, Emanuele Virgillito, Antonio Napoli, João Pedro, and Vittorio Curri. Performance Comparison of Translucent C-band and Transparent C + L-band Network. In *Optical Fiber Communication Conference (OFC) 2021*, volume 1, page M3E.4, 2021.

[11] Emanuele Virgillito, Elliot London, Andrea D Amico, Bruno Correia, Antonio Napoli, and Vittorio Curri. Single- vs . Multi-Band Optimized Power Control in C + L WDM 400G Line Systems. In *Optical Fiber Communication Conference (OFC) 2021*, page Th4C.3. OSA, 2021.

[12] Rasoul Sadeghi, Bruno Correia, Emanuele Virgillito, Antonio Napoli, Nelson Costa, Joao Pedro, and Vittorio Curri. Comparison of Transceiver and C+L Band Upgrades: Network Traffic and Energy Assessment. In *2021 International Conference on Electrical, Communication, and Computer Engineering (ICECCE)*, pages 1–6. IEEE, jun 2021.

[13] Rasoul Sadeghi, Bruno Correia, Emanuele Virgillito, Antonio Napoli, Nelson Costa, Joao Pedro, and Vittorio Curri. Network Comparison of C+L-band Transparent versus C-band Translucent Upgrade. In *2021 International Conference on Optical Network Design and Modeling (ONDM)*, pages 1–6. IEEE, jun 2021.

[14] Bruno Correia, Rasoul Sadeghi, Emanuele Virgillito, Antonio Napoli, Nelson Costa, Joao Pedro, and Vittorio Curri. Multiband Power Control Impact on the Transmission Capacity of Optical Line Systems. In *2021 IEEE Photonics Society Summer Topicals Meeting Series (SUM)*, pages 1–2. IEEE, jul 2021.

[15] Rasoul Sadeghi, Bruno Correia, Emanuele Virgillito, Antonio Napoli, Nelson Costa, Joao Pedro, and Vittorio Curri. C+L-band Network Upgrade: Capacity and Energy Analyses with Different Transceivers. In *2021 IEEE Photonics Society Summer Topicals Meeting Series (SUM)*, pages 1–2. IEEE, jul 2021.

[16] Rasoul Sadeghi, Bruno Correia, Emanuele Virgilito, Elliot London, Nelson Costa, Joao Pedro, Antonio Napoli, and Vittorio Curri. Optimized Translucent S-band Transmission in Multi-Band Optical Networks. In *2021 European Conference on Optical Communication (ECOC)*, pages 1–4. IEEE, sep 2021.

[17] Rasoul Sadeghi, Bruno Correia, Emanuele Virgillito, Antonio Napoli, Nelson Costa, Joao Pedro, and Vittorio Curri. Cost-Effective Capacity Increase of

Deployed Optical Networks to Support the Future Internet: the Multi-Band Approach. In *2021 12th International Conference on Network of the Future (NoF)*, pages 1–7. IEEE, oct 2021.

[18] Rasoul Sadeghi, Bruno Correia, Emanuele Virgillito, Antonio Napoli, Nelson Costa, Joao Pedro, and Vittorio Curri. Network Capacity and Energy Consumption: Transparent C + L -band vs Translucent C-band. In *2021 IEEE Photonics Conference (IPC)*, pages 1–2. IEEE, oct 2021.

[19] B. Correia, A. Donodin, R. Sadeghi, V. Dvoyrin, V. Dvoyrin, A. Napoli, J. Pedro, J. Pedro, N. Costa, W. Forysiak, S. K. Turitsyn, S. K. Turitsyn, and V. Curri. QoT Evaluation of Optical Line System Transmission with Bismuth-Doped Fiber Amplifiers in the E-Band. In *Asia Communications and Photonics Conference 2021 (2021)*, page M4I.5. Optica Publishing Group, oct 2021.

[20] Andre Souza, Bruno Correia, Nelson Costa, Joao Pedro, and Joao Pires. Accurate and Scalable Quality of Transmission Estimation for Wideband Optical Systems. In *2021 IEEE 26th International Workshop on Computer Aided Modeling and Design of Communication Links and Networks (CAMAD)*, volume 2021-Octob, pages 1–6. IEEE, oct 2021.

[21] Rasoul Sadeghi, Bruno Correia, Emanuele Virgillito, Antonio Napoli, Nelson Costa, João Pedro, and Vittorio Curri. Optimal Spectral Usage and Energy Efficient S-to-U Multiband Optical Networking. In *Optical Fiber Communication Conference (OFC) 2022*, page W3F.7, Washington, D.C., mar 2022. Optica Publishing Group.

[22] Nicola Sambo, Bruno Correia, Antonio Napoli, João Pedro, Piero Castoldi, and Vittorio Curri. Transport Network Upgrade exploiting Multi-Band Systems: S- versus E-band. In *Optical Fiber Communication Conference (OFC)*, page W3F.8. Optica Publishing Group, mar 2022.

[23] André Souza, Rasoul Sadeghi, Bruno Correia, Nelson Costa, Antonio Napoli, Vittorio Curri, João Pedro, and João Pires. Optimal Pay-As-You-Grow Deployment on S+C+L Multi-band Systems. In *Optical Fiber Communication Conference (OFC) 2022*, page W3F.4, Washington, D.C., mar 2022. Optica Publishing Group.

[24] Rasoul Sadeghi, Bruno Correia, Andre Souza, Antonio Napoli, Nelson Costa, Joao Pedro, and Vittorio Curri. Capacity and Energy Consumption Comparison in Translucent versus Transparent Multi-band Designs. In *2022 International Conference on Optical Network Design and Modeling, ONDM 2022*, pages 1–3. IEEE, may 2022.

[25] Rasoul Sadeghi, Bruno Correia, Antonio Napoli, Nelson Costa, João Pedro, and Vittorio Curri. Capacity and Energy Usage of Translucent and Multi-Band Transparent Optical Networks. In *Optica Advanced Photonics Congress 2022*, page NeTu3D.2, Washington, D.C., jul 2022. Optica Publishing Group.

[26] Rasoul Sadeghi, Bruno Correia, Nelson Costa, João Pedro, João Pedro, Antonio Napoli, and Vittorio Curri. Extending the C+L System Bandwidth versus Exploiting Part of the S-band: Network Capacity and Interface Count Comparison. In *European Conference on Optical Communication (ECOC) 2022*, page We1B.2. Optica Publishing Group, sep 2022.

[27] Muhammad Umar Masood, Ihtesham Khan, Lorenzo Tunesi, Bruno Correia, Rasoul Sadeghi, Enrico Ghillino, Paolo Bardella, Andrea Carena, and Vittorio Curri. Networking Analysis of Photonics Integrated Multiband WSS Based ROADM Architecture. In *2022 International Conference on Software, Telecommunications and Computer Networks (SoftCOM)*, pages 1–6. IEEE, sep 2022.

[28] Muhammad Umar Masood, Lorenzo Tunesi, Bruno Correia, Ihtesham Khan, Enrico Ghillino, Paolo Bardella, Andrea Carena, and Vittorio Curri. Photonics Integrated Multiband WSS Based ROADM Architecture: A Networking Analysis. In *2022 Asia Communications and Photonics Conference (ACP)*, pages 1243–1247. IEEE, nov 2022.

[29] Muhammad Umar Masood, Ihtesham Khan, Lorenzo Tunesi, Bruno Correia, Enrico Ghillino, Paolo Bardella, Andrea Carena, and Vittorio Curri. Network Traffic Analysis of Modular Multiband Integrated WSS based ROADMs. In *IEEE Photonics Conference, IPC 2022*. Institute of Electrical and Electronics Engineers Inc., 2022.

[30] Muhammad Umar Masood, Ihtesham Khan, Lorenzo Tunesi, Bruno Correia, Enrico Ghillino, Paolo Bardella, Andrea Carena, and Vittorio Curri. Network Performance of ROADM Architecture Enabled by Novel Wideband-integrated WSS. In *GLOBECOM 2022 - 2022 IEEE Global Communications Conference*, pages 2945–2950. IEEE, dec 2022.

[31] Muhammad Umar Masood, Lorenzo Tunesi, Ihtesham Khan, Bruno Correia, Enrico Ghillino, Paolo Bardella, Andrea Carena, and Vittorio Curri. Network performance analysis of a PIC-based reconfigurable add-drop multiplexer for multiband applications. In *Next-Generation Optical Communication: Components, Sub-Systems, and Systems XII*, volume 12429, pages 81–86, San Francisco, California, mar 2023. SPIE.

[32] Bruno Correia, Rasoul Sadeghi, Antonio Napoli, Nelson Costa, João Pedro, and Vittorio Curri. C+L+S-Band Optical Network Design Exploiting Amplifier Site Upgrade Strategies | IEEE Conference Publication | IEEE Xplore. In *2023 International Conference on Optical Network Design and Modeling (ONDM)*, pages 1–6, Coimbra, 2023.

[33] Rasoul Sadeghi, Bruno Correia, Elliot London, Antonio Napoli, Nelson Costa, João Pedro, and Vittorio Curri. Performance comparison of optical networks exploiting multiple and extended bands and leveraging reinforcement learning. In *2023 International Conference on Optical Network Design and Modeling (ONDM)*, pages 1–6, 2023.

[34] Govind P. Agrawal. *Fiber-Optic Communication Systems*. Wiley, oct 2010.

[35] A. L. Schawlow and C. H. Townes. Infrared and Optical Masers. *Physical Review*, 112(6):1940–1949, dec 1958.

[36] T. Miya, Y. Terunuma, T. Hosaka, and T. Miyashita. Ultimate low-loss single-mode fibre at 1.55 μm. *Electronics Letters*, 15(4):106, feb 1979.

[37] ITU-T. *Optical fibres, cables and systems*. ITU-T, 2009.

[38] Rajiv Ramaswami, Kumar N. Sivarajan, and Galen H. Sasaki. *Optical Networks: A Practical Perspective*. Elsevier, jan 2009.

[39] Erik Agrell, Magnus Karlsson, A. R. Chraplyvy, David J. Richardson, Peter M. Krummrich, Peter Winzer, Kim Roberts, Johannes Karl Fischer, Seb J. Savory, Benjamin J. Eggleton, Marco Secondini, Frank R. Kschischang, Andrew Lord, Josep Prat, Ioannis Tomkos, John E. Bowers, Sudha Srinivasan, Maïté Brandt-Pearce, and Nicolas Gisin. Roadmap of optical communications. *Journal of Optics*, 18(6):063002, may 2016.

[40] Xiang Liu. Evolution of Fiber-Optic Transmission and Networking toward the 5G Era. *iScience*, 22:489–506, dec 2019.

[41] David T. Neilson, Andrew R. Chraplyvy, and Peter J. Winzer. Fiber-optic transmission and networking: the previous 20 and the next 20 years [Invited]. *Optics Express*, 26(18):24190–24239, sep 2018.

[42] Cisco Annual Internet Report - Cisco Annual Internet Report (2018–2023) White Paper - Cisco.

[43] KwangOk Kim, Kyeong-Hwan Doo, Han Hyub Lee, SeungHwan Kim, Heuk Park, Jung-Yeol Oh, and Hwan Seok Chung. High Speed and Low Latency Passive Optical Network for 5G Wireless Systems. *Journal of Lightwave Technology*, 37(12):2873–2882, jun 2019.

[44] Chuang Song, Min Zhang, Yueying Zhan, Danshi Wang, Luyao Guan, Wei Liu, Lin Zhang, and Siya Xu. Hierarchical Edge Cloud Enabling Network Slicing for 5G Optical Fronthaul. *Journal of Optical Communications and Networking*, 11(4):B60, apr 2019.

[45] Jun Li, Lei Chen, and Jiajia Chen. Enabling technologies for low-latency service migration in 5G transport networks [Invited]. *Journal of Optical Communications and Networking*, 13(2):A200, feb 2021.

[46] Chongjin Xie, Lei Wang, Liang Dou, Ming Xia, Sai Chen, Huan Zhang, Zhao Sun, and Jingchi Cheng. Open and disaggregated optical transport networks for data center interconnects [Invited]. *Journal of Optical Communications and Networking*, 12(6):C12–C22, jun 2020.

[47] Fred Buchali, Fabian Steiner, Georg Bocherer, Laurent Schmalen, Patrick Schulte, and Wilfried Idler. Rate Adaptation and Reach Increase by Probabilistically Shaped 64-QAM: An Experimental Demonstration. *Journal of Lightwave Technology*, 34(7):1599–1609, apr 2016.

[48] Junho Cho, Xi Chen, Sethumadhavan Chandrasekhar, Gregory Raybon, Ronen Dar, Laurent Schmalen, Ells Burrows, Andrew Adamiecki, Steve Corteselli, Yan Pan, DIego Correa, Brad McKay, Szilard Zsigmond, Peter J. Winzer, and Steve Grubb. Trans-Atlantic Field Trial Using High Spectral Efficiency Probabilistically Shaped 64-QAM and Single-Carrier Real-Time 250-Gb/s 16-QAM. *Journal of Lightwave Technology*, 36(1):103–113, jan 2018.

[49] Dimitris Uzunidis, Michael Logothetis, Alexandros Stavdas, David Hillerkuss, and Ioannis Tomkos. Fifty Years of Fixed Optical Networks Evolution: A Survey of Architectural and Technological Developments in a Layered Approach. *Telecom*, 3(4):619–674, nov 2022.

[50] ICE6 800G Generation Optical Engine.

[51] George M. Saridis, Dimitris Alexandropoulos, Georgios Zervas, and Dimitra Simeonidou. Survey and Evaluation of Space Division Multiplexing: From Technologies to Optical Networks. *IEEE Communications Surveys & Tutorials*, 17(4):2136–2156, 2015.

[52] Werner Klaus, Benjamin J. Puttnam, Ruben S. Luís, Jun Sakaguchi, José-Manuel Delgado Mendinueta, Yoshinari Awaji, and Naoya Wada. Advanced Space Division Multiplexing Technologies for Optical Networks. *Journal of Optical Communications and Networking*, 9(4):C1, apr 2017.

[53] Yusuke Sasaki, Ryohei Fukumoto, Katsuhiro Takenaga, Shogo Shimizu, and Kazuhiko Aikawa. Optical-Fiber Cable Employing 200-μm-Coated Four-Core Multicore Fibers. *Journal of Lightwave Technology*, 40(5):1560–1566, mar 2022.

[54] Hitoshi Takeshita, Kohei Nakamura, Yuushi Matsuo, Takanori Inoue, Daishi Masuda, Tetsuya Hiwatashi, Kohei Hosokawa, Yoshihisa Inada, and Emmanuel Le Taillandier De Gabory. Demonstration of Uncoupled 4-Core Multicore Fiber in Submarine Cable Prototype with Integrated Multicore EDFA. *Journal of Lightwave Technology*, 41(3):980–988, feb 2023.

[55] Antonio Napoli, Nelson Costa, Johannes K. Fischer, João Pedro, Silvio Abrate, Nicola Calabretta, Wladek Forysiak, Erwan Pincemin, Juan P.F.P. Gimenez, Chris Matrakidis, Gunther Roelkens, and Vittorio Curri. Towards multiband optical systems. In *Advanced Photonics 2018 (BGPP, IPR, NP, NOMA, Sensors, Networks, SPPCom, SOF)*, volume Part F106-, page NeTu3E.1, Washington, D.C., 2018. OSA.

[56] Mattia Cantono, Rene Schmogrow, Matt Newland, Vijay Vusirikala, and Tad Hofmeister. Opportunities and Challenges of C+L Transmission Systems. *Journal of Lightwave Technology*, 38(5):1050–1060, 2020.

[57] Vittorio Curri. GNPy model of the physical layer for open and disaggregated optical networking [Invited]. *Journal of Optical Communications and Networking*, 14(6):C92, jun 2022.

[58] Wenfeng Xia, Yonggang Wen, Chuan Heng Foh, Dusit Niyato, and Haiyong Xie. A Survey on Software-Defined Networking. *IEEE Communications Surveys and Tutorials*, 17(1):27–51, jan 2015.

[59] Han Sun, Kuang-Tsan Wu, and Kim Roberts. Real-time measurements of a 40 Gb/s coherent system. *Optics Express*, 16(2):873–879, jan 2008.

[60] Michael G. Taylor. Coherent Detection Method Using DSP for Demodulation of Signal and Subsequent Equalization of Propagation Impairments. *IEEE Photonics Technology Letters*, 16(2):674–676, feb 2004.

[61] Stephen S. Walker. Rapid Modeling and Estimation of Total Spectral Loss in Optical Fibers. *Journal of Lightwave Technology*, 4(8):1125–1131, 1986.

[62] Govind Agrawal. *Nonlinear Fiber Optics*. Elsevier, jan 2012.

[63] G.J. Foschini and C.D. Poole. Statistical theory of polarization dispersion in single mode fibers. *Journal of Lightwave Technology*, 9(11):1439–1456, 1991.

[64] Antonio Mecozzi and Mark Shtaif. The statistics of polarization-dependent loss in optical communication systems. *IEEE Photonics Technology Letters*, 14(3):313–315, mar 2002.

[65] A. El Amari, Nicolas Gisin, Beat Perny, H. Zbinden, and Christian W. Zimmer. Statistical prediction and experimental verification of concatenations of fiber optic components with polarization dependent loss. *Journal of Lightwave Technology*, 16(3):332–339, mar 1998.

[66] Erwan Pincemin, Didier Grot, Laurence Bathany, Stéphane Gosselin, Michel Joindot, Sylvain Bordais, Yves Jaouen, and Jean Marc Delavaux. Raman gain efficiencies of modern terrestrial transmission fibers in S-, C- and L-band. *Nonlinear Guided Waves and Their Applications*, page NLTuC2, sep 2002.

[67] Clifford Headley and Govind P. Agrawal. *Raman Amplification in Fiber Optical Communication Systems*. Elsevier, jan 2004.

[68] Jake Bromage. Raman Amplification for Fiber Communications Systems. *Journal of Lightwave Technology*, 22(1):79–93, jan 2004.

[69] R. H. Stolen and A. Ashkin. Optical Kerr effect in glass waveguide. *Applied Physics Letters*, 22(6):294–296, mar 1973.

[70] D. F. PARKER and G. K. NEWBOULT. COUPLED NONLINEAR SCHRÖDINGER EQUATIONS ARISING IN FIBRE OPTICS. *Le Journal de Physique Colloques*, 50(C3):C3–137, mar 1989.

[71] Dietrich Marcuse, C. R. Menyuk, and P. K.A. Wai. Application of the Manakov-PMD equation to studies of signal propagation in optical fibers with randomly varying birefringence. *Journal of Lightwave Technology*, 15(9):1735–1745, sep 1997.

[72] Andrea Carena, Gabriella Bosco, Vittorio Curri, Yanchao Jiang, Pierluigi Poggiolini, and Fabrizio Forghieri. EGN model of non-linear fiber propagation. *Optics Express*, 22(13):16335, jun 2014.

[73] Emanuele Virgillito, Andrea D'Amico, Alessio Ferrari, and Vittorio Curri. Observing and modeling wideband generation of non-linear interference. *International Conference on Transparent Optical Networks (ICTON)*, 2019-July, jul 2019.

[74] Pontus Johannisson and Magnus Karlsson. Perturbation analysis of nonlinear propagation in a strongly dispersive optical communication system. *Journal of Lightwave Technology*, 31(8):1273–1282, 2013.

[75] P. Poggiolini and Y. Jiang. Recent Advances in the Modeling of the Impact of Nonlinear Fiber Propagation Effects on Uncompensated Coherent Transmission Systems. *Journal of Lightwave Technology*, 35(3):458–480, feb 2017.

[76] Vittorio Curri, Andrea Carena, Pierluigi Poggiolini, Gabriella Bosco, Fabrizio Forghieri, K Roberts, W Kuang-Tsan, H Sun, A Awadalla, D J Krause, and C Laperle. Extension and validation of the GN model for non-linear interference to uncompensated links using Raman amplification. *Optics Express*, 21(3):3308–3317, feb 2013.

[77] P. Serena and A. Bononi. On the accuracy of the Gaussian nonlinear model for dispersion-unmanaged coherent links. *IET Conference Publications*, 2013(622 CP):723–725, 2013.

[78] Andrea D'Amico, Elliot London, Bertrand Le Guyader, Florian Frank, Esther Le Rouzic, Erwan Pincemin, Nicolas Brochier, and Vittorio Curri. Experimental validation of GNPy in a multi-vendor flex-grid flex-rate WDM optical transport scenario. *Journal of Optical Communications and Networking*, 14(3):79–88, mar 2022.

[79] Antonino Nespola, Stefano Straullu, Andrea Carena, Gabriella Bosco, Roberto Cigliutti, Vittorio Curri, Pierluigi Poggiolini, Masaaki Hirano, Yoshinori Yamamoto, Takashi Sasaki, Johan Bauwelinck, Koen Verheyen, and Fabrizio Forghieri. GN-Model Validation Over Seven Fiber Types in Uncompensated PM-16QAM Nyquist-WDM Links. *IEEE Photonics Technology Letters*, 26(2):206–209, jan 2014.

[80] A. Nespola, S. Straullu, A. Carena, G. Bosco, R. Cigliutti, V. Curri, P. Poggiolini, M. Hirano, Y. Yamamoto, T. Sasaki, J. Bauwelinck, K. Verheyen, and F. Forghieri. Extensive Fiber Comparison and GN-model Validation in

Uncompensated Links using DAC-generated Nyquist-WDM PM-16QAM Channels. *Optical Fiber Communication Conference/National Fiber Optic Engineers Conference*, page OTh3G.5, mar 2013.

[81] Mattia Cantono, Dario Pilori, Alessio Ferrari, Clara Catanese, Jordane Thouras, Jean-Luc Auge, and Vittorio Curri. On the Interplay of Nonlinear Interference Generation With Stimulated Raman Scattering for QoT Estimation. *Journal of Lightwave Technology*, 36(15):3131–3141, aug 2018.

[82] Mattia Cantono, Jean Luc Auge, and Vittorio Curri. Modelling the impact of SRS on NLI generation in commercial equipment: An experimental investigation. In *2018 Optical Fiber Communications Conference and Exposition, OFC 2018 - Proceedings*, pages 1–3. OSA, 2018.

[83] Andrea D'Amico, Vittorio Curri, Antonio Napoli, Elliot London, and Emanuele Virgillito. Modelling non-linear interference in non-periodic and disaggregated optical network segments. *Optics Continuum*, 1(4):793–803, apr 2022.

[84] Marco Secondini and Enrico Forestieri. Analytical fiber-optic channel model in the presence of cross-phase modulation. *IEEE Photonics Technology Letters*, 24(22):2016–2019, 2012.

[85] Ronen Dar, Meir Feder, Antonio Mecozzi, and Mark Shtaif. Pulse collision picture of inter-channel nonlinear interference in fiber-optic communications. *Journal of Lightwave Technology*, 34(2):593–607, 2016.

[86] Michael J. Connelly. *Semiconductor Optical Amplifiers*. Kluwer Academic Publishers, Boston, 2004.

[87] Shoichi Sudo. *Optical fiber amplifiers : materials, devices, and applications*. Artech House, 1997.

[88] Jane M. Simmons. *Optical Network Design and Planning*. Optical Networks. Springer International Publishing, Cham, 2014.

[89] Leonid G. Kazovsky, Ning Cheng, Wei-Tao Shaw, Shing-Wa Wong, and David Gutierrez. Next-Generation Optical Access Networks. *Journal of Lightwave Technology*, 25(11):3428–3442, nov 2007.

[90] Derek Nesset. Next Generation PON Technologies: 50G PON and Beyond (Invited) | IEEE Conference Publication | IEEE Xplore. In *2023 International Conference on Optical Network Design and Modeling (ONDM)*, 2023.

[91] Glen Kramer and Gerry Pesavento. Ethernet passive optical network (EPON): Building a next-generation optical access network. *IEEE Communications Magazine*, 40(2):66–73, 2002.

[92] Software-Defined Networking: The New Norm for Networks - Open Networking Foundation.

[93] Mohammad Mousa, Ayman M. Bahaa-ElDin, and Mohamed Sobh. Software Defined Networking concepts and challenges. *11th International Conference on Computer Engineering and Systems, ICCES*, pages 79–90, jan 2017.

[94] Esther Le Rouzic, Olivier Augizeau, Olivier Renais, Julien Meuric, Thierry Marcot, Christophe Betoule, Gilles Thouenon, Ahmed Triki, Maxime Laye, Nicolas Pelloquin, Yannick Lagadec, and Emmanuelle Delfour. Automation Journey in Core and Metro Networks: An Operator View. *2021 European Conference on Optical Communication, ECOC 2021*, 2021.

[95] Alessio Ferrari, Mark Filer, Karthikeyan Balasubramanian, Yawei Yin, Esther Le Rouzic, Jan Kundrát, Gert Grammel, Gabriele Galimberti, and Vittorio Curri. GNPy: an open source application for physical layer aware open optical networks. *Journal of Optical Communications and Networking*, 12(6):C31, jun 2020.

[96] Mark Filer, Mattia Cantono, Alessio Ferrari, Gert Grammel, Gabriele Galimberti, and Vittorio Curri. Multi-Vendor Experimental Validation of an Open Source QoT Estimator for Optical Networks. *Journal of Lightwave Technology*, 36(15):3073–3082, aug 2018.

[97] Alessio Ferrari, Mark Filer, Esther Le Rouzic, Jan Kundrat, Bruno Correia, Karthikeyan Balasubramanian, Yawei Yin, Gert Grammel, Gabriele Galimberti, and Vittorio Curri. GNPy: an open source planning tool for open optical networks. In *2020 International Conference on Optical Network Design and Modeling (ONDM)*, number 1, pages 1–6. IEEE, may 2020.

[98] GitHub - Telecominfraproject/oopt-gnpy: Optical Route Planning Library, Based on a Gaussian Noise Model.

[99] Vittorio Curri, Mattia Cantono, and Roberto Gaudino. Elastic All-Optical Networks: A New Paradigm Enabled by the Physical Layer. How to Optimize Network Performances? *Journal of Lightwave Technology*, 35(6):1211–1221, mar 2017.

[100] Krzysztof Walkowiak, Mirosław Klinkowski, and Piotr Lechowicz. Dynamic Routing in Spectrally Spatially Flexible Optical Networks with Back-to-Back Regeneration. *Journal of Optical Communications and Networking*, 10(5):523, may 2018.

[101] Krzysztof Walkowiak, Piotr Lechowicz, and Miroslaw Klinkowski. Transceiver Sharing in Survivable Spectrally-Spatially Flexible Optical Networks. *2018 IEEE Global Communications Conference, GLOBECOM 2018 - Proceedings*, pages 0–5, 2019.

[102] E. W. Dijkstra. A note on two problems in connexion with graphs. *Numerische Mathematik*, 1(1):269–271, dec 1959.

[103] Jin Y. Yen. Finding the K Shortest Loopless Paths in a Network. *Management Science*, 17(11):712–716, jul 1971.

[104] H. Zang, J. P. Jue, and B. Mukherjee. A review of Routing and Wavelength Assignment Approaches for Wavelength- Routed Optical WDM Networks. *Optical Networks Magazine*, 1(January):47–60, 2000.

[105] Joao Pedro and Silvia Pato. On scaling transport networks for very high nodal degree ROADM nodes using state-of-the-art optical switch technology. *International Conference on Transparent Optical Networks*, 2015-Augus, aug 2015.

[106] Joao Pedro and Silvia Pato. ROADM express layer design strategies for scalable and cost-effective multi-fibre DWDM networks. *International Conference on Transparent Optical Networks*, sep 2017.

[107] Kiyoshi Fukuchi, Tadashi Kasamatsu, Masao Morie, Risato Ohhira, Toshiharu Ito, Kayato Sekiya, Daisaku Ogasahara, and Takashi Ono. 10.92-Tb/s (273 $\times$ 40-Gb/s) triple-band/ultra-dense WDM optical-repeatered transmission experiment. *Optical Fiber Communication Conference and International Conference on Quantum Information (2001)*, page PD24, mar 2001.

[108] Seiji Okamoto, Kengo Horikoshi, Fukutaro Hamaoka, Kyo Minoguchi, and Akira Hirano. 5-band (O , E , S , C , and L) WDM Transmission with Wavelength Adaptive Modulation Format Allocation. In *European Conference on Optical Communication (ECOC) 2016*, pages 20–22, 2016.

[109] Benjamin J. Puttnam, Ruben S. Luís, Georg Rademacher, Manuel Mendez-Astudilio, Yoshinari Awaji, and Hideaki Furukawa. S, C and Extended L-Band Transmission with Doped Fiber and Distributed Raman Amplification. *Optical Fiber Communication Conference (OFC)*, page Th4C.2, jun 2021.

[110] Lidia Galdino, Adrian Edwards, Wenting Yi, Eric Sillekens, Yuta Wakayama, Thomas Gerard, Wayne Sheldon Pelouch, Stuart Barnes, Takehiro Tsuritani, Robert I. Killey, Domanic Lavery, and Polina Bayvel. Optical Fibre Capacity Optimisation via Continuous Bandwidth Amplification and Geometric Shaping. *IEEE Photonics Technology Letters*, 32(17):1021–1024, sep 2020.

[111] A. Turukhin, O. V. Sinkin, H. G. Batshon, M. Mazurczyk, W. W. Patterson, G. Wolter, M. A. Bolshtyansky, D. G. Foursa, and A. Pilipetskii. Power-Efficient Transmission Using Optimized C+L EDFAs with 6.46 THz Bandwidth and Optimal Spectral Efficiency. *European Conference on Optical Communication, ECOC*, 2018-Septe:12–14, 2018.

[112] Meeting the 4 Challenges of C+L. https://www.infinera.com/blog/meeting-the-4-challenges-of-cl/tag/long-haul/?utm_source=SHP&utm_medium=Blog&utm_campaign=CLChallenges.

[113] Johannes K. Fischer, Mattia Cantono, Vittorio Curri, Ralf-Peter Braun, Nelson Costa, Joao Pedro, Erwan Pincemin, Philippe Doare, Claude Le Bouette, and Antonio Napoli. Maximizing the Capacity of Installed Optical Fiber Infrastructure Via Wideband Transmission. In *2018 20th International Conference*

on Transparent Optical Networks (ICTON), volume 2018-July, pages 1–4. IEEE, jul 2018.

[114] Alessio Ferrari, Antonio Napoli, Johannes K. Fischer, Nelson Costa, Joao Pedro, Nicola Sambo, Erwan Pincemin, Bernd Sommerkohrn-Krombholz, and Vittorio Curri. Upgrade capacity scenarios enabled by multi-band optical systems. *International Conference on Transparent Optical Networks*, 2019-July:3–6, 2019.

[115] Karsten Rottwitt, Lufeng Leng, Jake Bromage, Malcolm E. Lines, Henrik Smith, and Andrew J. Stentz. Scaling of the Raman Gain Coefficient: Applications to Germanosilicate Fibers. *Journal of Lightwave Technology*, 21(7):1652–, jul 2003.

[116] Takeshi Hoshida, Vittorio Curri, Lidia Galdino, David T. Neilson, Wladek Forysiak, Johannes K. Fischer, Tomoyuki Kato, and Pierluigi Poggiolini. Ultrawideband Systems and Networks: Beyond $C+L$-Band. *Proceedings of the IEEE*, pages 1–17, 2022.

[117] Robert Emmerich, Matheus Sena, Robert Elschner, Carsten Schmidt-Langhorst, Isaac Sackey, Colja Schubert, and Ronald Freund. Enabling S-C-L-band systems with standard c-band modulator and coherent receiver using coherent system identification and nonlinear predistortion. *Journal of Lightwave Technology*, 40(5):1360–1368, 2022.

[118] Gabriele Di Rosa, Robert Emmerich, Matheus Sena, Johannes K. Fischer, Colja Schubert, and Andre Richter. Impact of Wavelength-Dependent I/Q Imbalances of Standard C-Band Transceivers in Rate-Adaptive Multiband Systems. *2021 European Conference on Optical Communication, ECOC 2021*, (1):32–35, 2021.

[119] Gabriele Di Rosa, Robert Emmerich, Matheus Sena, Johannes K. Fischer, Colja Schubert, Ronald Freund, and Andre Richter. Characterization, Monitoring, and Mitigation of the I/Q Imbalance in Standard C-Band Transceivers in Multi-Band Systems. *Journal of Lightwave Technology*, 40(11):3470–3478, jun 2022.

[120] Finisar WSS: Flexgrid(R) C+L Wavelength Selective Switch | Lightwave.

[121] Nicolas K. Fontaine, Mikael Mazur, Roland Ryf, Haoshuo Chen, Lauren Dallachiesa, and David T. Neilson. 36-THz Bandwidth Wavelength Selective Switch. *2021 European Conference on Optical Communication (ECOC)*, 2021.

[122] Xiang Liu. Enabling Optical Network Technologies for 5G and Beyond. *Journal of Lightwave Technology*, 40(2):358–367, jan 2022.

[123] Lutz Rapp and Michael Eiselt. Optical Amplifiers for Wideband Optical Transmission Systems. *Optical Fiber Communication Conference (OFC)*, page Th4C.1, jun 2021.

[124] Lutz Rapp and Michael Eiselt. Optical Amplifiers for Multi–Band Optical Transmission Systems. *Journal of Lightwave Technology*, 40(6):1579–1589, mar 2022.

[125] Amp-fl8221-sb-16 amplifier datasheet from fiberlabs inc.

[126] S. Aozasa, H. Masuda, H. Ono, T. Sakamoto, T. Kanamori, Y. Ohishi, and M. Shimizu. 1480-1510 nm-band Tm doped fiber amplifier (TDFA) with a high power conversion efficiency of 42%. In *Optical Fiber Communication Conference (2001)*, page PD1. Optica Publishing Group, mar 2001.

[127] V V Dvoirin, V M Mashinskii, O I Medvedkov, A A Umnikov, Aleksei N Gur'yanov, and Evgenii M Dianov. Bismuth-doped telecommunication fibres for lasers and amplifiers in the 1400–1500-nm region. *Quantum Electronics*, 39(6):583–584, jun 2009.

[128] Aleksandr Donodin, Vladislav Dvoyrin, Egor Manuylovich, Lukasz Krzczanowicz, Wladek Forysiak, Mikhail Melkumov, Valery Mashinsky, and Sergei Turitsyn. Bismuth doped fibre amplifier operating in E- and S-optical bands. *Optical Materials Express*, 11(1):127, jan 2021.

[129] P. Poggiolini, G. Bosco, A. Carena, R. Cigliutti, V. Curri, F. Forghieri, R. Pastorelli, and S. Piciaccia. The LOGON Strategy for Low-Complexity Control Plane Implementation in New-Generation Flexible Networks. *Optical Fiber Communication Conference - OFC 2013*, (1):1–3, 2013.

[130] Alessio Ferrari, Dario Pilori, Emanuele Virgillito, and Vittorio Curri. Power Control Strategies in C+L Optical Line Systems. *2019 Optical Fiber Communications Conference and Exhibition, OFC 2019 - Proceedings*, pages 10–12, 2019.

[131] Fukutaro Hamaoka, Masanori Nakamura, Seiji Okamoto, Kyo Minoguchi, Takeo Sasai, Asuka Matsushita, Etsushi Yamazaki, and Yoshiaki Kisaka. Ultra-Wideband WDM Transmission in S -, C -, and L -Bands Using Signal Power Optimization Scheme. *Journal of Lightwave Technology*, 37(8):1764–1771, apr 2019.

[132] Ian Roberts, Joseph M. Kahn, James Harley, and David W. Boertjes. Channel Power Optimization of WDM Systems Following Gaussian Noise Nonlinearity Model in Presence of Stimulated Raman Scattering. *Journal of Lightwave Technology*, 35(23):5237–5249, dec 2017.

[133] Alessio Ferrari, Antonio Napoli, Johannes Karl Fischer, Nelson Costa, Andrea D'Amico, Joao Pedro, Wladek Forysiak, Erwan Pincemin, Andrew Lord, Alexandros Stavdas, Juan Pedro F.-P. Gimenez, Gunther Roelkens, Nicola Calabretta, Silvio Abrate, Bernd Sommerkorn-Krombholz, and Vittorio Curri. Assessment on the Achievable Throughput of Multi-Band ITU-T G.652.D Fiber Transmission Systems. *Journal of Lightwave Technology*, 38(16):4279–4291, aug 2020.

[134] R. Pastorelli, S. Piciaccia, G. Galimberti, E. Self, M. Brunella, G. Calabretta, F. Forghieri, D. Siracusa, A. Zanardi, E. Salvadori, G. Bosco, A. Carena, V. Curri, and P. Poggiolini. Optical control plane based on an analytical model of non-linear transmission effects in a self-optimized network. In *39th European Conference and Exhibition on Optical Communication (ECOC 2013)*, volume 2013, pages 555–557, London, 2013.

[135] Vittorio Curri, Andrea Carena, Andrea Arduino, Gabriella Bosco, Pierluigi Poggiolini, Antonino Nespola, and Fabrizio Forghieri. Design Strategies and Merit of System Parameters for Uniform Uncompensated Links Supporting Nyquist-WDM Transmission. *Journal of Lightwave Technology*, 33(18):3921–3932, sep 2015.

[136] Alessio Ferrari, Dario Pilori, Emanuele Virgillito, and Vittorio Curri. Power Control Strategies in C+L Optical Line Systems. *2019 Optical Fiber Communications Conference and Exhibition, OFC 2019 - Proceedings*, pages 10–12, 2019.

[137] Emanuele Virgillito, Rasoul Sadeghi, Alessio Ferrari, Giacomo Borraccini, and Vittorio Curri. Network Performance Assessment of C+L Upgrades vs. Fiber Doubling SDM Solutions. In *Optical Fiber Communication Conference (OFC) 2020*, page M2G.4, Washington, D.C., 2020. OSA.

[138] Vittorio Curri. Software-defined WDM optical transport in disaggregated open optical networks. *International Conference on Transparent Optical Networks*, 2020-July:1–4, 2020.

[139] Michel Gendreau and Jean-Yves Potvin. *Handbook of Metaheuristics*, volume 272 of *International Series in Operations Research & Management Science*. Springer International Publishing, Cham, 2019.

[140] Abdullah Konak, David W. Coit, and Alice E. Smith. Multi-objective optimization using genetic algorithms: A tutorial. *Reliability Engineering & System Safety*, 91(9):992–1007, sep 2006.

[141] Kalyanmoy Deb, Amrit Pratap, Sameer Agarwal, and T. Meyarivan. A fast and elitist multiobjective genetic algorithm: NSGA-II. *IEEE Transactions on Evolutionary Computation*, 6(2):182–197, apr 2002.

[142] S VFirstov, V F Khopin, I A Bufetov, E G Firstova, A N Guryanov, E M Dianov, V V Dvoyrin, V M Mashinsky, A A Umnikov, M V Yashkov, A Bufetov, M A Melkumov, S V Firstov, A V Shubin, O I Medvedkov, M Yu Sharonov, A B Bykov, V Petricevic, and R R Alfano. Combined excitation-emission spectroscopy of bismuth active centers in optical fibers. *Optics Express*, 19(20):19551–19561, sep 2011.

[143] Y. Wang, N. K. Thipparapu, D. J. Richardson, and J. K. Sahu. Broadband Bismuth-Doped Fiber Amplifier With a Record 115-nm Bandwidth in the O and E Bands. In *Optical Fiber Communication Conference Postdeadline*

Papers 2020 (2020), volume F174, page Th4B.1. Optica Publishing Group, mar 2020.

[144] Aleksandr Donodin, Vladislav Dvoyrin, Egor Manuylovich, Lukasz Krzczanowicz, Wladek Forysiak, Mikhail Melkumov, Valery Mashinsky, and Sergei Turitsyn. Bismuth doped fibre amplifier operating in E- and S-optical bands. *Optical Materials Express*, 11(1):127, jan 2021.

[145] M. A. Melkumov, V. Mikhailov, A. M. Hegai, K. E. Riumkin, P. S. Westbrook, D. J. DiGiovanni, and E. M. Dianov. E-band data transmission over 80 km of non-zero dispersion fibre link using bismuth-doped fibre amplifier. *Electronics Letters*, 53(25):1661–1663, dec 2017.

[146] V. Mikhailov, M. A. Melkumov, D. Inniss, A. M. Khegai, K. E. Riumkin, S. V. Firstov, F. V. Afanasiev, M. F. Yan, Y. Sun, J. Luo, G. S. Puc, S. D. Shenk, R. S. Windeler, P. S. Westbrook, R. L. Lingle, E. M. Dianov, and D. J. Digiovanni. Simple Broadband Bismuth Doped Fiber Amplifier (BDFA) to Extend O-band Transmission Reach and Capacity. In *Optical Fiber Communication Conference (OFC)*, page M1J.4. Optica Publishing Group, mar 2019.

[147] Open ZR+ MSA Technical Specification. https://openzrplus.org/site/assets/files/1075/openzrplus_1p0.pdf.

[148] Nicola Sambo, Alessio Ferrari, Antonio Napoli, Nelson Costa, Joao Pedro, Bernd Sommerkorn-Krombholz, Piero Castoldi, and Vittorio Curri. Provisioning in Multi-Band Optical Networks. *Journal of Lightwave Technology*, 38(9):2598–2605, may 2020.

[149] Masahiro Nakagawa, Hiroki Kawahara, Kana Masumoto, Toshiya Matsuda, and Kazuyuki Matsumura. Performance Evaluation of Multi-Band Optical Networks Employing Distance-Adaptive Resource Allocation. *25th Opto-Electronics and Communications Conference, OECC 2020*, pages 2020–2022, 2020.

[150] Mahdieh Mehrabi, Hamzeh Beyranvand, and Mohammad Javad Emadi. Multi-Band Elastic Optical Networks: Inter-Channel Stimulated Raman Scattering-Aware Routing, Modulation Level and Spectrum Assignment. *Journal of Lightwave Technology*, 39(11):3360–3370, jun 2021.

[151] N Sambo, Alessio Ferrari, A Napoli, J Pedro, L S Kiani, P Castoldi, and V Curri. Multiband Seamless Network Upgrade by Exploiting the E-band. In *2021 European Conference on Optical Communication (ECOC)*, volume Tu2E.1, pages 1–4. IEEE, sep 2021.

[152] Jay W Dawson, Leily S Kiani, Paul H Pax, Graham S Allen, Derrek R Drachenberg, Victor V Khitrov, Diana Chen, Nick Schenkel, Matthew J Cook, Robert P Crist, and Michael J Messerly. E-band Nd3+ amplifier based on wavelength selection in an all-solid micro-structured fiber. *Optics Express*, 25(6):6524, mar 2017.

[153] Polyzois Soumplis, Konstantinos Christodoulopoulos, Marco Quagliotti, Annachiara Pagano, and Emmanouel Varvarigos. Network Planning With Actual Margins. *Journal of Lightwave Technology*, 35(23):5105–5120, dec 2017.

[154] Nicola Sambo, Filippo Cugini, Giulio Bottari, Paola Iovanna, and Piero Castoldi. Distributed Setup in Optical Networks with Flexible Grid. In *37th European Conference and Exposition on Optical Communications*, page We.10.P1.100, Washington, D.C., sep 2011. OSA.

[155] Daniela Moniz, Victor Lopez, and João Pedro. Design Strategies Exploiting C+L-band in Networks with Geographically-dependent Fiber Upgrade Expenditures. In *Optical Fiber Communication Conference (OFC) 2020*, volume Part F174-, page M2G.3, Washington, D.C., 2020. Optica Publishing Group.

[156] Rana Kumar Jana, Abhijit Mitra, Aniket Pradhan, Kristofer Grattan, Anand Srivastava, Biswanath Mukherjee, and Andrew Lord. When Is Operation Over C + L Bands More Economical than Multifiber for Capacity Upgrade of an Optical Backbone Network? In *2020 European Conference on Optical Communications (ECOC)*, pages 1–4. IEEE, dec 2020.

[157] J. López Vizcaíno, Y. Ye, F. Jiménez, A. Macho, and P. M. Krummrich. Optimized Amplifier Placements for Improved Energy and Spectral Efficiency in Protected Mixed-Line-Rate Networks. In *Optical Fiber Communication Conference*, page Th1E.5, Washington, D.C., 2014. OSA.

[158] Joao Pedro and Nelson Costa. Optimized Hybrid Raman/EDFA Amplifier Placement for DWDM Mesh Networks. *Journal of Lightwave Technology*, 36(9):1552–1561, may 2018.

[159] Yu Gu, Yongcheng Li, Ningning Guo, Xiaodi You, and Gangxiang Shen. L-band Amplifier Placement in C+L-band Elastic Optical Networks. In *Asia Communications and Photonics Conference 2021*, page M5I.2, Washington, D.C., 2021. Optica Publishing Group.

[160] Thierry Zami, Ivan Fernandez de Jauregui Ruiz, Amirhossein Ghazisaeidi, and Bruno Lavigne. Growing impact of optical filtering in future WDM networks. In *Optical Fiber Communication Conference (OFC) 2019*, volume Part F160-, page M1A.6, Washington, D.C., 2019. OSA.

Appendix A

Optical network topologies

All the optical network topologies use in this work are presented in Figure A.1, with the main parameters described bellow.

- Figure A.1a – German topology (Dutch telecom – DT) composed by 17 optical nodes, 26 links, average node degree of 3.0, and average link length of 236.6 km.
- Figure A.1b – US-NET topology composed by 24 optical nodes, 43 links, average node degree of 3.6, and average link length of 833.7 km.
- Figure A.1c – European (COST) topology, composed by 28 optical nodes, 41 links, average node degree of 2.9, and average link length of 658.6 km.
- Figure A.1d – Italian topology composed by 21 optical nodes, 36 links, average node degree of 3.4, and average link length of 270.8 km.
- Figure A.1e – Japanese topology composed by 25 optical nodes, 43 links, average node degree of 3.4, and average link length of 291.3 km.
- Figure A.1f – Spanish topology composed by 30 optical nodes.

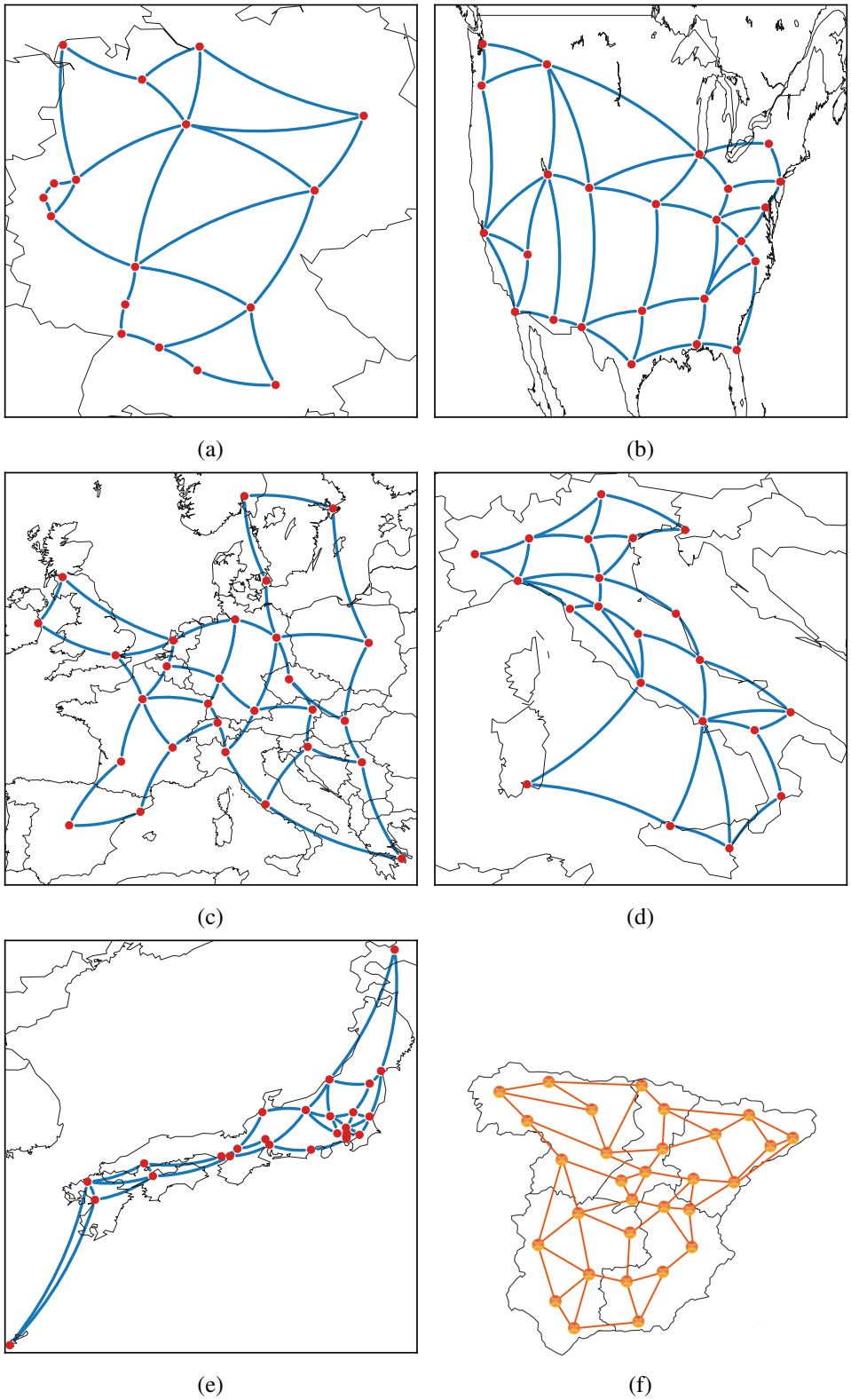

Fig. A.1 Optical network topologies used in this work. (a) DT, (b) US-NET, (c) COST, (d) Italian, (e) Japanese, and (f) Spanish.

Appendix B

Fiber and devices characteristics

B.1 Transceivers characteristics

Table B.1 presents the flexible rate transceiver characteristics, i.e. modulation formats, an their respective data rates, power, and required GSNR. These values are reported in [147].

Table B.1 Transceivers modelling assumptions.

Modulation	**Data rate [Gbps]**	**P [W]**	**RGSNR [dB/0.1nm]**
DP-16QAM	400	20	24
DP-8QAM	300	18	21
DP-QPSK	200	16	16
DP-QPSK	100	13	12.5